FERMILAB-THESIS-2014-31

Sterile Neutrino Searches in MiniBooNE and MicroBooNE

by

Christina M. Ignarra

Submitted to the Department of Physics
in partial fulfillment of the requirements for the degree of

Doctor of Philosophy in Physics

at the

MASSACHUSETTS INSTITUTE OF TECHNOLOGY

September 2014

© Massachusetts Institute of Technology 2014. All rights reserved.

Signature of Author .....
Department of Physics
August 29, 2014

Certified by .....
Janet M. Conrad
Professor of Physics
Thesis Supervisor

Accepted by .....
Krishna Rajagopal
Associate Department Head for Education

Operated by Fermi Research Alliance, LLC under Contract No. DE-AC02-07CH11359 with the United States Department of Energy

Sterile Neutrino Searches in MiniBooNE and MicroBooNE

by
Christina M. Ignarra

Submitted to the Department of Physics
on August 29, 2014, in partial fulfillment of the
requirements for the degree of
Doctor of Philosophy in Physics

Abstract

Tension among recent short baseline neutrino experiments has pointed toward the possible need for the addition of one or more sterile (non-interacting) neutrino states into the existing neutrino oscillation framework. This thesis first presents the motivation for sterile neutrino models by describing the short-baseline anomalies that can be addressed with them. This is followed by a discussion of the phenomenology of these models. The MiniBooNE experiment and results are then described in detail, particularly the most recent antineutrino analysis. This will be followed by a discussion of global fits to world data, including the anomalous data sets. Lastly, future experiments will be addressed, especially focusing on the MicroBooNE experiment and light collection studies. In particular, understanding the degradation source of TPB, designing the TPB-coated plates for MicroBooNE and developing lightguide collection systems will be discussed.

We find an excess of events in the MiniBooNE antineutrino mode results consistent with the LSND anomaly, but one that has a different energy dependence than the low-energy excess reported in neutrino mode. This disagreement creates tension within global fits which include up to three sterile neutrinos. The low-energy excess will be addressed by the MicroBooNE experiment, which is expected to start taking data in early 2015. Tension among existing experiments calls for additional, more decisive future experiments.

Thesis Supervisor: Janet M. Conrad
Title: Professor of Physics

Acknowledgments

First and foremost, I would like to thank my advisor, Janet Conrad. Your enthusiasm is truly contagious and you have helped me grow more than I thought possible. Thank you for your undying support and guidance, and for always pushing me forward when I had my sights firmly set sideways.

To the rest of the group, past and present: Teppei Katori and Matt Toups, it was wonderful to work with you on MicroBooNE; I really appreciate that you were always available to answer questions and provide a helping hand. Lindley Winslow and Josh Spitz, even though we had no overlap in our work, you always took the time to provide help and support, and I will forever think of you as "my postdocs" anyway. And of course, all of the graduate students in the group with whom I have overlapped: Ben Jones, Marjon Moulai, Gabriel Collin, Georgia Karagiorgi, Chris Jones, and Kazu Terao. Thank you for insightful conversations, help, and friendship. Zander Moss and Christie Chiu, you have done outstanding work and set the bar extremely high for any students I will "supervise" in the future. Len Bugel, it was loads of fun working with you in the lab; thank you for sharing your wisdom and expertise. Jose Alonso, Daniel Winklehner, and Taritree Wongjirad, there is an extraordinary sense of camaraderie in this group despite our various geographical locations. It has been a pleasure working with all of you!

Mike Shaevitz, thank you for all of your support and collaboration. You have helped to guide me all the way from my undergraduate REU through the end of my PhD, and hopefully, beyond.

Thank you to all of the MiniBooNE and MicroBooNE collaborators who have given me help and guidance. I am especially grateful to Zarko Pavlovic, for getting me set up with MiniBooNE and helping me along the way. And thank you to Stephen Pordes, Paul Nienaber, Bill Lewis, Byron Roe, and Ana Pla for advice and collaboration. Thank you also to my out-of-collaboration-collaborators, Joe Formaggio, Peter Fisher, Tali Figueroa, and Kim Palladino.

I appreciate all of the graduate students at MIT who have taken the edge off of graduate school through friendship, collaboration, and wings night at the Muddy. Also all of the students at Fermilab who helped to make Fermilab feel like a home away from home.

Thank you Simon, for supporting every possible aspect of my life and career and for always being there for me. I am a lot more productive, successful, and happy for having you in my life! And thank you to my parents, Ed and Dawn, for your unconditional love, understanding, and support. I could not have done this without all of you!

Contents

1 Introduction **14**
1.1 Neutrinos and the Standard Model of Particle Physics 14
1.2 Neutrino Oscillations 18
1.2.1 Formalism for Two Neutrinos 18
1.2.2 Formalism for Three Neutrinos 19
1.2.3 Experimental Tests of Three Neutrino Oscillations 20
1.3 Open Questions in Neutrino Physics 22
1.4 This Thesis on Sterile Neutrinos and the MiniBooNE Anomaly 23

2 Sterile Neutrinos **25**
2.1 Experimental Motivation 25
2.1.1 The LSND Experiment 25
2.1.2 MiniBooNE 29
2.1.3 The Reactor Antineutrino Anomaly 29
2.1.4 The Gallium Experiments 30
2.1.5 Null Experiments 33
2.2 Phenomenology 33
2.2.1 $3+1$ Model 33
2.2.2 Extending to $3+2$ and $3+3$ Models 38
2.3 Sterile Neutrinos in Cosmology 39

3 Detecting Neutrinos with MiniBooNE **41**
3.1 The Booster Neutrino Beam 41
3.2 The MiniBooNE Detector 42
3.3 Cherenkov Rings in MiniBooNE 44
3.4 Types of Neutrino Interactions in MiniBooNE 45
3.4.1 Quasi-Elastic Scattering 47
3.4.2 Resonance Production 47
3.4.3 Deep Inelastic Scattering 49
3.5 Final State Interactions 49
3.6 Event Reconstruction 50
3.6.1 Identifying Events 50
3.6.2 Particle Track and Energy Reconstruction 50
3.6.3 Particle ID 51
3.6.4 Reconstructed *vs.* True Neutrino Energies 51

3.7 Backgrounds to The Appearance Signal . . . 53
3.7.1 NC π^0 Background . . . 53
3.7.2 Radiative Δ Decay . . . 54
3.7.3 Intrinsic ν_e Background . . . 57
3.7.4 Wrong-sign ν_e Background . . . 57
3.7.5 Dirt Backgrounds . . . 60

4 The MiniBooNE Electron-Flavor Appearance Analyses 63
4.1 Systematic Uncertainties in the Oscillation Analysis . . . 63
4.1.1 Covariance Matrix Construction . . . 63
4.1.2 Sources and Determination of Errors . . . 64
4.1.3 ν_μ CCQE constraint . . . 69
4.1.4 Statistical Uncertainties . . . 69
4.1.5 Differences between neutrino and antineutrino mode systematics 69
4.2 The Oscillation Analysis . . . 70
4.2.1 Constructing a χ^2 . . . 71
4.2.2 Drawing Confidence Level Contours . . . 72
4.3 Results . . . 72
4.3.1 First Results: $\nu_\mu \to \nu_e$ Appearance . . . 72
4.3.2 Discussion of Low-Energy Excess . . . 77
4.3.3 Antineutrino Mode: $\bar{\nu}_\mu \to \bar{\nu}_e$ Appearance . . . 77
4.3.4 Combined Fit . . . 78
4.4 Fitting MiniBooNE Data to a $3+2$ Model . . . 79
4.5 Accounting for Disappearance Within the Appearance Analysis . . . 83
4.6 Multinucleon Effects . . . 84

5 Global Fits 85
5.1 Experiments Included in the Fits . . . 85
5.1.1 Muon-to-Electron-Flavor Appearance . . . 90
5.1.2 Muon Flavor Disappearance . . . 91
5.1.3 Electron Flavor Disappearance . . . 93
5.2 Fitting Procedure . . . 94
5.3 Results . . . 96
5.4 Recent Constraints Since Published Work . . . 99
5.4.1 MiniBooNE/SciBooNE . . . 102
5.4.2 ICARUS . . . 102
5.4.3 OPERA . . . 102

6 MicroBooNE 104
6.1 Overview . . . 104
6.2 The MicroBooNE Detector . . . 105
6.2.1 Event Signatures and e-γ Separation . . . 106
6.3 MicroBooNE Light Collection System . . . 108
6.3.1 Scintillation Light in Liquid Argon . . . 110

6.3.2 PMT System Design 111
6.4 TPB Wavelength-Shifting Coating 112
6.4.1 Types of TPB Coatings in MicroBooNE and Other Experiments 112
6.4.2 Comparing TPB Coatings 115
6.4.3 TPB Degradation 121
6.4.4 MicroBooNE Plate Production and Deployment 122
6.5 MicroBooNE Physics Goals 123

7 Other Current and Future LArTPCs 125
7.1 Previous and Current Experiments 125
7.2 Future Experiments 126
7.3 A Lightguide System for Light Detection in Future LArTPCs 127
7.3.1 Description of System 127
7.3.2 MIT Lightguide Test Stand 128

8 Future Sterile Neutrino Searches 134
8.1 LAr at Fermilab 134
8.2 IsoDAR 135
8.3 SOX 136
8.4 νSTORM 139
8.5 OscSNS 140
8.6 Ricochet 141

9 Conclusion 142

List of Figures

1-1 The predicted cross section for two, three, and four neutrino species as a function of center of mass energy at the Z resonance on top of data points. 16
1-2 The solar neutrino spectrum. 17
1-3 KamLAND data compared with prediction based on best fit oscillation parameters. 21
1-4 Flavor breakdown of the three mass eigenstates. 22

2-1 The neutrino flux from a decay at rest beam. 26
2-2 A schematic of the LSND detector with a $\bar{\nu}_e$ candidate event. 27
2-3 The excess beam events in the LSND experiment as a function of L/E. 28
2-4 The region in Δm^2 vs. $\sin^2 2\theta$ parameter space allowed by LSND at 90% CL. 29
2-5 The ratio of the observed number of neutrinos divided by the expected number for a variety of short-baseline reactor experiments. 31
2-6 The allowed regions in Δm^2 vs $\sin^2(2\theta)$ parameter space from a fit to short-baseline reactor experiments. 32
2-7 Data points showing the results from the gallium source experiments. 33
2-8 The confidence level contours and best fit value in Δm^2 vs $\sin^2(2\theta)$ parameter space from a fit to data from the GALLEX and SAGE radioactive source experiments. 34
2-9 The flavor breakdown of the mass states in a $3+1$ model. 36
2-10 A representation of neutrino states as physical objects. 37

3-1 The neutrino and antineutrino flux predictions for all neutrino species at MiniBooNE. 43
3-2 A schematic of the MiniBooNE detector hall and detector. 44
3-3 An example of muon and electron Cherenkov rings in the MiniBooNE detector. 45
3-4 Measured and predicted CC cross-sections per nucleon as a function of neutrino energy for neutrinos and antineutrinos. 46
3-5 Feynman diagrams for CCQE interactions. 48
3-6 The distributions of $R_{e/\mu}$ for ν_e (left) and ν_μ (right) events as a function of electron-hypothesis reconstructed energy. 52
3-7 The distributions of $R_{e/\pi}$ for ν_e (left) and ν_π (right) events as a function of electron-hypothesis reconstructed energy. 52

3-8 The relationship between the true neutrino energy E_{true} and the reconstructed neutrino energy, E_ν^{QE} in neutrino mode. 53
3-9 Neutrino and antineutrino mode backgrounds in an energy range of reconstructed energy between 200 MeV $< E_\nu^{QE} <$ 3000 MeV. 55
3-10 The predicted number of events from π^0 misIDs for the neutrino-mode data set. 56
3-11 Angular distribution of pions relative to the proton beam. 58
3-12 The $CC1\pi^+$ sample reconstructed energy spectrum comparing data to MC. 59
3-13 The constraint of the neutrino component to the antineutrino mode beam. 60
3-14 The R_{btw} distribution before and after the fit was done. 61
3-15 The UR/R distribution before and after the fit was done. 62

4-1 The predicted ν_μ and $\bar{\nu}_\mu$ flux in neutrino mode divided by parent meson. 66
4-2 The predicted ν_μ and $\bar{\nu}_\mu$ flux in antineutrino mode divided by parent meson 67
4-3 Neutrino mode data over predicted backgrounds for CCQE events as a function of reconstructed neutrino energy, E_ν^{QE}. 73
4-4 Neutrino mode data minus background. 74
4-5 CL contours from a fit to MiniBooNE neutrino-mode data in an energy range between 475 MeV $< E_\nu^{QE} <$ 1250 MeV. 75
4-6 CL contours from a fit to MiniBooNE neutrino-mode data in an energy range between 200 MeV $< E_\nu^{QE} <$ 1250 MeV. 76
4-7 Antineutrino mode data over predicted backgrounds for CCQE events as a function of reconstructed neutrino energy, E_ν^{QE}. 78
4-8 Antineutrino mode data minus background. 79
4-9 CL contours from a fit to MiniBooNE antineutrino-mode data in an energy range between 200 MeV $< E_\nu^{QE} <$1250 MeV. 80
4-10 The data minus background histograms from Figures 4-4 and 4-8 here plotted with predictions representing the best fit values from a combined $3+1$ (two-neutrino) fit and a combined $3+2$ fit. 81
4-11 CL contours from a combined fit to MiniBooNE neutrino-mode data and antineutrino-mode data in an energy range between 200 MeV $< E_\nu^{QE} <$1250 MeV. 82

5-1 Summary of $\bar{\nu}_\mu \to \bar{\nu}_e$ and $\nu_\mu \to \nu_e$ results, shown at 90% and 99% CL. 87
5-2 Summary of $\bar{\nu}_\mu \to \bar{\nu}_\mu$ and $\nu_\mu \to \nu_\mu$ results, shown at 90% and 99% CL. 88
5-3 Summary of $\bar{\nu}_e \to \bar{\nu}_e$ and $\nu_e \to \nu_e$ results, shown at 90% and 99% CL. 89
5-4 Confidence level contours projected onto two-dimensional parameter space (Δm^2_{41} *vs.* $\sin^2(2\theta_{\mu e})$) from a $3+1$ global fit. 98
5-5 Confidence level contours projected onto two-dimensional parameter space (Δm^2_{51} *vs.* Δm^2_{41}) from a $3+2$ global fit. 98

5-6 Confidence level contours projected onto two-dimensional parameter space (Δm^2_{51} *vs.* Δm^2_{41}) resulting from a $3+2$ fit to appearance experiments, and disappearance experiments. 99
5-7 The MiniBooNE neutrino and antineutrino excess data with signal predictions for each of the global best-fit and appearance-only best-fit oscillation signal predictions for $3+1$, $3+2$, and $3+3$ models. 100
5-8 The $3+1$, $3+2$, and $3+3$ oscillation probabilities for the global best-fit values. 101
5-9 The limits from a MiniBooNE/SciBooNE dual-baseline search for muon neutrino and antineutrino disappearance. 102
5-10 The limits from the ICARUS experiment for an electron-flavor appearance search. 103

6-1 A schematic of the outside of the MicroBooNE cryostat and internal TPC. 105
6-2 Photographs of the MicroBooNE TPC and cryostat. 106
6-3 Muon, electron, and π^0 events in the MicroBooNE detector. 107
6-4 Energy loss for 0.5 - 5 MeV electrons and photons in MicroBooNE. . 108
6-5 Simulated signals in MicroBooNE of a photon signal over photon backgrounds and an electron signal over electron backgrounds. 109
6-6 A photograph of the PMT units including TPB coated plates mounted on the PMT rack in the MicroBooNE cryostat. 111
6-7 A schematic and photograph of an individual PMT unit. 113
6-8 The TPB emission spectrum from an evaporative coating for a variety of different incident wavelengths. 114
6-9 A photograph of one of the MicroBooNE TPB coated plates immediately after it was coated. 115
6-10 Setup for vacuum monochromator measurements. 116
6-11 The spectrum from a McPherson model 632 vacuum UV deuterium source. 117
6-12 The plate holder and PMT mount for the LAr tests described in the text. 118
6-13 An example waveform acquired by the Alazar Tech ATS9870 digitizer. 119
6-14 TPB coating efficiencies measured in a vacuum monochrometer and in LAr. 120
6-15 The test setup for the TPB degradation studies. 121
6-16 The results of the TPB degradation study. 122
6-17 The sensitivity expected by the MicroBooNE experiment from a run of 6.6×10^{20} protons on target in neutrino mode for a search for ν_e appearance. 123
6-18 The sensitivity expected by the MicroBooNE experiment for a ν_μ disappearance analysis. 124

7-1 A photograph of a collection of lightguide bars adiabatically bent to form a paddle. 127

7-2 A photograph of a lightguide and PMT holder. 129
7-3 Examples of events read-out with a waveform digitizer. 130
7-4 Example integrated charge distributions at different distances along a cast acrylic bar. 131
7-5 Attenuation length measurement of cast acrylic bars with UVT25% coatings. 132
7-6 The placement of four lightguide paddles in the MicroBooNE PMT rack. 133

8-1 The sensitivity expected by the proposed LAr1-ND detector combined with MicroBooNE. 135
8-2 The sensitivity expected by the proposed ICARUS @ FNAL in neutrino mode for 3 years of running. 136
8-3 Predicted errors on data points along an oscillation wave for 5 years of IsoDAR running at the KAMLAND detector. 137
8-4 The sensitivity expected by IsoDAR at Juno or IsoDAR at KAMLAND. 138
8-5 The sensitivity expected by IsoDAR with 5 years of running at KamLAND for a variety of potential signal parameters. 138
8-6 The sensitivity expected by the SOX experiment for each of its three phases. 139
8-7 The sensitivity expected by the νSTORM experiment. 140
8-8 The sensitivity expected by OscSNS for three years of running. 141

List of Tables

2.1 A list of which experiments have a signal at 90% Confidence Level and which do not. 35

4.1 Systematic errors (%) for the ν_e signal (oscillated from MC events for each mass and mixing model), ν_e background, and ν_μ CCQE samples before the ν_μ constraint is applied. 64

4.2 Systematic errors (%) for the $\bar{\nu}_e$ signal (oscillated from MC events for each mass and mixing model), $\bar{\nu}_e$ background and $\bar{\nu}_\mu$ CCQE samples before the $\bar{\nu}_\mu$ constraint is applied. 65

4.3 The expected background events in the range of $200 < E_\nu^{QE} < 1250$ MeV for both the neutrino and antineutrino analyses 70

5.1 Details about the process, energy range, and baseline for each data set used in the global fits. 86

5.2 The χ^2 values and corresponding probabilities for the best-fit points to the models considered. 97

5.3 The compatibility between appearance *vs.* disappearance experiments and neutrino *vs.* antineutrino experiments for each model. 97

Chapter 1

Introduction

1.1 Neutrinos and the Standard Model of Particle Physics

Wolfgang Pauli proposed the existence of the neutrino as a "desperate remedy" in order to save a fundamental law of physics. Conservation of energy appeared to be violated in studies of beta decay, a process where a neutron decays into a proton and an electron (and an antineutrino):

$$n \rightarrow p + e^- + \bar{\nu}_e \tag{1.1}$$

Being nearly massless, weakly interacting, and electrically neutral, the outgoing antineutrino was undetectable at the time. This the kinematics of the remaining particles thus appeared to violate energy conservation. In order for such a particle to have escaped detection up to that point, it would have to have an extremely small interaction cross-section, leading the community to doubt that the neutrino would ever be detected.

That changed when the antineutrino was discovered by Reines and Cowan in 1956 [1]. They detected antineutrinos at a nuclear reactor through inverse beta decay:

$$\bar{\nu}_e + p \rightarrow n + e^+. \tag{1.2}$$

When the muon was discovered in 1937 and subsequently found to decay into only one electron, neutrinos were suspected to be involved in this interaction as well. In fact, kinematics distributions indicated that there were two neutrinos involved in muon decay. It was later observed that there were two distinct flavors of neutrino when the first accelerator-based neutrino experiments (using a source of muon neutrinos from pion decay) detected only outgoing muons from neutrino interactions. This was contrary to reactor experiments, which had only seen electrons.

As soon as the tau was discovered in the 1970s, it was suspected that it, too, had a corresponding neutrino. By this time electroweak theory was established. The role of the neutrino in the standard model of particle physics was thought to be understood within what appeared to be a neat and complete picture.

In this picture, there were three flavors of neutrinos, corresponding to each of the three charged leptons: the electron, the muon, and the tau. One of the most common types of neutrino interaction is charged current quasi-elastic scattering (CCQE), where a neutrino (antineutrino) will interact with a neutron (proton) to produce the corresponding charged lepton (anti-lepton) and a proton (neutron):

$$\begin{aligned} \nu_l + n &\rightarrow l^- + p \\ \bar{\nu}_l + p &\rightarrow l^+ + n \end{aligned} \tag{1.3}$$

Neutrinos interact through the weak force, which is mediated by the $W^{\pm}$ and Z^0 bosons. An interaction where the $W^{\pm}$ is exchanged (as in Equation 1.3) is called a charged current (CC) interaction. Alternatively, an interaction where the Z^0 boson is exchanged is called a neutral current (NC) interaction:

$$\begin{aligned} \nu_l + N &\rightarrow \nu_l + N \\ \bar{\nu}_l + N &\rightarrow \bar{\nu}_l + N \end{aligned} \tag{1.4}$$

where N represents a nucleon–either a proton or a neutron.

From studying the decay of the Z boson, we know that there cannot be more than three flavors of light neutrinos that interact through the weak force. The width of the Z^0 resonance is dependent on N_ν, the number of weakly interacting light neutrino states (Figure 1-1). This measurement corresponds to $N_\nu = 2.9840 \pm 0.0082$ [2], a stringent result.

Neutrinos were originally assumed to be massless because this provided a convenient explanation for "parity violation." While studying the beta decay spectrum of ^{60}Co atoms polarized by a magnetic field, C.S. Wu discovered a clear anti-correlation between the spin of the nucleus and the emitted electron direction, while parity conservation would have indicated emission at equal rates in either direction [4]. This was the first proof that parity was maximally violated in the weak interaction, meaning that the neutrino spin must be correlated with its momentum vector. Subsequent measurements have shown that all neutrinos have these vectors anti-aligned (so they have "left-handed" chirality) and all antineutrinos have their spin aligned to their momentum (and so have "right-handed" chirality). This led to the belief that neutrinos must be massless. If they had mass, one would be able to boost into a frame with a higher velocity than that of the the neutrino, thus observing a neutrino with right-handed helicity. This problem would be irrelevant if neutrinos were massless since the neutrino would move at the speed of light and there would be no such frame (helicity and chirality would be equivalent in that case).

This straightforward picture of neutrinos did not last long; it was shattered by the "solar neutrino problem." By the late 1960s, the solar model was well established and the neutrino flux from various solar processes was predicted (Figure 1-2). The Homestake experiment sought to measure these solar neutrinos, and did so successfully, but only saw about a third of the expected number of neutrinos. Many years passed where most of the community thought that either the experiment or the predictions were incorrect, but complimentary experiments began to reproduce the same results.

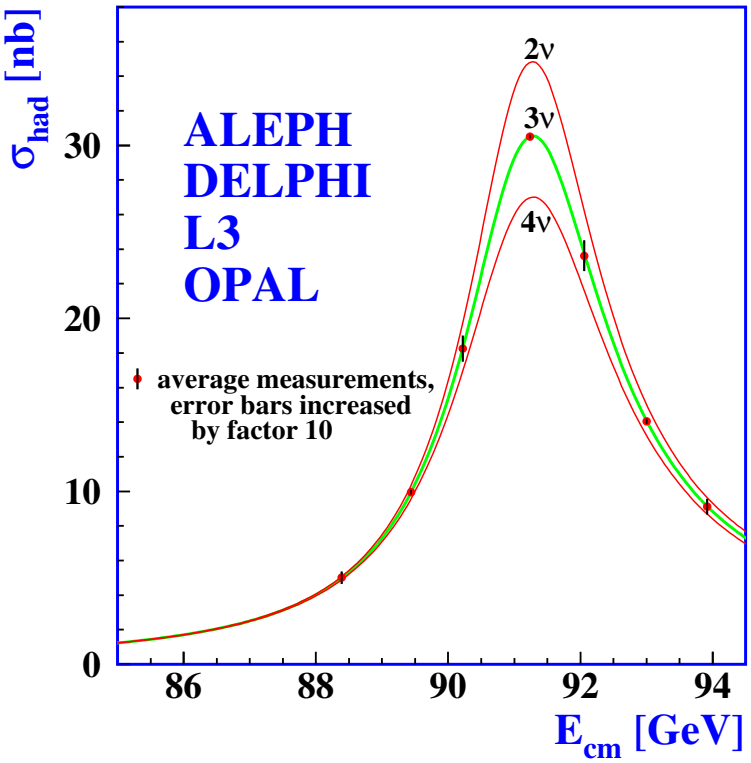

Figure 1-1: The predicted cross section for two, three, and four neutrino species as a function of center of mass energy at the Z resonance on top of data points. This plot indicates that there are three light neutrino species that interact weakly with standard model couplings. From Reference [3].

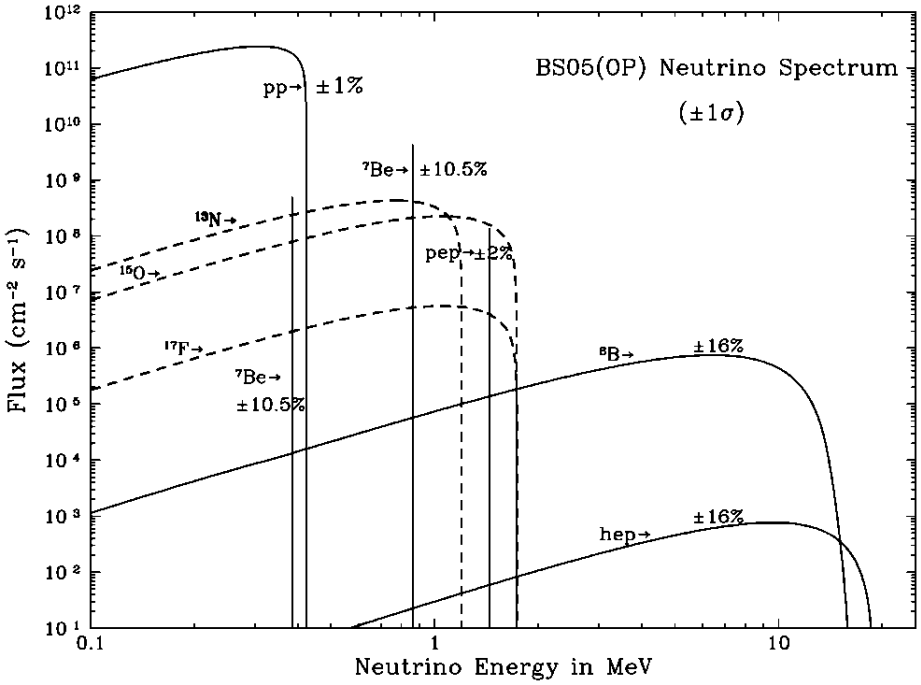

Figure 1-2: The solar neutrino spectrum from Reference [5]. The Homestake detector was sensitive to neutrinos above 0.845 MeV, the threshold energy of the inverse beta decay process on ^{37}Cl, the detector medium.

The processes in the sun produce only electron flavored neutrinos. Experiments such as Gallex [6] and Sage [7], were also only sensitive to this flavor since they measure CCQE interactions. The energy of a solar neutrino is insufficient to produce a muon or a tau in the detector. This lent credence to the theory of neutrino oscillations, where one flavor of neutrino is able to change into another. The result could be explained if the electron neutrinos were oscillating into muon and tau flavors.

1.2 Neutrino Oscillations

Neutrino oscillations are a quantum mechanical effect that can only occur if neutrinos have mass. In this section, the formalism is introduced within a two neutrino model for simplicity. The model is then expanded to three neutrinos. Lastly, we consider the present status of experimental tests of the three neutrino model.

1.2.1 Formalism for Two Neutrinos

Neutrino mixing is a rotation between the mass eigenstates and the flavor states. This mixing can be quantified using a mixing matrix, which for a 2-neutrino approximation is given by:

$$\begin{pmatrix} \nu_e \\ \nu_\mu \end{pmatrix} = \begin{pmatrix} U_{e1} & U_{e2} \\ U_{\mu 1} & U_{\mu 2} \end{pmatrix} \begin{pmatrix} \nu_1 \\ \nu_2 \end{pmatrix}. \tag{1.5}$$

This mixing matrix can be parametrized as a rotation matrix:

$$\begin{pmatrix} \nu_e \\ \nu_\mu \end{pmatrix} = \begin{pmatrix} \cos\theta & \sin\theta \\ -\sin\theta & \cos\theta \end{pmatrix} \begin{pmatrix} \nu_1 \\ \nu_2 \end{pmatrix}. \tag{1.6}$$

The mixing parameters, U_{e1}, $U_{\mu 1}$, U_{e2}, and $U_{\mu 2}$ correspond to the magnitude of the mixing. The larger the mixing, the larger the amplitude of oscillation. The probability for neutrino oscillations in a two-neutrino model can be calculated from this matrix and the Schrodinger equation.

First, we express the ν_μ flavor state in terms of the mass states by multiplying out the second row of the matrix in 1.6 (and including the time dependance from solving the Schrodinger equation):

$$|\nu_\mu(t)\rangle = -\sin\theta e^{-iE_1 t} |\nu_1\rangle + \cos\theta e^{-iE_2 t} |\nu_2\rangle . \tag{1.7}$$

The probability of detecting an electron neutrino can then be expressed as:

$$|\langle \nu_e | \nu_\mu(t)\rangle|^2 = \sin^2 2\theta(1 - \cos(E_2 - E_1)t). \tag{1.8}$$

Using the relations

$$E \approx p + \frac{m^2}{2E} \tag{1.9}$$

and

$$v \approx c = \frac{L}{t}, \tag{1.10}$$

this probability can be expressed as:

$$P(\nu_\mu \to \nu_e) = \sin^2 2\theta \sin^2(1.27\Delta m^2 \frac{L}{E}), \tag{1.11}$$

where Δm^2 is the mass squared splitting between neutrino mass states $(m_2^2 - m_1^2)$, L is the distance from the neutrino source to the detector, and E is the energy of the neutrino. In this equation, L must be expressed in meters and E in MeV, as the 1.27 is not unitless; it has units of 10^{18} m/MeV. In this representation, $\sin^2 2\theta$ expresses the amplitude of oscillations and $\sin^2(1.27\Delta m^2 \frac{L}{E})$ expresses the period of oscillations. From this, we can see that the sensitivity of an experiment to certain values of Δm^2 is dependent on the range of L/E values. L is usually fixed, since most detectors and sources are immobile, and E depends on the type of neutrino source used.

The probability displayed in Equation 1.11 is an "appearance probability" for detecting electron flavored neutrinos from an initially muon flavored source ($\nu_\mu \to \nu_e$). The disappearance probability, for example the probability of muon neutrinos disappearing from a pure muon neutrino source ($\nu_\mu \to \nu_\mu$), is

$$P(\nu_\mu \to \nu_\mu) = 1 - \sin^2 2\theta \sin^2(1.27\Delta m^2 \frac{L}{E}), \tag{1.12}$$

which, as expected, is one minus the appearance probability.

1.2.2 Formalism for Three Neutrinos

Extending this to a three neutrino model, we now require a 3×3 mixing matrix:

$$\begin{pmatrix} \nu_e \\ \nu_\mu \\ \nu_\tau \end{pmatrix} = \begin{pmatrix} U_{e1} & U_{e2} & U_{e3} \\ U_{\mu 1} & U_{\mu 2} & U_{\mu 3} \\ U_{\tau 1} & U_{\tau 2} & U_{\tau 3} \end{pmatrix} \begin{pmatrix} \nu_1 \\ \nu_2 \\ \nu_3 \end{pmatrix}. \tag{1.13}$$

The U matrix can be parameterized as the three dimensional Euler rotation matrix, which has three distinct angles. In addition, there can be one complex phase:

$$U = \begin{pmatrix} c_{12}c_{13} & s_{12}c_{13} & s_{13}e^{-i\delta_{CP}} \\ -s_{12}c_{23} - c_{12}s_{23}s_{13}e^{i\delta_{CP}} & c_{12}c_{23} - s_{12}s_{23}s_{13}e^{i\delta_{CP}} & s_{23}c_{13} \\ s_{12}s_{23} - c_{12}c_{23}s_{13}e^{i\delta_{CP}} & -c_{12}s_{23} - s_{12}c_{23}s_{13}e^{i\delta_{CP}} & c_{23}c_{13} \end{pmatrix}. \tag{1.14}$$

Here, c and s represent $\sin\theta$ and $\cos\theta$ and the indices refer to the mass states and are subscripts on the Euler angles. A non-zero δ_{CP} term will manifest itself in the appearance probabilities, leading to a difference between neutrino and antineutrino appearance oscillation rates. The question of whether neutrinos violate CP is still an ongoing area of research, as discussed in Section 1.3.

The three-neutrino probability will now depend on two distinct mass squared splittings between the three mass states, m_1, m_2 and m_3. We can define the two squared splittings, $\Delta m^2_{21} = m^2_2 - m^2_1$ and $\Delta m^2_{32} = m^2_3 - m^2_2$. This leaves a third potential splitting, Δm^2_{31}, however as the difference between m_1 and m_2 is small relative to m_3, $\Delta m^2_{31} \approx \Delta m^2_{32}$.

1.2.3 Experimental Tests of Three Neutrino Oscillations

Acquiring experimental evidence for neutrino oscillations was a long road. Evidence from all of the experiments before 1998 combined with the Super Kamiokande results in that year [8] finally crystallized the theory. However, perhaps the most visually decisive result came from KamLAND [9], where the expected oscillation wave can be observed (Figure 1-3).

During these years of study, two distinct mass splittings were observed from a variety of different experiments. In the experimental literature, Δm^2_{21} was called Δm^2_{solar} because it is the mass splitting relevant for solar neutrino oscillations, and has been measured by numerous solar neutrino experiments. Likewise, Δm^2_{32} was called Δm^2_{atm}, as it was first measured by studying atmospheric neutrinos and is the mass splitting relevant for neutrinos produced in the atmosphere.

The two independent neutrino mass splittings and three mixing angles have been precisely measured by various neutrino experiments [2]. The values of Δm^2_{21} and $\sin^2(2\theta_{12})$ come from combining results from the SNO [10] and KamLAND experiments. The values of Δm^2_{32} and $\sin^2(2\theta_{23})$ were first measured by Super-Kamiokande [8], measuring neutrinos produced in the atmosphere, and later confirmed by the accelerator experiments MINOS [11], K2K [12], and T2K [13]. The last of the mixing parameters to be determined, $\sin^2(2\theta_{13})$, was measured much more recently, in 2012, by the Double Chooz [14], Daya Bay [15], and Reno [16] experiments.

The current values of these parameters are [2]:

$$\begin{aligned}
&\Delta m^2_{21}(\Delta m^2_{solar}) = (7.30 \pm 0.20) \times 10^{-5}\ eV^2 \\
&\Delta m^2_{32}(\Delta m^2_{atm}) = (2.32^{+0.12}_{-0.08}) \times 10^{-3}\ eV^2 \\
&\sin^2(2\theta_{12}) = 0.857 \pm 0.024 \\
&\sin^2(2\theta_{23}) > 0.95 \\
&\sin^2(2\theta_{13}) = 0.095 \pm 0.010
\end{aligned} \tag{1.15}$$

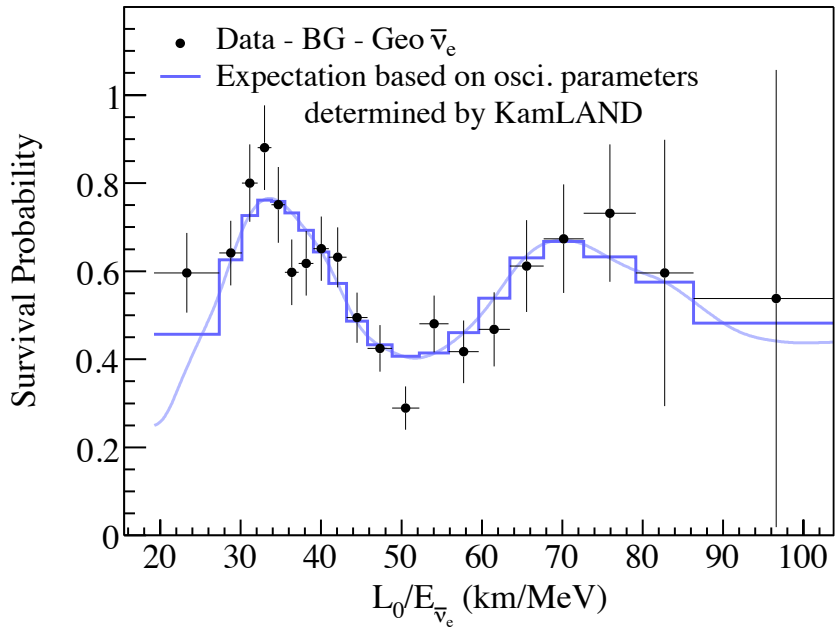

Figure 1-3: KamLAND data compared with prediction based on best fit oscillation parameters; a conclusive measurement of neutrino oscillations. From Reference [9].

The mixing angles in Equation 1.15 lead to the following mixing matrix (for a "normal mass hierarchy"– the mass states having the order illustrated in Figure 1-4), and is called the Pontecorvo-Maki-Nakagawa-Sakat (PMNS) matrix, Equation 1.13:

$$U_{PMNS} = \begin{pmatrix} 0.795 \text{ to } 0.846 & 0.513 \text{ to } 0.585 & 0.126 \text{ to } 0.178 \\ 0.205 \text{ to } 0.543 & 0.416 \text{ to } 0.730 & 0.579 \text{ to } 0.808 \\ 0.215 \text{ to } 0.548 & 0.409 \text{ to } 0.725 & 0.567 \text{ to } 0.800 \end{pmatrix}. \quad (1.16)$$

A visual representation of the flavor breakdown of the mass states is shown in Figure 1-4. The amount of color in each bar represents the amount of flavor in each mass state, which is equal to the square of the corresponding mixing matrix element. For example, the red component in the bottom bar corresponds to $|U_{e1}^2|$, the amount of electron flavor in the first mass eigenstate.

Analogous mixing had been observed in the quark sector for many years [2]. So, arguably, neutrino mixing was expected. However, unlike the analogous quark mixing matrix, the PMNS is far from diagonal, meaning that the amplitude for oscillations can be large. The connection between the quark and neutrino mixing matrices is not understood at a fundamental level, and the values of the matrix elements, in both the quark and lepton cases, are purely experimentally determined.

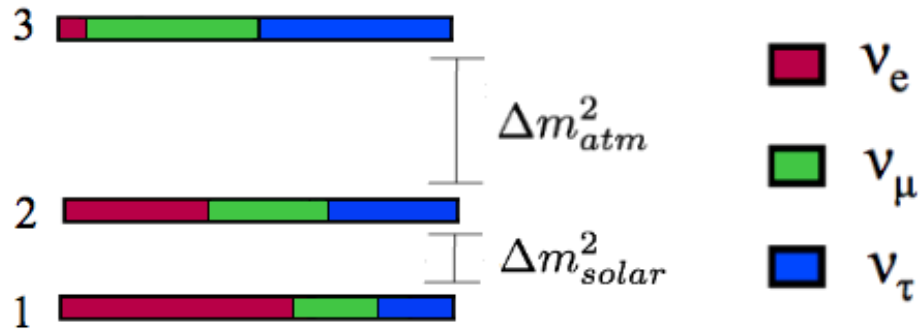

Figure 1-4: Flavor breakdown of the three mass eigenstates. For example, the red component in the bottom bar corresponds to $|U^2_{e1}|$, the amount of electron flavor in the first mass eigenstate.

1.3 Open Questions in Neutrino Physics

There are still many mysteries to be solved in the neutrino sector. This section lists some of the most prominent questions. First, we know that neutrinos have mass because oscillations measure nonzero mass splittings, but there has yet to be a direct measurement of this mass. Thus, the absolute mass scale of the neutrinos is not known. The Mainz [17] and Troitsk [18] experiments have placed the tightest limits on the mass of the lightest mass eigenstate, m_{min}, of $m_{min} < 2$ eV. The Katrin [19] experiment will come online soon with a sensitivity of 0.2 eV at 90% confidence. These three experiments probe the absolute mass scale by measuring the beta-decay spectrum endpoint of tritium using a large electrostatic spectrometer. The beta-decay spectrum endpoint is sensitive to the effective $\bar{\nu}_e$ mass, which is a superposition of the mass states weighted by the relevant mixing parameters.

A second major question is whether or not neutrinos violate CP. Recall that CP violation arises from a nonzero value of δ_{CP} in the 3×3 neutrino mixing matrix (Equation 1.14). In the muon to electron flavor appearance probability, the CP violation term is also proportional to $\sin\theta_{13}$. Therefore, the recently determined nonzero value of θ_{13} gives us an opportunity to search for CP violation. CP-violation would have important ramifications, as it is an ingredient in models which seek to explain the matter-antimatter asymmetry in the universe [2, 20]. There are a number of proposed experiments on the horizon designed to observe and measure δ_{CP}, such as LBNF [21] and DAEδALUS [22].

Another open question concerns the neutrino mass hierarchy, defined by the signs of the splittings described in Section 1.2.2. In addition to the uncertainty of the absolute mass scale, the ordering of the neutrino mass states is also unknown. We do know that $m_2 > m_1$ by the MSW effect, observed in solar neutrino studies [2]. However we are only sensitive to the absolute value of the mass splitting between m_2 and m_3 through oscillation searches. It is therefore unknown whether the masses have the ordering shown in Figure 1-4, which is known as the "normal hierarchy," or

if m_3 is below the other two, a configuration known as the "inverted hierarchy." Long baseline experiments sensitive to matter effects in the earth, such as NOνA [23] and PINGU [24], seek to determine the mass hierarchy.

Yet another mystery is whether neutrinos are Majorana particles (their own antiparticle). Inquiries have largely focused on the search for neutrinoless double beta decay [25]. For some nuclei, double beta decay is energetically favorable. This involves simultaneously converting two neutrons into protons, emitting two electrons and two electron antineutrinos:

$$n + n \rightarrow p + p + e^- + e^- + \bar{\nu} + \bar{\nu}. \tag{1.17}$$

This $Z \rightarrow Z+2$ process is possible if the nucleus in between, with $Z+1$, is disfavored because of binding energy. Such nuclei, such as ^{76}Ge, cannot undergo single beta decay at all, as the resultant nucleus from this process would have a lower binding energy than that of the double beta decay process. These nuclei are ideally suited for a neutrinoless double beta decay search. If neutrinos were Majorana, it would be possible for light Majorana neutrino exchange to occur, leading to neutrinoless double beta decay:

$$n + n \rightarrow p + p + e^- + e^- \tag{1.18}$$

This process is observable by looking for a peak at the end of the continuous kinematic distributions of the outgoing electrons. This peak corresponds to the case where the two electrons exit exactly back-to-back, thus carrying all of the energy from the process. This would indicate that there were no neutrinos exiting the interaction.

The CUORE0, NEMO, GERDA, KamLAND-Zen, and EXO-200 [26] experiments are currently operational and have set limits of $m_{\beta\beta} \lesssim 0.1$ on neutrinoless double beta decay [27, 28, 29, 30, 26]. This compares to the controversial Heidelberg-Moscow measurement [31] of $0.11 < m_{\beta\beta} < 0.56$, which has been disputed by several sources [32, 33]. New experiments, such as those proposed in References [25] and [34], are expected to lower the sensitivity to $m_{\beta\beta} \lesssim 0.01$ by 2025, probing Majorana neutrinos for the case of the inverted hierarchy. It would likely take another decade after that to make good progress in the parameter space for the normal hierarchy [34].

Lastly, there are the assorted short baseline anomalies which are the focus of the rest of this thesis. This collection of anomalies shows hints of oscillations that may correspond to at least one more mass splitting. If observed, these oscillations could confirm a hypothesis of a relatively light, non-interacting fourth neutrino flavor, the sterile neutrino. Probing this question is a primary focus of this thesis.

1.4 This Thesis on Sterile Neutrinos and the MiniBooNE Anomaly

My graduate studies focused on sterile neutrino phenomenology in general, and the MiniBooNE anomaly in particular. The outline of this thesis is as follows. I will first describe the motivation and phenomenology of sterile neutrinos. I will then describe,

in detail, the MiniBooNE anomaly, which was in part an outcome of the analyses reported in Reference [35]. This will be followed by a discussion of my global fits to the anomalous data sets, which were reported in Reference [36]. Lastly I will discuss future experiments, especially focussing on the MicroBooNE experiment, where I contributed to light collection studies reported in References [37], [38], and [39].

Chapter 2

Sterile Neutrinos

2.1 Experimental Motivation

In the 1990s, an unexpected $\nu_\mu \rightarrow \nu_e$ appearance signal was seen by the Liquid Scintillator Neutrino Detector (LSND). The signal was inconsistent with the three neutrino model and sparked a great deal of interest in the existence of a $\sim$1 eV^2 sterile neutrino. Since then, there have been several other experimental anomalies that support such a theory. We review those anomalies here. The MiniBooNE experiment will be discussed in greater detail in Chapters 3 and 4. It should be noted that along with anomalous signals, many experiments have seen null results for searches in the 1 eV^2 range. These results are reviewed in detail in Section 5.1.

2.1.1 The LSND Experiment

The primary purpose of LSND was to search for $\bar{\nu}_\mu \rightarrow \bar{\nu}_e$ oscillations at higher mass splittings than the atmospheric and solar signals. Reference [40] detected neutrinos with energies between 20 and 52 MeV at a baseline of 30 m. This value of $\frac{L}{E} \sim 1$ leads to sensitivities in Δm^2 on the order of 1 eV^2. The search was motivated by the dark matter models of the time, which postulated a neutrino with a mass greater than 1 eV. The solar and atmospheric mass splittings were not well determined at that point in time, so such an oscillation could be considered within a three neutrino model [41]. This is no longer true, as we have measured Δm^2_{32} and Δm^2_{21} to be $(7.50 \pm 0.20) \times 10^{-5}$ eV^2 and $(2.32^{+0.12}_{-0.08}) \times 10^{-3}$ eV^2 respectively [2]. Therefore, the potential signal seen by the LSND experiment cannot be due to oscillations among the three known neutrino mass states.

LSND used a decay at rest (DAR) beam at the Los Alamos Meson Physics Facility (LAMPF), which provided 800 MeV protons on target. The $\bar{\nu}_\mu$ beam used to search for $\bar{\nu}_e$ appearance was produced by muon decay at rest, with the muons stemming from pion decay at rest:

$$\begin{aligned} \pi^+ \rightarrow & \mu^+ + \nu_\mu \\ & \mu^+ \rightarrow e^+ + \nu_e + \nu_\mu \end{aligned} \tag{2.1}$$

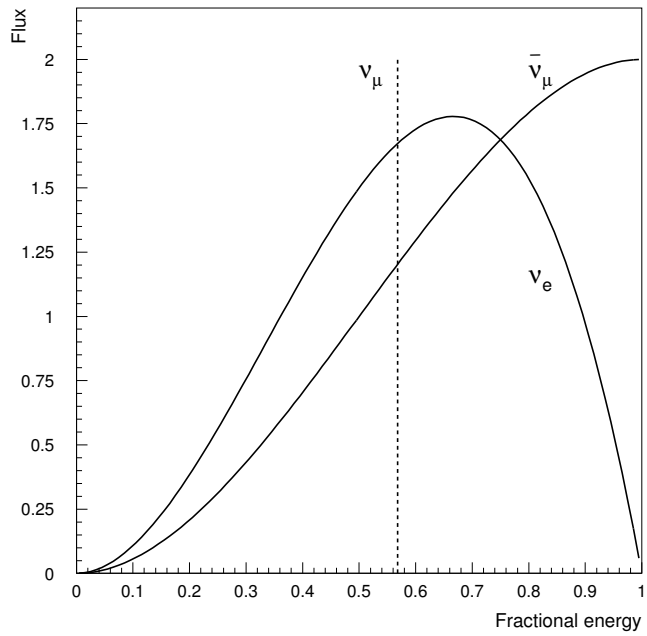

Figure 2-1: The shape of the flux of neutrinos from a DAR beam from Reference [42].

The shape of the beam flux from a DAR source is well known (Figure 2-1). The DAR source is ideal for a $\bar{\nu}_\mu \rightarrow \bar{\nu}_e$ search as there is low $\bar{\nu}_e$ contamination from negative pions. This is because the 800 MeV proton beam and water target favor positive pion production. Negative pions that are produced will generally capture before decaying, so only decay in flight π^-s contribute, and they represent a small fraction of events. In addition, most of the μ^-s from π^- decay would also be captured. The resulting $\bar{\nu}_e$ background was 8×10^{-4} of the $\bar{\nu}_\mu$ flux [40].

LSND consisted of 167 tons of mineral oil lightly doped with b-PDB scintillator surrounded by 1220 PMTs, corresponding to a photocathode coverage of 25%. LSND detected $\bar{\nu}_e$ events through inverse beta decay, $\bar{\nu}_e + p \rightarrow e^+ + n$. The $\bar{\nu}_e$ event signature consists of an initial burst of Cherenkov light from the outgoing positron, followed by a 2.2 MeV photon from the neutron capture which subsequently Compton scatters, producing a second burst of light. This sequence of events, in combination with an energy measurement of the positron, unambiguously identified the events of interest. An event within a schematic of the detector is shown in Figure 2-2.

LSND observed an excess of $87.9 \pm 22.4 \pm 6.0$ $\bar{\nu}_e$ events above background, shown in Figure 2-3. This excess was interpreted as an oscillation signal and corresponded to a best fit value of $\sin^2 2\theta = 0.003$, $\Delta m^2 = 1.2$ eV^2 within a two-neutrino approximation. The errors are illustrated by the contours in Δm^2 *vs.* $\sin^2 2\theta$ parameter space shown in Figure 2-4. Though the best fit value is at $\sin^2 2\theta = 0.003$, $\Delta m^2 = 1.2$ eV^2, the χ^2 region along the diagonal stretching towards the bottom right is shallow. The contour has that diagonal shape because simultaneously raising the amplitude of oscillation and lowering the value of Δm^2 leads to a similar oscillation curve within the data

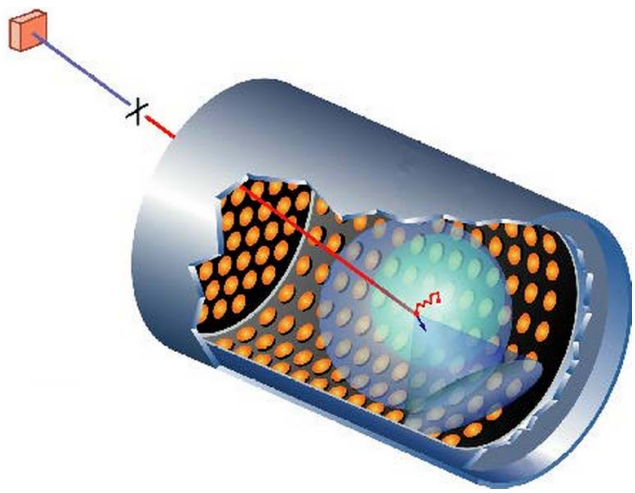

Figure 2-2: A schematic of the LSND detector with a $\bar{\nu}_e$ candidate event. The detector is lined with PMTs. An incident $\bar{\nu}_e$ (solid red line) interacts with a proton to produce an electron (jagged red line), reconstructed by its Cherenkov light, and a neutron. The neutron captures producing a photon (blue arrow).

region. The wave continues to rise (when followed from right to left on Figure 2-4) at $L/E = 0.6$ rather than falling to meet the leftmost data point like the best fit point, but still leads to a similar goodness of fit. A region with a lower bound of ~ 7 eV^2 is also allowed, corresponding to oscillations that are faster than can be resolved by the detector. This means that this region lacks sensitivity to Δm^2. An oscillation signal in this regime would manifest itself as an excess at half the oscillation amplitude.

The contours of Figure 2-4 are drawn using three different methods, which all yield equivalent results. The Feldman-Cousins method involves generating a large number of "fake" datasets by varying parameters and calculating a region which contains 90% of the fake experiments for a 90% CL contour. This method is described further in Section 4.2.2. The Constant Slice method makes a "slice" at a particular value of the log likelihood (L). The value used corresponds to errors for a particular CL within an assumption that the likelihood behaves as a two-dimensional Gaussian (with a peak at the best fit value). This is similar to the method for drawing CL regions for the global fits of Chapter 5 (described in Section 5.2). And finally, the Bayesian method assumes the prior expectation that the Δm^2 and $\sin^2 2\theta$ parameters fall within the ranges shown in Figure 2-4. Each bin within this space is assigned the weight $\delta(\Delta m^2)\delta(\sin^2 2\theta)L$ and the regions are determined by integrating over the parameter space.

The resulting analyses disfavor the null hypothesis at 3.8σ. At the time, the result was interpreted by some as first evidence for neutrino oscillations. After results from the neutrino oscillation experiments described in Section 1.2.3 became more precise, and considering that there could only be three interacting neutrinos (Section 1.1), it was determined that the only way the LSND results could be a consequence of neutrino oscillations was if there was a third mass splitting. This splitting would correspond to a fourth mass eigenstate and a fourth non-interacting, "sterile," flavor

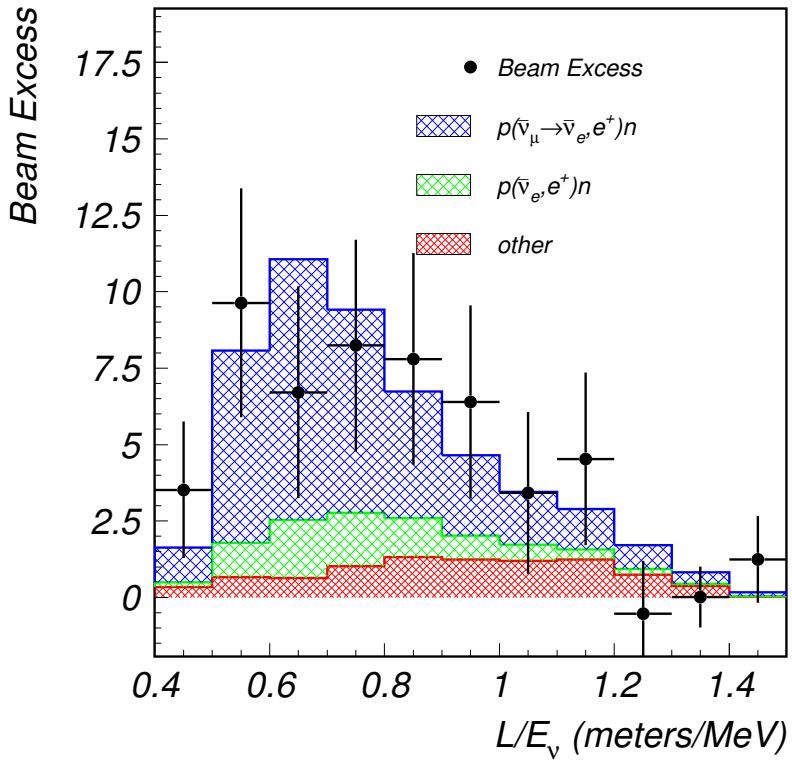

Figure 2-3: The excess beam events in the LSND experiment as a function of L/E. The data is overlaid on the expected background and expected oscillation signal for the LSND best-fit value of $\sin^2 2\theta = 0.003$, $\Delta m^2 = 1.2$ eV^2. From Reference [40].

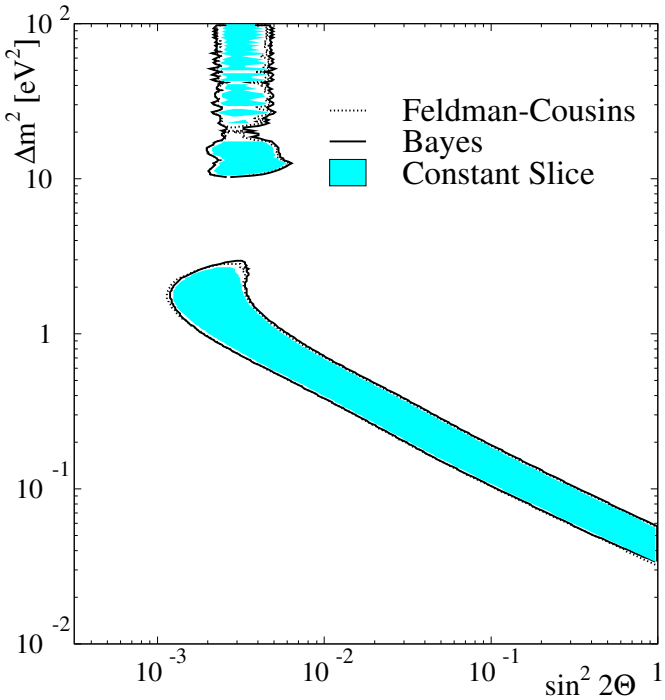

Figure 2-4: The region in Δm^2 vs. $\sin^2 2\theta$ parameter space allowed by LSND at 90% CL [40]. Three methods of drawing these contours yield equivalent results.

state.

2.1.2 MiniBooNE

The MiniBooNE Experiment was proposed in late 1997 [43] to specifically address LSND. This experiment saw signals that can be interpreted as consistent with LSND within some sterile neutrino models. This result is central to the work on this thesis, and is described in detail in Chapter 4. Therefore, we do not consider this anomaly further in this section, except to note that it is an important experimental motivation for considering the existence of sterile neutrinos.

2.1.3 The Reactor Antineutrino Anomaly

Reactors are often used as a source for antineutrino disappearance $\bar{\nu}_e \rightarrow \bar{\nu}_e$ searches, as they produce a high flux of pure electron antineutrinos [44]. Neutrino experiments located at reactors can either utilize two detectors–a near detector to measure the unoscillated flux and a far detector for the oscillation search–or rely on calculations of the antineutrino flux to search for oscillations with only a far detector. These calculations include detailed input from the reactor and are constrained by past measurements [45]. Recent updates to the expected antineutrino flux from reactors have increased the predicted rate [46], leading to an apparent deficit of antineutrino events within past experiments [47].

This deficit arises from a change in the predicted number of neutrinos per fission for ^{235}U, ^{239}Pu, ^{241}Pu, and ^{238}U. References [46] and [48] showed that weak magnetism and finite size corrections were needed. The weak magnetism correction takes into account interference between the magnetic moment distribution of the vector current and the spin distribution of the axial current. The finite size correction takes into account that there is a smaller electron density at the nucleus relative to a point-like approximation, leading to a decrease in the rate of beta decay.

The reactor flux is peaked at about 3 MeV [2], and shielding plus space in the reactor complex forces experiments to > 15 m. As a result, for high Δm^2, fast oscillations will occur. These cannot be resolved in the detector, and instead manifest as an overall deficit of events with a magnitude of half the mixing amplitude. As a result, the sterile neutrino hypothesis is one possible interpretation of the reactor anomaly.

A summary of the ratio of the observed event rate to the expected rate in various short-baseline reactor antineutrino experiments can be seen in Figure 2-5. This value is below the expectation of one for the majority of the experiments. The mean value of this ratio is 0.927 ± 0.023 [49], corresponding to a $\sim 3\sigma$ effect. The preferred regions from a fit to this data are shown in Figure 2-6.

There has been recent controversy over this anomaly due to concerns raised by Reference [50]. There are hundreds of different fission fragments, most of which beta-decay with multiple branches, leading to about 6 electron antineutrinos per fission. The resulting spectrum consists of about 6,000 endpoints, 1500 of which are forbidden transitions. The problem arises because all of the transitions used in the recent update were assumed to be Gamow-Teller (GT) transitions. It is unknown which operators determine the forbidden transitions and therefore what corrections to use for this part of the spectrum. The authors of [50] do not know if this will have an effect on the reactor predictions, so at this time it is not possible to account for this in the analysis. As the forbidden transitions distort the the shape of the neutrino spectrum, future high-statistics experiments should be sensitive to them and may be able to shed light on this issue.

2.1.4 The Gallium Experiments

The GALLEX [6] and SAGE [7] solar neutrino experiments used ^{51}Cr and ^{37}Ar sources to calibrate their detectors. The nuclei produce electron neutrinos by electron capture, producing neutrinos with distinct energies. Thus, these sources can be used for electron neutrino disappearance ($\nu_e \to \nu_e$) searches. They produce neutrinos with energies of 0.811 and 0.813 MeV for ^{37}Ar and 0.747, 0.752, 0.427, and 0.432 MeV for ^{51}Cr [51]. The neutrinos produced by these sources are lower in energy than the neutrinos in LSND or reactor experiments. They also have a comparatively short travel distance since the sources are inserted directly within the detectors (with radii of $R_{\text{GALLEX}} = 1.9$ m and $R_{\text{SAGE}} = 5$ m, and heights of $H_{\text{GALLEX}} = 0.7$ m and $H_{\text{SAGE}} = 1.5$ m). This leads to an L/E on the same order as that of LSND and therefore the ability to probe a similar range of parameter space. The results of this analysis show a 2.8σ deficit of events compared with expectation if interpreted

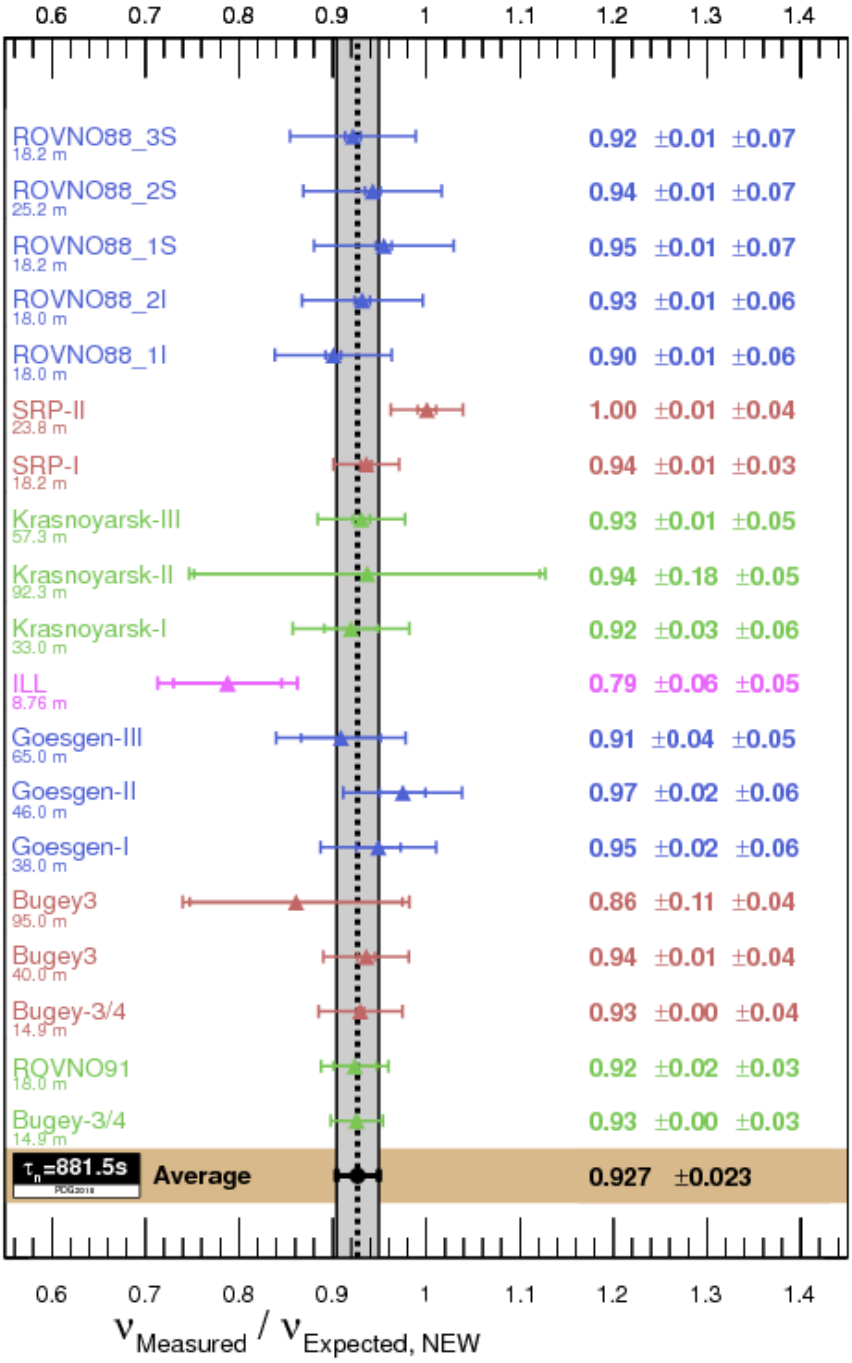

Figure 2-5: The ratio of the observed number of neutrinos divided by the expected number for a variety of short-baseline reactor experiments. For the case of no oscillations, the value should be one. From Reference [49].

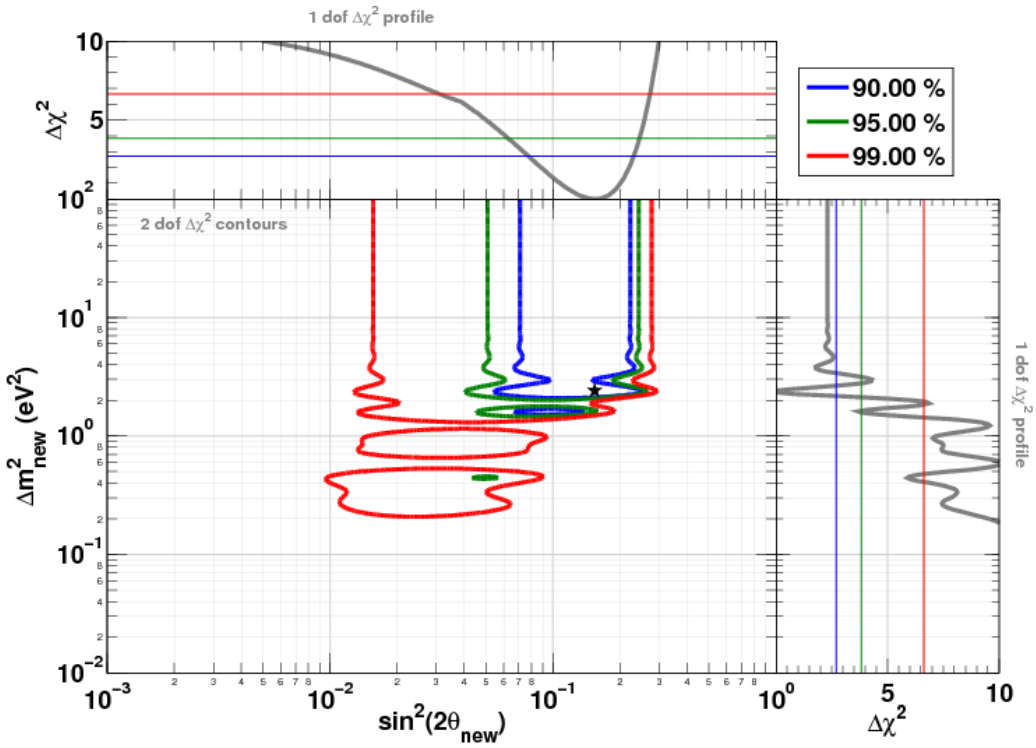

Figure 2-6: The allowed regions in Δm^2 vs $\sin^2(2\theta)$ parameter space from a fit to short-baseline reactor experiments. From Reference [49].

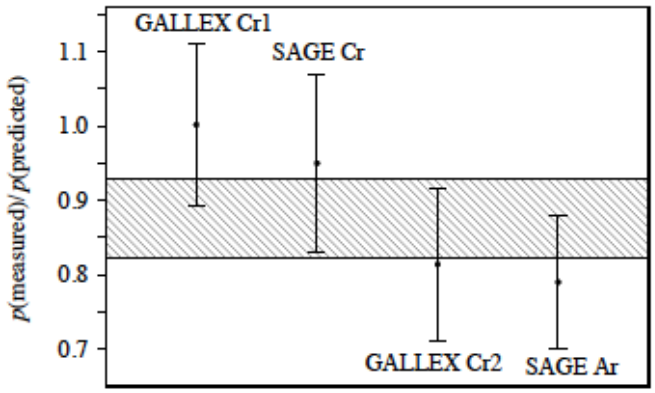

Figure 2-7: Data points showing the results from the gallium source experiments. From Reference [53]. The shaded region indicates the weighted average. In a no-oscillation scenario, p(measured)/p(predicted) should be consistent with one.

as ν_e disappearance due to oscillations in a $3+1$ scenario. The resulting fit favors oscillations with a mass splitting on the order of 1 eV^2 [52]. The best fit value is $\Delta m^2 = 2.24$ eV^2, $\sin^2 2\theta = 0.50$ and the contours can be seen in Figure 2-8.

2.1.5 Null Experiments

It is important to note that there are many null experiments, and that they are included in global analyses. The experiments included in our global fits (Chapter 5) are indicated in Table 2.1 with information as to whether or not they see a signal at 90% Confidence Level (CL). It will be shown that these experiments place strong constraints on the interpretation of the anomalies as oscillations involving sterile states. These experiments will be discussed in more detail in Section 5.1.

2.2 Phenomenology

The previously described results can be fit with null constraints within a phenomenological picture that includes sterile neutrinos. This section describes the phenomenology involved in these fits to $3+N$ models, where N is the number of sterile neutrinos considered in the fit. This thesis explores $3+1$, $3+2$, and $3+3$ models.

2.2.1 $3+1$ Model

In a $3+1$ model, $\Delta m^2_{41} \gg \Delta m^2_{31} > \Delta m^2_{21}$, so m_1, m_2, and m_3 are approximately degenerate. This means that a 3+1 model is, effectively, a simple two-neutrino model.

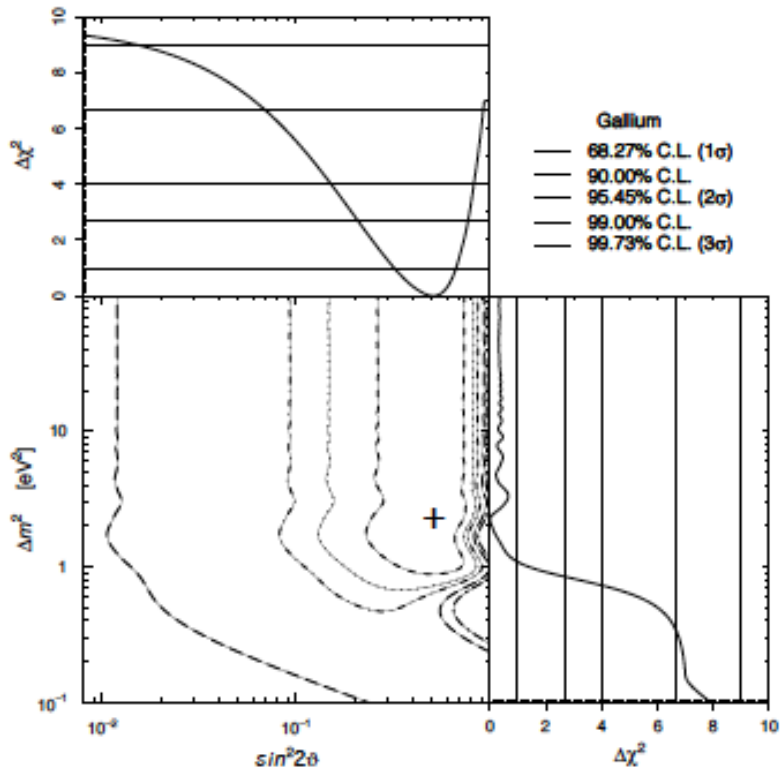

Figure 2-8: The confidence level contours and best fit value in Δm^2 vs $\sin^2(2\theta)$ parameter space from a fit to data from the GALLEX and SAGE radioactive source experiments. Also shown are the marginal $\Delta\chi^2$ for each of the two parameters. From Reference [52].

Channel	Name	Signal at 90% CL?
$\bar{\nu}_\mu \to \bar{\nu}_e$	LSND	Yes
	MiniBooNE – $\bar{\nu}$	Yes
	KARMEN	No
$\nu_\mu \to \nu_e$	NOMAD	No
	MiniBooNE – ν	Yes
	NuMI-in-MiniBooNE	No
$\bar{\nu}_e \to \bar{\nu}_e$	Bugey	Yes
$\nu_e \to \nu_e$	Gallium Anomaly	Yes
	μDAR xsec	Yes
$\bar{\nu}_\mu \to \bar{\nu}_\mu$	MINOS-CC	No
$\nu_\mu \to \nu_\tau$	NOMAD	No
$\nu_\mu \to \nu_\mu$	CCFR84	No
	CDHS	Yes
	MINOS-NC	No

Table 2.1: This table shows which experiments have a signal at 90% Confidence Level and which do not. This list encompasses all experiments included in the global fits of Chapter 5.

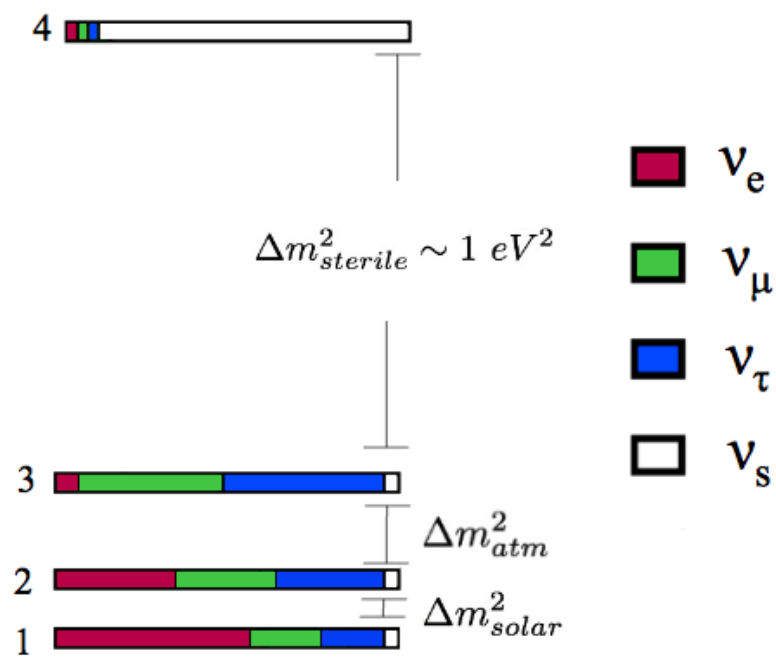

Figure 2-9: The flavor breakdown of the mass states in a $3+1$ model.

The probability for two-neutrino oscillations is usually expressed as:

$$P = \sin^2 2\theta \ \sin^2 \left(\frac{1.27\ \Delta m^2 \left(\mathrm{eV}^2\right)\ L\,(\mathrm{m})}{E\,(\mathrm{MeV})} \right) , \tag{2.2}$$

where $\sin^2 2\theta$ can also be expressed in terms of the mixing parameters as $4|U_{e4}|^2|U_{\mu 4}|^2$ for appearance experiments or $4|U_\mu|^2(1-|U_\mu|^2)$ or $4|U_e|^2(1-|U_e|^2)$ for disappearance experiments. This results in 3 parameters for a $3+1$ fit to both appearance and disappearance type experiments (Δm^2_{41}, $|U_{e4}|$, and $|U_{\mu 4}|$).

The flavor breakdown of the mass states can be visualized in Figure 2-10. $|U_{e4}|^2$ is the amount of electron flavor in the fourth mass eigenstate and so forth. In order for the values of the mixing parameters to be nonzero, and therefore in order for oscillations to occur, there must be some flavor component in the fourth mass state. Similarly, to conserve unitarity, some sterile component must also be introduced to the first three states.

Utilizing the same visual flavor breakdown as Figure 2-10, the flavor breakdown can also be visualized as physical objects created by Reference [54]. These are shown in Figure 2-10 where the top row represents the neutrino flavor eigenstates, the second row represents the neutrino mass eigenstates, and the third row represents the fourth mass eigenstate. Note that the fourth state in the figure has not yet been physically created by Reference [54] and so is just a visual schematic created in Photoshop [55]. The submission of this schematic will be submitted to Reference [54] for manufacture in the case of discovery of the sterile neutrino.

Figure 2-10: A representation of neutrino states as physical objects produced by Reference [54]. Top row: The neutrino flavor eigenstates; Middle row: The neutrino mass eigenstates (note that the number of eyes represents the index on the mass state); Bottom row: The potential fourth mass eigenstate. The fourth mass eigenstate was created using Photoshop, as it has not yet been produced by Reference [54].

2.2.2 Extending to $3+2$ and $3+3$ Models

The general form of the oscillation probability from the previous section is:

$$P(\nu_\alpha \to \nu_\beta) = \delta_{\alpha\beta} - \sum_{j<i} (4Re\{U_{\beta i}U^*_{\alpha i}U^*_{\beta j}U_{\alpha j}\} \sin^2(1.27\Delta m^2_{ij}L/E) \\ -2Im\{U_{\beta i}U^*_{\alpha i}U^*_{\beta j}U_{\alpha j}\} \sin(2.53\Delta m^2_{ij}L/E)), \tag{2.3}$$

where $\Delta m^2_{ij} = m^2_j - m^2_i$, α and β are flavor-state indices (e, μ, τ), and i and j are mass-state indices $(1, 2, 3$ in the three-neutrino case, though Eq. 2.3 holds for N-neutrino oscillations). Writing this out for the case of a $3+2$ model yields:

$$\begin{aligned} P(\nu_\alpha \to \nu_\beta) \simeq & \\ & - 4|U_{\alpha 5}||U_{\beta 5}||U_{\alpha 4}||U_{\eta 4}| \cos\phi_{54} \sin^2(1.27\Delta m^2_{54}L/E) \\ & + 4(|U_{\alpha 4}||U_{\beta 4}| + |U_{\alpha 5}||U_{\beta 5}| \cos\phi_{54})|U_{\alpha 4}||U_{\beta 4}| \sin^2(1.27\Delta m^2_{41}L/E) \\ & + 4(|U_{\alpha 4}||U_{\beta 4}| \cos\phi_{54} + |U_{\alpha 5}||U_{\beta 5}|)|U_{\alpha 5}||U_{\beta 5}| \sin^2(1.27\Delta m^2_{51}L/E) \\ & + 2|U_{\beta 5}||U_{\alpha 5}||U_{\beta 4}||U_{\alpha 4}| \sin\phi_{54} \sin(2.53\Delta m^2_{54}L/E) \\ & + 2(|U_{\alpha 5}||U_{\beta 5}| \sin\phi_{54})|U_{\alpha 4}||U_{\beta 4}| \sin(2.53\Delta m^2_{41}L/E) \\ & + 2(-|U_{\alpha 4}||U_{\beta 4}| \sin\phi_{54})|U_{\alpha 5}||U_{\beta 5}| \sin(2.53\Delta m^2_{51}L/E), \end{aligned} \tag{2.4}$$

and

$$\begin{aligned} P(\nu_\alpha \to \nu_\alpha) \simeq \quad & 1 - 4|U_{\alpha 4}|^2|U_{\alpha 5}|^2 \sin^2(1.27\Delta m^2_{54}L/E) \\ & - 4(1 - |U_{\alpha 4}|^2 - |U_{\alpha 5}|^2)(|U_{\alpha 4}|^2 \sin^2(1.27\Delta m^2_{41}L/E) \\ & + |U_{\alpha 5}|^2 \sin^2(1.27\Delta m^2_{51}L/E)). \end{aligned} \tag{2.5}$$

for the cases of appearance and disappearance respectively. This is now analogous to the three-neutrino case since the first three states are still degenerate. As such, the usual CP-violating phase, here expressed as ϕ_{54}, appears for appearance-type experiments and will flip sign for antineutrinos.

Extending this further, to a $3+3$ model,

$$\begin{aligned}
P(\nu_\alpha \to \nu_\beta) \simeq &- 4|U_{\alpha5}||U_{\beta5}||U_{\alpha4}||U_{\beta4}|\cos\phi_{54}\sin^2(1.27\Delta m^2_{54}L/E) \\
&- 4|U_{\alpha6}||U_{\beta6}||U_{\alpha4}||U_{\beta4}|\cos\phi_{64}\sin^2(1.27\Delta m^2_{64}L/E) \\
&- 4|U_{\alpha5}||U_{\beta5}||U_{\alpha6}||U_{\beta6}|\cos\phi_{65}\sin^2(1.27\Delta m^2_{65}L/E) \\
&+4(|U_{\alpha4}||U_{\beta4}| + |U_{\alpha5}||U_{\beta5}|\cos\phi_{54} + |U_{\alpha6}||U_{\beta6}|\cos\phi_{64})|U_{\alpha4}||U_{\beta4}|\sin^2(1.27\Delta m^2_{41}L/E) \\
&+4(|U_{\alpha4}||U_{\beta4}|\cos\phi_{54} + |U_{\alpha5}||U_{\beta5}| + |U_{\alpha6}||U_{\beta6}|\cos\phi_{65})|U_{\alpha5}||U_{\beta5}|\sin^2(1.27\Delta m^2_{51}L/E) \\
&+4(|U_{\alpha4}||U_{\beta4}|\cos\phi_{64} + |U_{\alpha5}||U_{\beta5}|\cos\phi_{65} + |U_{\alpha6}||U_{\beta6}|)|U_{\alpha6}||U_{\beta6}|\sin^2(1.27\Delta m^2_{61}L/E) \\
&+ 2|U_{\beta5}||U_{\alpha5}||U_{\beta4}||U_{\alpha4}|\sin\phi_{54}\sin(2.53\Delta m^2_{54}L/E) \\
&+ 2|U_{\beta6}||U_{\alpha6}||U_{\beta4}||U_{\alpha4}|\sin\phi_{64}\sin(2.53\Delta m^2_{64}L/E) \\
&+ 2|U_{\beta6}||U_{\alpha6}||U_{\beta5}||U_{\alpha5}|\sin\phi_{65}\sin(2.53\Delta m^2_{65}L/E) \\
&+2(|U_{\alpha5}||U_{\beta5}|\sin\phi_{54} + |U_{\alpha6}||U_{\beta6}|\sin\phi_{64})|U_{\alpha4}||U_{\beta4}|\sin(2.53\Delta m^2_{41}L/E) \\
&+2(-|U_{\alpha4}||U_{\beta4}|\sin\phi_{54} + |U_{\alpha6}||U_{\beta6}|\sin\phi_{65})|U_{\alpha5}||U_{\beta5}|\sin(2.53\Delta m^2_{51}L/E) \\
&+2(-|U_{\alpha4}||U_{\beta4}|\sin\phi_{64} - |U_{\alpha5}||U_{\beta5}|\sin\phi_{65})|U_{\alpha6}||U_{\beta6}|\sin(2.53\Delta m^2_{61}L/E)\ . \quad (2.6)
\end{aligned}$$

CP violation appears in Eq. 2.6 in the form of the three phases: ϕ_{54}, ϕ_{64}, and ϕ_{65} defined by:

$$\phi_{ij} = \arg(U_{ei}U^*_{\mu i}U^*_{ej}U_{\mu j}), \quad (2.7)$$

where again, for $\nu \to \bar{\nu}$, $\phi \to -\phi$.

In the case of disappearance ($\alpha \equiv \beta$), the survival probability becomes:

$$\begin{aligned}
P(\nu_\alpha \to \nu_\alpha) \simeq &1 - 4|U_{\alpha4}|^2|U_{\alpha5}|^2\sin^2(1.27\Delta m^2_{54}L/E) \\
&- 4|U_{\alpha4}|^2|U_{\alpha6}|^2\sin^2(1.27\Delta m^2_{64}L/E) - 4|U_{\alpha5}|^2|U_{\alpha6}|^2\sin^2(1.27\Delta m^2_{65}L/E) \\
&- 4(1 - |U_{\alpha4}|^2 - |U_{\alpha5}|^2 - |U_{\alpha6}|^2)(|U_{\alpha4}|^2\sin^2(1.27\Delta m^2_{41}L/E) \\
&+ |U_{\alpha5}|^2\sin^2(1.27\Delta m^2_{51}L/E) + |U_{\alpha6}|^2\sin^2(1.27\Delta m^2_{61}L/E)). \quad (2.8)
\end{aligned}$$

2.3 Sterile Neutrinos in Cosmology

Cosmological observations are sensitive to the existence of sterile neutrinos in the form of N_{eff}, the total number of neutrino species that contribute to the radiation energy density of the early universe [49] by:

$$\rho_\nu = N_{eff}\frac{7\pi^2 T_\nu^4}{120}, \quad (2.9)$$

where ρ_ν is the neutrino energy density after e^+e^- annihilation in the radiation-dominated era and T_ν is the neutrino temperature after e^+e^- annihilation (related to the photon temperature by $T_\nu = (4/11)^{1/2}T_\gamma$). Neutrinos can be treated like photons rather than matter in this model due to their relativistic nature.

The energy density of neutrinos affects the expansion rate of the universe during

this era by:

$$H^2(t) \simeq \frac{8\pi G}{3}(\rho_\gamma + \rho_\nu) \tag{2.10}$$

where $H(t)$ is the Hubble constant and ρ_γ is the (well-measured) photon energy density.

Predictions for parameters such as the ratios of light elements in the early universe, CMB anisotropies, and large-scale structure distributions are dependent on N_{eff} [2]. Therefore, cosmological measurements of these parameters are sensitive to N_{eff}. Current cosmological data allow for and in some cases even favor light sterile neutrinos [49]. While measurements of $N_{eff} > 3.046.$ [1] may be an indicator of the existence of sterile neutrinos, there are other processes that could lead to this result. For example, any process that changes the thermal abundance of neutrinos could lead to $N_{eff} \neq 3.046$. In addition, the existence of another light, neutral particle that contributes to the relativistic energy density of the early universe could lead to measurements of $N_{eff} > 3.046$ [2, 49].

Likewise, measurements confirming the prediction of $N_{eff} = 3.046$ do not necessarily rule out sterile neutrinos, as there are a variety of theories where neutrinos do not thermalize, or partially thermalize, in the early universe. For example, suppression of sterile neutrino production may occur due to a thermal MSW effect or hidden sector gauge forces [56, 57]. These processes could cause N_{eff} to be insensitive to sterile neutrinos.

Limits can also be placed on $\Sigma(m_\nu)$, the total sum of the masses of all neutrino species. Models with one thermalized sterile neutrino currently place limits ranging from $m_s < 0.23$ eV to $m_s < 0.66$ eV [58], depending on which datasets and constraints are considered. Masses up to $m_s = 1$ eV can be accommodated with small modifications to the ΛCDM model [49]. However the addition of additional (thermalized) heavy sterile neutrinos are disfavored.

The above predictions shift slightly if one considers the effects of the recent BICEP-2 result. This is explored in Reference [59].

[1] The standard model predicts $N_{eff} = 3.046$ due to a correction based on the energy dependence of neutrino interactions. This means that for three neutrino species, the total neutrino energy density is a factor of 3.046 more than the case of one neutrino species that decouples before e^+e- annihilation.

Chapter 3

Detecting Neutrinos with MiniBooNE

The MiniBooNE experiment was proposed in 1999 to study the LSND anomaly. Data was taken from 2002 through 2012 in both neutrino and antineutrino modes. The details of the experiment are described in this section.

3.1 The Booster Neutrino Beam

MiniBooNE is located along the Booster Neutrino Beam (BNB) at Fermilab. Protons are first accelerated to 8 GeV in the Fermilab booster ring and then transferred to the MiniBooNE target hall. The protons then impinge on a beryllium target located inside of a magnetic focusing horn. Pions and kaons produced in this interaction decay in flight within a 50 m decay region. Neutrinos from this decay continue on to the detector, while the muons and other particles produced in the meson decays are absorbed in a 3.8 m beam dump. The additional 474 m of earth makes it impossible for any of the other particles to reach the MiniBooNE detector. To investigate the LSND anomaly, MiniBooNE roughly preserves the $L/E \sim 1$ ratio of LSND. The flux of the beam used in the analysis is primarily between 200 and 1500 MeV, peaking at 700 MeV, and the distance is 540 m.

The simulation of the beam uses a GEANT4 [60] Monte Carlo and takes into account detailed information about the geometry of the beamline, following protons from the initial beam through p-Be interactions with the 70 cm long by 0.5 cm radius beryllium target. The pion production cross section for this interaction was measured by HARP [61], which used the same beam momentum as MiniBooNE, about 9 GeV/c, and E910 [62], which used beam momenta of 6.4, 12.3, and 17.5 GeV/c. A Sanford-Wang [63] parameterization is used in conjunction with the HARP and E910 data to extrapolate differential cross sections for pion production at a range of energies.

The simulation then models the propagation and magnetic focusing of the secondary pions and kaons produced in the p-Be interaction, followed by the decay of these mesons. The focusing horn uses a current of +174 kA in neutrino mode, focusing positively charged mesons which will decay into neutrinos, and defocusing negatively

charged mesons which will decay into antineutrinos. In antineutrino mode, the sign of this current is reversed, to -174 kA, to focus negatively charged mesons and defocus positively charged mesons. The contamination of mesons of the opposite sign is much higher in antineutrino mode due to the higher number of positive mesons produced by the p-Be interaction. In addition, negative mesons capture more quickly due to their electromagnetic attraction to positive nuclei.

The forward-going mesons continue on to a 50 m decay pipe where they decay into neutrinos and antineutrinos. Any particles remaining (other than the neutrinos and antineutrinos) are absorbed by a beam dump located at the end of this decay pipe. The simulation accounts for the lifetime and branching ratios of the mesons, calculating the resultant neutrino energy and decay position. The total predicted flux of all neutrino species for neutrino and antineutrino mode is shown in Figure 3-1 and is described in more detail in Reference [64].

3.2 The MiniBooNE Detector

MiniBooNE is a spherical Cherenkov detector with a diameter of 12.2 m, filled with 818 tons of Marcol 7 mineral oil. When a charged particle travels faster than the speed of light in a material, in this case mineral oil, it produces Cherenkov radiation. This light radiates in the shape of a cone in the forward direction, with an angle of

$$\theta = \cos^{-1}(\frac{c}{nv}), \tag{3.1}$$

where c is the speed of light, n is the index of refraction of the material, and v is the velocity of the light. The higher index of refraction of the mineral oil compared with water ($n = 1.47$ *vs.* $n = 1.33$) leads to a lower Cherenkov threshold (enabling detection of lower energy particles), as the threshold velocity for Cherenkov light production is $v = c/n$. This also leads to more Cherenkov light for particles of a given energy. The higher Cherenkov angle also leads to a more accurate reconstruction of particle positions inside of the detector.

Rings of Cherenkov light are mapped across 1280 R1408 and R5912 8" Hamamatsu Photomultiplier Tubes (PMTs) placed uniformly along the inside of the detector at a radius of 5.7 m. This results in an 11.3% photocathode coverage. An additional 240 PMTs were used in an outer veto region for rejection of cosmic rays, with an efficiency measured to be 99.987% of the 10 kHz of cosmic ray events that reach the detector through the 3 m overburden. There is also a muon tracker located above the detector and six scintillation cubes located within the volume of mineral oil which are used for muon-energy calibration using the muon events which decay within the cubes. The 1198 R1408 PMTs were recycled from the LSND experiment and the remaining PMTs were newly purchased for MiniBooNE. The PMT efficiencies and responses were externally characterized using a pulsed LED and are described in [65]. In situ calibration was done using a ludox ball and cosmic rays [66]. A schematic of the detector and detector hall can be seen in Figure 3-2.

The simulation of the detector uses GEANT3 [67] and accounts for the detec-

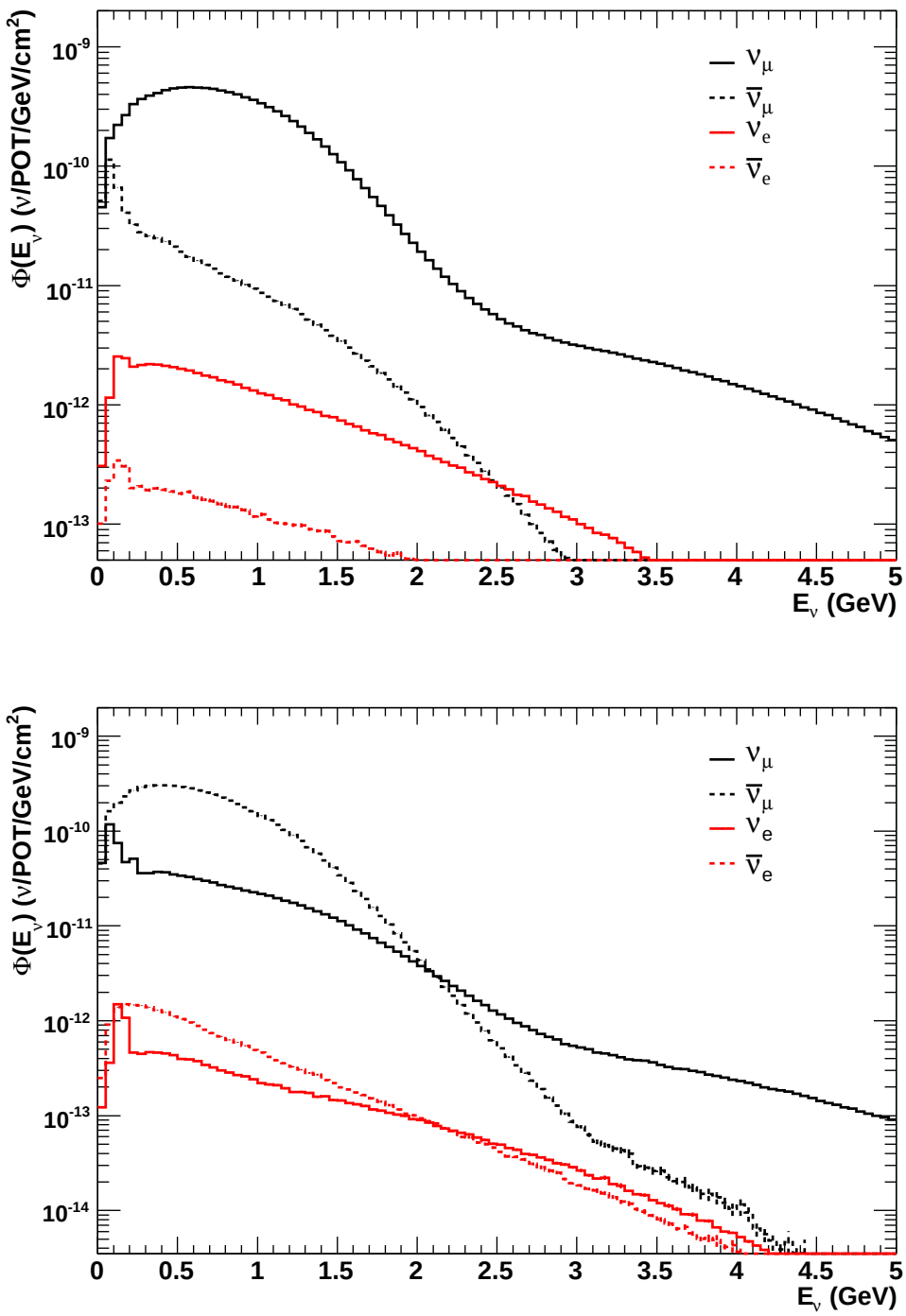

Figure 3-1: The neutrino (top) and antineutrino (bottom) flux predictions for all neutrino species at MiniBooNE from Reference [64]. Note that there is contamination of antineutrinos in neutrino mode and neutrinos in antineutrino mode. The effect of this "wrong-sign" component on the analysis is further discussed in Section 3.7.4.

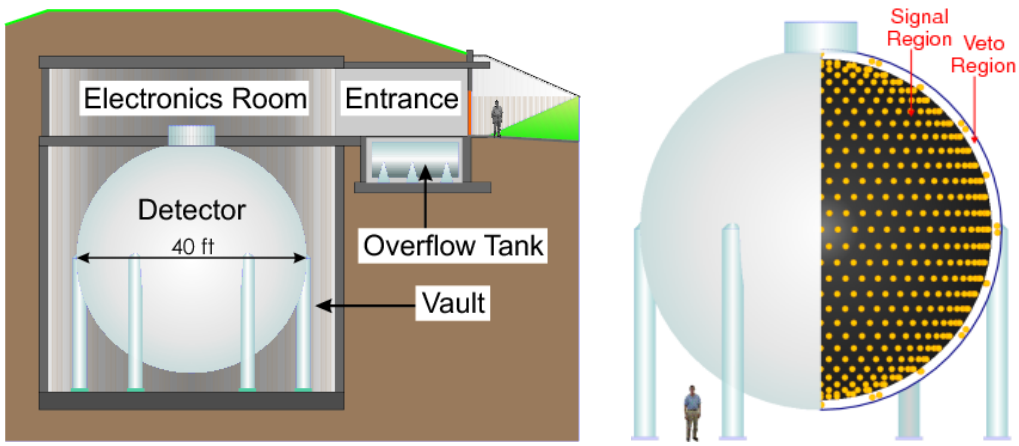

Figure 3-2: A schematic of the MiniBooNE detector hall and detector with Bill Louis [69] standing next to it for scale. From Reference [70].

tor geometry, the properties of the mineral oil, the air-filled concrete housing of the detector, and the surrounding dirt. All aspects of the neutrino interaction are simulated, including the generation and propagation of resultant particles and individual Cherenkov and scintillation photons. This includes the interaction of the photons with the photocathode of the PMT, including information about PMT efficiencies. The detector simulation is described in detail in Reference [68].

3.3 Cherenkov Rings in MiniBooNE

The charged particles produced in neutrino interactions primarily generate Cherenkov light, as well as a small amount of scintillation light, in the detector. The resultant Cherenkov light patterns are called "Cherenkov rings" and are used for particle ID.

To determine the flavor of the incident neutrino, we must identify the charged lepton that emerges from the interaction. If an electron is detected, we know that an electron neutrino initiated the interaction. If a muon is detected, the initiator was a muon neutrino. These charged leptons produce different signatures in the detector. Specifically, they produce Cherenkov rings with distinct properties. Because of their smaller mass, electrons tend to radiate more than muons. Muons primarily lose energy through ionization. As a result, for particles of the same energy, the muon travels a longer distance. Muons also suffer little multiple scattering, again because of their large mass. As a result, the muon produces a ring with a sharp, solid outer edge, which becomes "filled-in" as the muon approaches the edge of the detector and slows to a stop. An electron, on the other hand, creates short tracks, undergoing multiple scattering and modest bremsstrahlung as it travels, producing a thin, "fuzzy" ring. An example of an electron ring and a muon ring in the detector can be seen in Figure

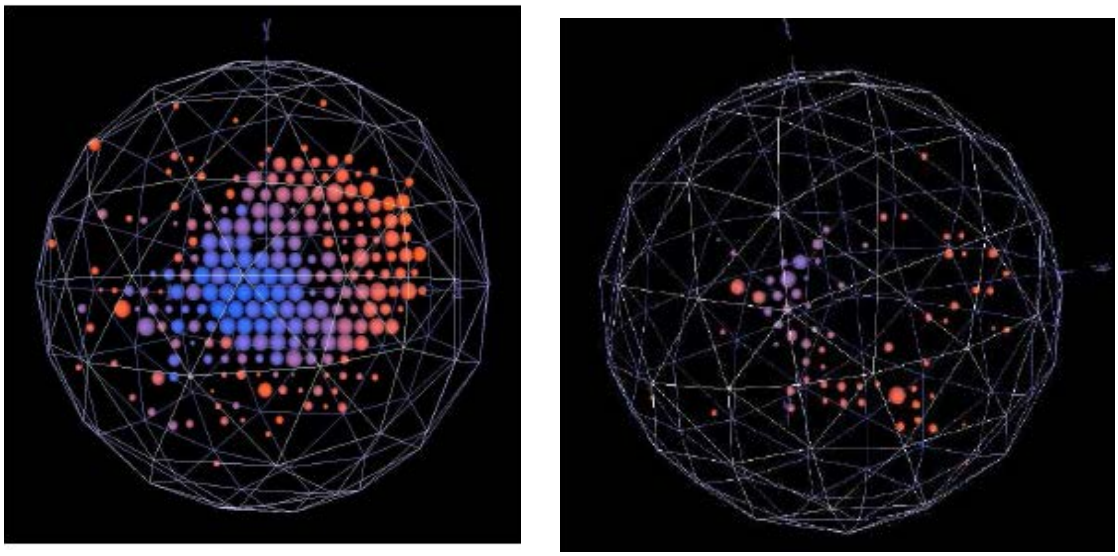

Figure 3-3: An example of a muon Cherenkov ring (left) and electron Cherenkov ring (right) in the MiniBooNE detector. Muon rings are sharp and thick or filled in due to the long tracks of the muon, while electron rings are thin and fuzzy due to the short tracks of electrons and the electron's tendency to scatter.

.

3-3.

A major drawback of Cherenkov detectors is their inability to distinguish electrons from photons. Both electrons and photons initiate an electromagnetic shower and produce "fuzzy" Cherenkov rings in the detector. This causes misidentification of single photons as electron neutrino events. Backgrounds associated with photons identified as electrons are described in Section 3.7.

3.4 Types of Neutrino Interactions in MiniBooNE

Event interactions are simulated in the detector using the NUANCE [71] event generator. NUANCE includes all aspects of neutrino interactions, including cross section models in the energy range from $\sim$ 100 MeV to 1 TeV, and nuclear models describing final-state interactions and bound nucleon states. Bound nucleons, such as those in the carbon nuclei of the mineral oil, are assumed to be independent and described by the Fermi gas model. Section 4.6 addresses this assumption in relation to the oscillation analysis. The main types of interactions relevant to the oscillation analysis are quasi-elastic scattering and resonance production. There is also a very small contribution from deep inelastic scattering. A summary of charged current cross section measurements compared with prediction are shown in Figure 3-4.

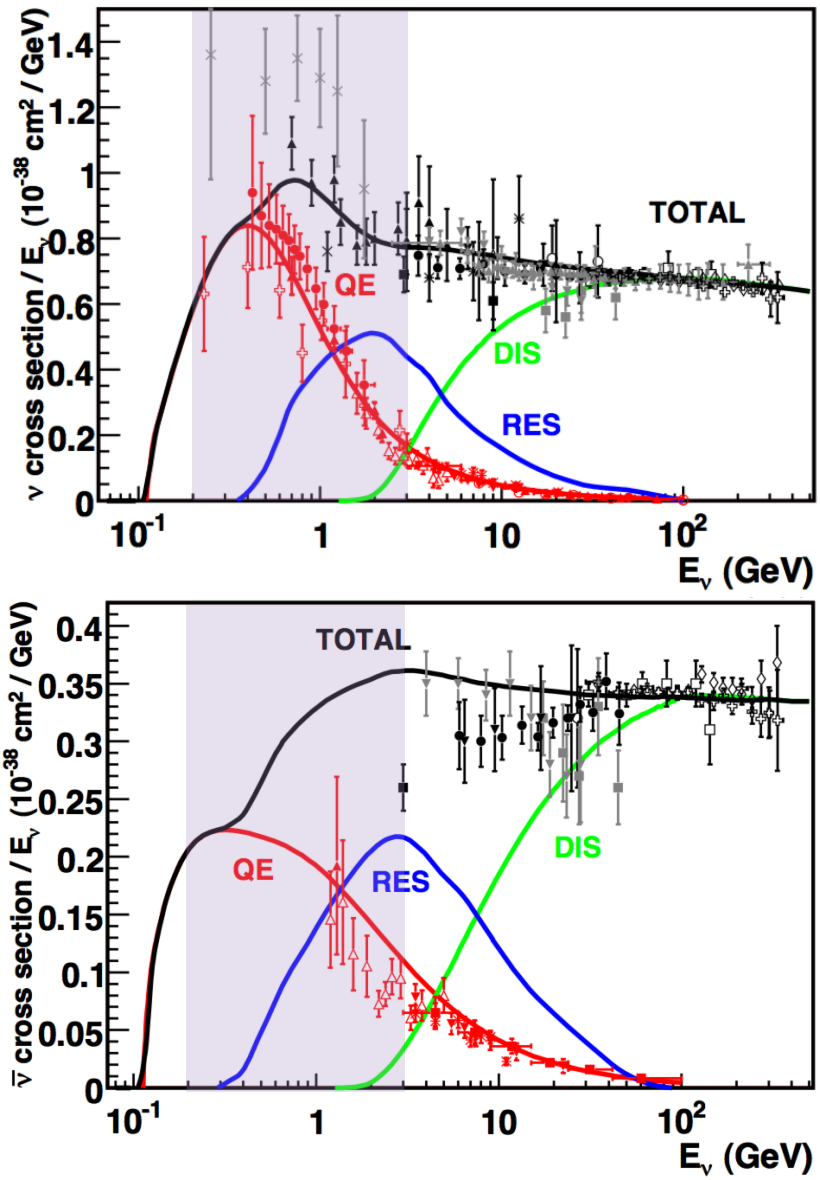

Figure 3-4: Measured and predicted CC cross-sections per nucleon as a function of neutrino energy for neutrinos (top) and antineutrinos (bottom) from Reference [72]. The processes indicated on the plot are Quasi-Elastic Scattering (QE), Resonance Production (RES) and Deep Inelastic Scattering (DIS). The shaded region represents the range of energies relevant to MiniBooNE.

3.4.1 Quasi-Elastic Scattering

Recall from Chapter 1 that when a two-body Charged-Current (CC) interaction occurs, where a neutrino (antineutrino) scatters off of a neutron (proton), the process is called Charged Current Quasi-Elastic Scattering (CCQE). For neutrinos, the interaction produces a negatively charged lepton:

$$\nu_l + n \rightarrow p + l^-.$$

The reverse of this process, for incident antineutrinos, is:

$$\bar{\nu}_l + p \rightarrow n + l^+.$$

These events are identified by the outgoing charged lepton produced in the interaction, which has the same flavor as that of the incident neutrino due to lepton flavor conservation. Generally, the outgoing nucleon does not produce sufficient light to observe, since MiniBooNE has no scintillator doping. CCQE dominates at energies less than about 2 GeV, and accounts for about 42% of all events observed in MiniBooNE. CCQE is the channel which produces signal events for the the oscillation analysis. The Feynman diagrams for CCQE events can be seen in Figure 3-5.

The CCQE scattering cross section at energies on the order of 1 GeV has been measured by MiniBooNE to be about $\sim 30\%$ higher than prediction [73, 74]. This is in contrast to measurements at higher (10s of GeV) energies which are sitting lower than prediction [75]. Early measurements were made using deuterium, a simple nucleus, which resulted in good agreement with V-A theory. Recent experiments, however, use higher-A nuclei, which are affected by more complicated nuclear interactions. It is believed that the independent-particle models on which most scattering predictions are based are insufficient. Tension in the data may be resolved by accounting for nuclear effects that were previously thought not to play a role [72]. Data from current and future experiments, such as MINERvA, T2K, and NOvA, are expected to help us understand this issue in the near future [76]. This discrepancy is not expected to affect the MiniBooNE oscillation analysis substantially because we use measured ν_μ data to constrain our ν_e prediction (Section 4.1.3). A sample model including these affects was tested in Reference [35] and showed no significant effect.

3.4.2 Resonance Production

Resonance production occurs when neutrinos excite the target nucleon, inducing a resonance state such as a Δ particle. These events are identified by the final state nucleons and mesons produced after the resonance decays, which is most often to a nucleon and single pion:

$$\begin{aligned} \nu_\mu + N \rightarrow \mu^- + \Delta & \\ \Delta \rightarrow \pi + N' & \end{aligned} \tag{3.2}$$

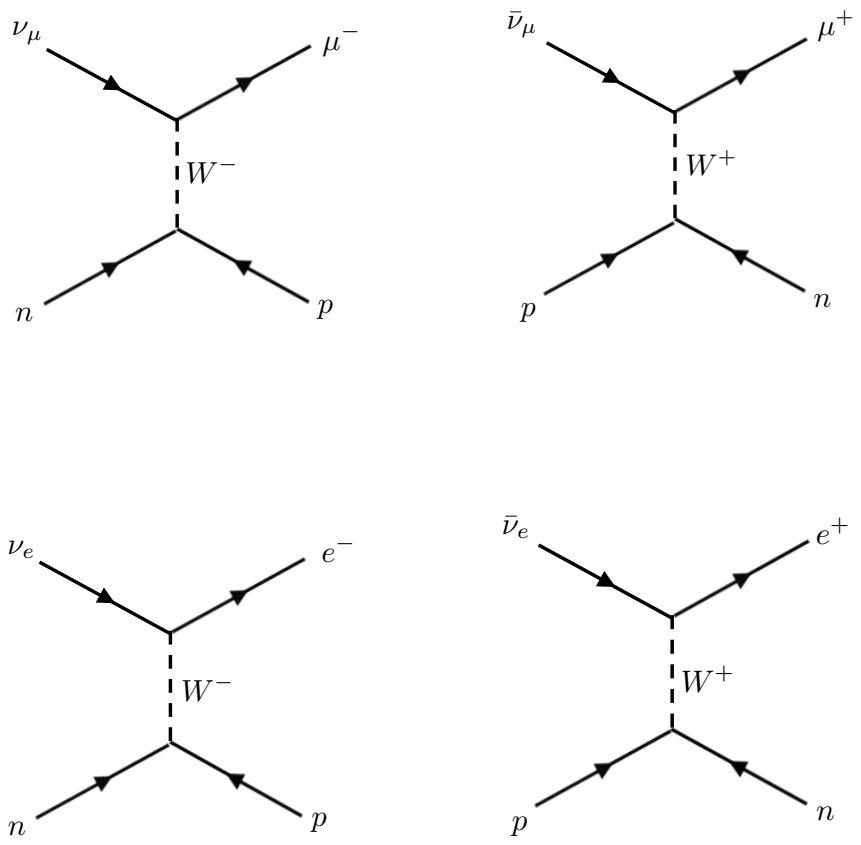

Figure 3-5: Feynman diagrams for CCQE interactions. The top and bottom rows depict muon and electron flavor events respectively, while the left and right columns show neutrino and antineutrino interactions respectively.

where N and N' represent protons or neutrons. There are three possible CC reaction channels for each neutrinos and antineutrinos and four possible NC channels [72]:

$$\begin{aligned}
\nu_\mu + p &\rightarrow \mu^- + p + \pi^+ & \bar{\nu}_\mu + p &\rightarrow \mu^+ + p + \pi^- \\
\nu_\mu + n &\rightarrow \mu^- + p + \pi^0 & \bar{\nu}_\mu + p &\rightarrow \mu^+ + n + \pi^0 \\
\nu_\mu + n &\rightarrow \mu^- + n + \pi^+ & \bar{\nu}_\mu + n &\rightarrow \mu^+ + n + \pi^-
\end{aligned}$$

$$\begin{aligned}
\nu_\mu + p &\rightarrow \nu_\mu + p + \pi^0 & \bar{\nu}_\mu + p &\rightarrow \bar{\nu}_\mu + p + \pi^0 \\
\nu_\mu + p &\rightarrow \nu_\mu + n + \pi^+ & \bar{\nu}_\mu + p &\rightarrow \bar{\nu}_\mu + n + \pi^+ \\
\nu_\mu + n &\rightarrow \nu_\mu + n + \pi^0 & \bar{\nu}_\mu + n &\rightarrow \bar{\nu}_\mu + n + \pi^0 \\
\nu_\mu + n &\rightarrow \nu_\mu + n + \pi^- & \bar{\nu}_\mu + n &\rightarrow \bar{\nu}_\mu + p + \pi^-.
\end{aligned}$$

The historical measurements of CC and NC pion production are summarized in Reference [72]. NC π^0 production is important for the MiniBooNE oscillation analysis since it is the largest ν_μ-induced background in the analysis, particularly at low energies, as will be discussed in Section 3.7.1.

Coherent pion production, a process where the incident neutrino scatters from the entire nucleus, can also lead to single pion final states:

$$\begin{aligned}
\nu_\mu + A &\rightarrow \nu_\mu + A + \pi^0 & \bar{\nu}_\mu + A &\rightarrow \bar{\nu}_\mu + A + \pi^0 \\
\nu_\mu + A &\rightarrow \mu^- + A + \pi^+ & \bar{\nu}_\mu + A &\rightarrow \mu^+ + A + \pi^-.
\end{aligned}$$

These events are too low in energy to produce nuclear recoil. This is because there is only a small amount of energy transferred to the target nucleus and the resulting pions are forward-scattered.

3.4.3 Deep Inelastic Scattering

Another class of neutrino interactions, dominant at higher energies than those relevant to MiniBooNE, is deep inelastic scattering (DIS). DIS occurs when a neutrino interacts with an individual quark in a nucleon, which typically occurs for higher energies. This process results in a hadronic shower. Such an interaction is difficult to reconstruct in a Cherenkov detector as the rings from the hadronic debris will overlap.

3.5 Final State Interactions

Final state interactions refer to the processes which occur after the neutrino interacts in the detector. They are often effectively instantaneous and all that is observed is the final state after these interactions occur. The resultant particles from neutrino interactions are propagated by NUANCE, which takes into account any re-interactions to determine the likelihood of observable final states. The most common processes

that require this consideration are pion absorption:

$$\pi^{\pm} + X \rightarrow X' \tag{3.3}$$

and pion charge exchange:

$$\pi^{\pm} + X \rightleftarrows \pi^{0} + X'. \tag{3.4}$$

Pion absorption leads to a final state without a pion, leading to a state that is identical to CCQE. This is therefore an irreducible background in the oscillation analysis.

3.6 Event Reconstruction

Reconstruction of ν_e and ν_μ CCQE events rely on the identification and measurement of the outgoing charged lepton. Events are reconstructed based on parameters such as the topology of their Cherenkov and scintillation light, the distance from the detector, and the angle with respect to the beam direction.

3.6.1 Identifying Events

Neutrino events are located in MiniBooNE by identifying bursts of light within a window coinciding with the booster neutrino beam, which is pulsed with a duty factor of 2.5 $\times 10^{-5}$. Multiple bursts within one beamspill are taken to be from the same neutrino event, and are called subevents. A burst must have at least 10 PMT hits, where consecutive hits cannot be separated by more than 10 ns, to be considered a subevent. A PMT hit is defined as a charge of $\geq$ 2 mV, which corresponds to about 0.1 photoelectrons, and is the threshold at which the charge and timing information are read out. The analog-to-digital converter (ADC) stores data for 200 μs when it receives a trigger for data-taking, such as the beam trigger.

Energy information for each particle is determined by the number of PMTs hit and the amount of charge on each PMT. If there are more than 200 hits, the subevent is most likely from a higher energy particle, like a muon. If less than 200 hits, the subevent is more likely to be a lower energy particle such as a Michel electron. The muon capture rate is $\sim$ 8% in MiniBooNE, with 6.6% of the captured muons leading to a Michel-like event [74]. A combination of the event having the correct number and timing of subevents with each subevent containing the expected amount of PMT hits is the first step towards event identification. A major source of uncertainty arises when one or more of the subevents are lost, which can make the event look like a different type of event. This can be accounted for through detector simulations, where the mechanisms for such losses can be explored and statistically characterized.

3.6.2 Particle Track and Energy Reconstruction

Another aspect of event reconstruction is through analysis of particle tracks. Particle track information can be obtained using the charge, timing, and topology information from the PMTs. Cherenkov light emission (Section 3.3) is directional and mostly

goes into a small solid angle area in a short period of time, meaning we can use the PMT information to determine the position, time, direction, and energy of a particle. MiniBooNE uses the following seven parameters to describe a particle track: The event vertex is described in terms of the starting position, x_0, y_0, and z_0, and the initial time, t_0. The direction of the event is described in terms of the polar angle θ_0 and azimuthal angle ϕ_0, defined with respect to the neutrino beam. And finally, E_0 describes the kinetic energy. The vector $\tilde{\mathbf{x}}$ contains these seven parameters. Each PMT is assigned 3 parameters, the first being a boolean determining whether the tube was hit, and the others being the measured charge and time of the hit. This information is then used to express a likelihood for observed PMT measurements given the track. The predicted charge for a given particle type and track parameters $\tilde{\mathbf{x}}$ can be determined using photon and particle propagation. Likelihood functions are created relating the expected parameters (i.e. charge and timing parameters) to the particle energy.

3.6.3 Particle ID

Particle identification is achieved by using the maximum likelihoods from a fit to each possible particle. The ratios $R_{e/\mu} = log(L_e/L_\mu)$ and $R_{e/\pi^0} = log(L_e/L_{\pi^0})$ are defined to determine whether the electron model leads to a better fit than the muon or π^0 models. To determine electron/muon separation for the ν_μ and ν_e appearance analysis, events are subject to several criteria. First, there must only be one subevent, eliminating muon events that decay and produce a Michel electron. In order to reject cosmic backgrounds, the number of PMT hits in the veto region must be less than 6, the number of PMT hits in the main region must be above 200, and the average time of the PMT hits must be within the beam window. A comparison of electron-to-muon likelihood ratios for true electron and true muon events are shown in Figure 3-6. For separation between electrons and π^0 events, $R_{e/\pi}$ is shown in Figure 3-7. In addition, the invariant mass, $M_{\gamma\gamma}$ determined by the two-track fit to the two γs in the π^0 case can also be used to help in the separation, as the true gamma events will tend towards the invariant mass of the π^0.

3.6.4 Reconstructed *vs.* True Neutrino Energies

The energy reconstructed from the event is not identical to the true energy of the neutrino. This is due to physics effects, such as energy losses in the nuclear environment and production of invisible particles, like neutrons, as well as detector effects like the resolution of the PMTs. However, the oscillation signal depends on the true neutrino energy. Thus, a simulation is used to map the possible true energies to the reconstructed energy of the event.

For a particular point in parameter space, previously generated ν_μ MC events are oscillated according to the oscillation probability calculated from the corresponding values of Δm^2 and $\sin^2 2\theta$. This generates the prediction to be used in the analysis for that particular mass and mixing model (Section 4.2). The MC takes into account the predicted ν_μ and $\bar{\nu}_\mu$ flux and measurements of ν_e and $\bar{\nu}_e$ cross-sections and selection

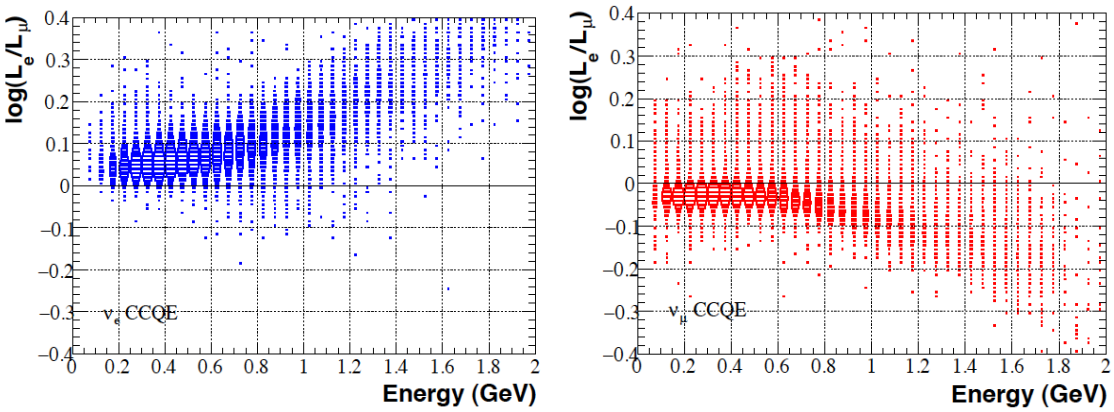

Figure 3-6: The distributions of $R_{e/\mu}$ for ν_e (left) and ν_μ (right) events as a function of electron-hypothesis reconstructed energy. Figure from Reference [77].

.

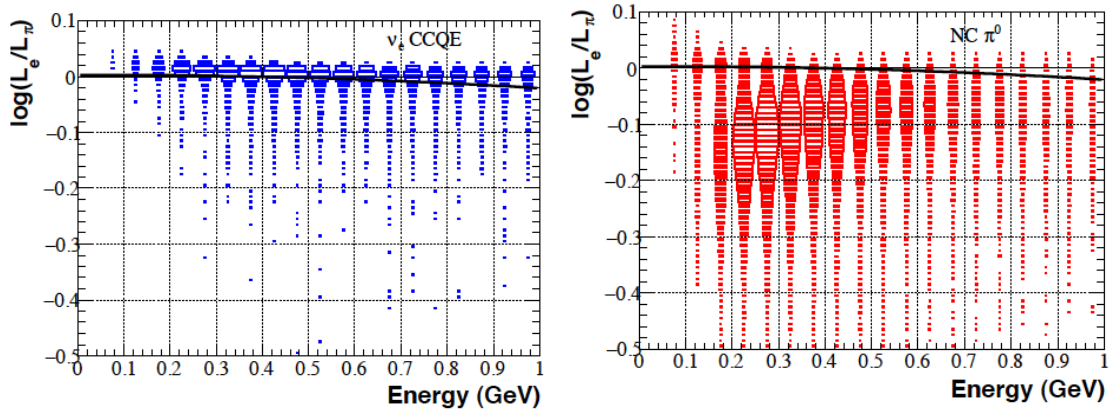

Figure 3-7: The distributions of $R_{e/\pi}$ for ν_e (left) and ν_π (right) events as a function of electron-hypothesis reconstructed energy. Figure from Reference [77].

.

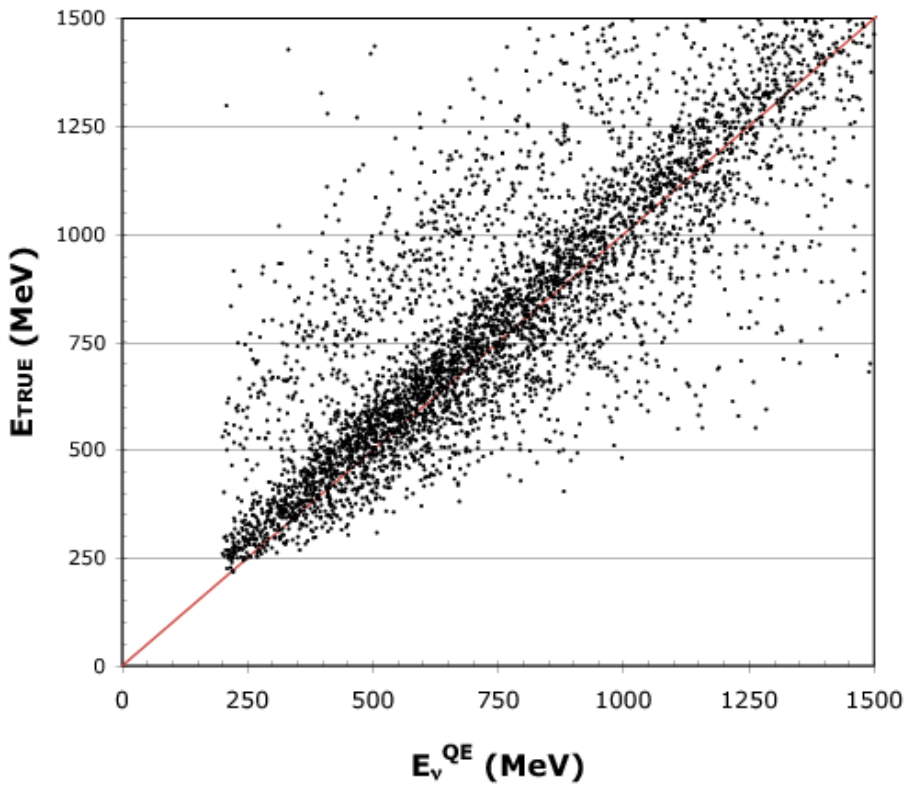

Figure 3-8: The relationship between the true neutrino energy E_{true} and the reconstructed neutrino energy, E_ν^{QE} in neutrino mode. From Reference [78].

efficiencies. This sample of MC events contains the reconstructed energy, the true neutrino energy, and the precise distance travelled for each individual event.

It is important to note that the histograms displaying MiniBooNE data over backgrounds displayed throughout the following chapter are shown as a function of reconstructed neutrino energy, E_ν^{QE}, rather than the true neutrino energy, E_{true}. The relationship between E_{true} and E_ν^{QE} can be seen in Figure 3-8 for the simulated, "fully oscillated" sample for neutrino-mode running.

3.7 Backgrounds to The Appearance Signal

3.7.1 NC π^0 Background

The production of π^0s is a potential source of ν_μ-induced background. Mis-IDs of these events are the primary background source at low energies for the $\nu_\mu \to \nu_e$ oscillation search, as can be seen in Figure 3-9. This is due to the subsequent $\pi^0 \to \gamma\gamma$, which occurs with a mean lifetime of 8×10^{-17} s. Each γ produces an electromagnetic shower in the detector, identical to the shower produced by an electron. There are circumstances where only one γ will be visible from a π^0 decay. If the π^0 is produced near the edge of the fiducial volume, one of the photons may exit the detector. Simi-

larly, if, due to a relativistic boost, one of the two photons is at too low of an energy, it may not be observed. A photon may also be lost in a photonuclear reaction. In the occasional very forward-going event, the two rings overlap and may be indistinguishable from a single ring. The rates of events with all of these types of kinematic profiles are constrained by the direct measurement of fully reconstructed π^0 rates in MiniBooNE [79].

π^0 events can arise from either resonant or coherent production. Resonant NC π^0 production is the dominant mechanism, and occurs when a ν_μ interacts with a nucleon producing a baryonic resonance particle. The resonance particle subsequently decays into a π^0 plus a nucleon:

$$\begin{aligned} \nu_\mu + N \rightarrow \nu_\mu + \Delta \\ \Delta \rightarrow \pi^0 + N \end{aligned} \tag{3.5}$$

Coherent NC π^0 production occurs when a neutrino scatters from the entire nucleus. During this process, the neutrino transfers a negligible amount of energy to the nucleus, and produces a forward-going π^0:

$$\nu_\mu + A \rightarrow \nu_\mu + A + \pi^0. \tag{3.6}$$

MiniBooNE measures the rate in-situ to compare with simulation, as there is limited information at these low energies from previous experiments. The π^0 measurements at MiniBooNE are described in detail in References [79] and [80]. This measurement is made using a sample of unambiguous π^0 events, demonstrating two electron-like rings in the detector. This data then provides a correction to π^0 mis-ID events, as shown in Figure 3-10.

3.7.2 Radiative Δ Decay

Another γ-induced background in MiniBooNE is from the decay of Δ particles. These Δs arise through the same mechanism as coherent π^0 production, but instead decay electromagnetically:

$$\begin{aligned} \nu_\mu + N \rightarrow \nu_\mu + \Delta \\ \Delta \rightarrow N + \gamma \end{aligned} \tag{3.7}$$

with a branching ratio of 0.55 - 0.65% [2]. When $N = 1$, the γ is indistinguishable from an electron event. The rate of Δ production is constrained by the measured rate of π^0 events, with additional uncertainty coming from errors in the branching fraction as well as final state interactions. Correlations between the two γ-induced backgrounds are accounted for through the covariance matrix described in Section 4.1.

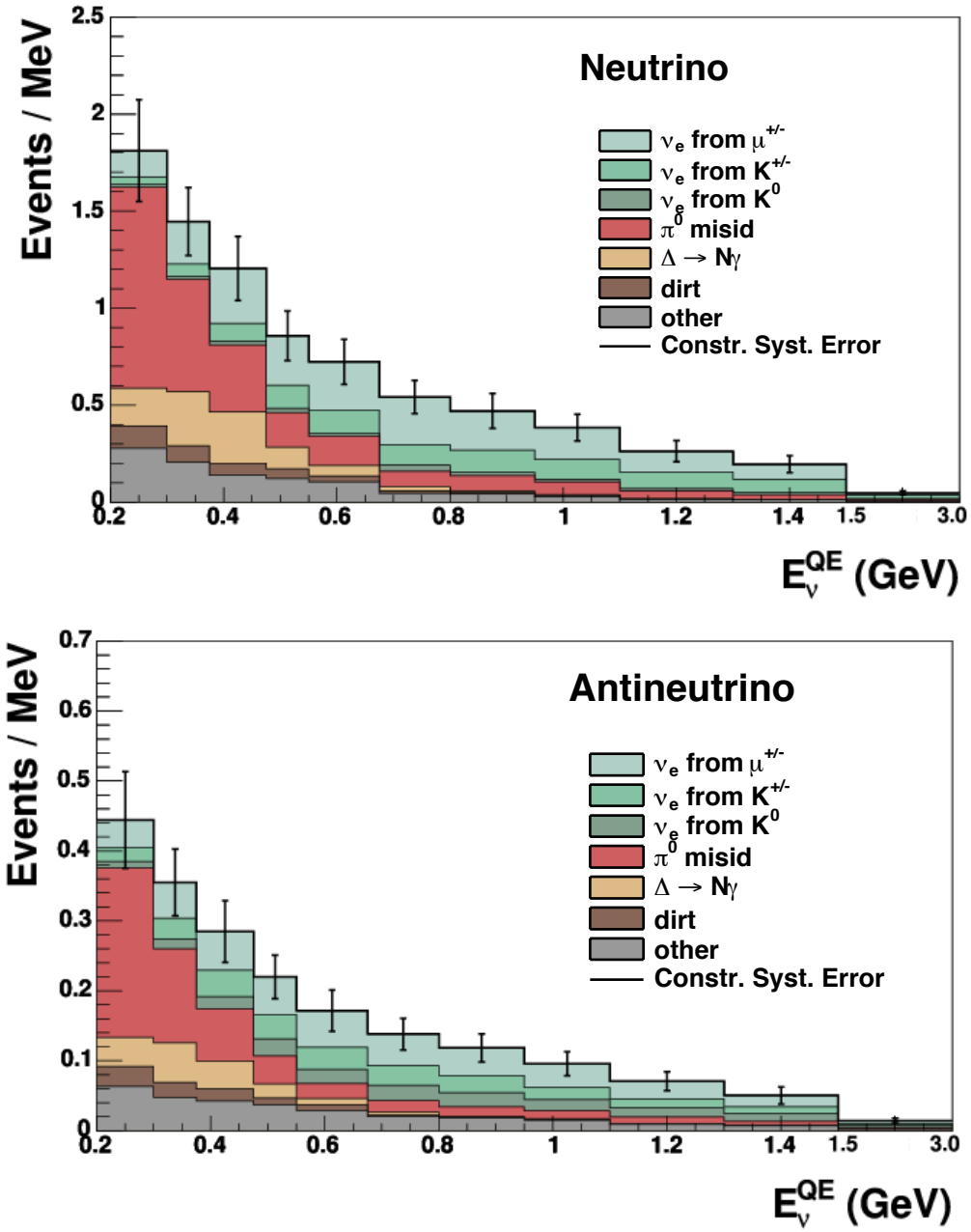

Figure 3-9: Neutrino-mode (top) and antineutrino-mode (bottom) backgrounds in an energy range of reconstructed energy between 200 MeV $< E_\nu^{QE} <$ 3000 MeV.

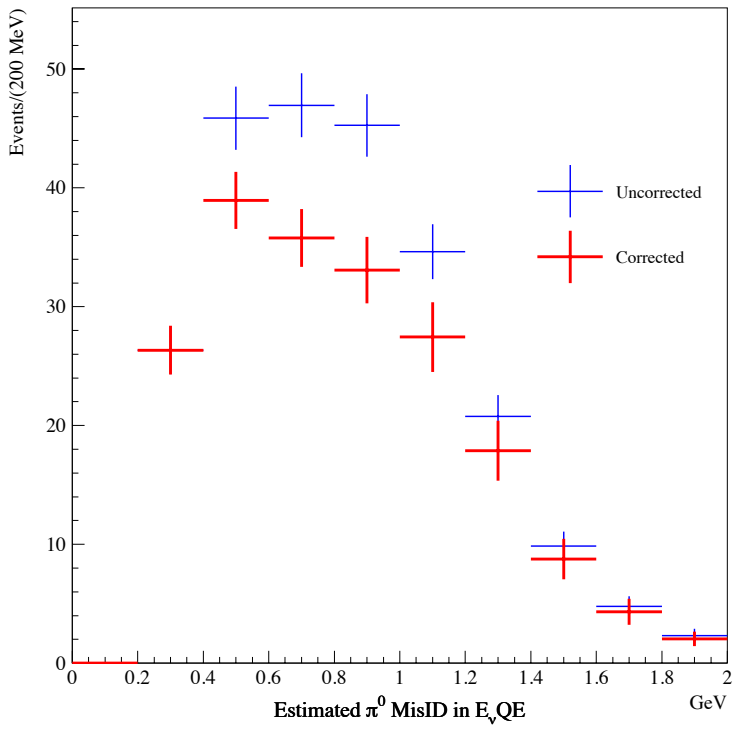

Figure 3-10: The predicted number of events from π^0 misIDs for the neutrino-mode data set for 5.68 $\times 10^{20}$ POT from the Monte Carlo. The red points correspond to the prediction from the raw Monte Carlo and the blue points include the corrections from the in-situ measurement. From Reference [81].

3.7.3 Intrinsic ν_e Background

ν_e events stemming from the decay chain that produces the flux of muon antineutrinos are the largest background, particularly above 475 MeV, as seen in Figure 3-9. Most of these electron neutrinos come from the muons from π^+ decays:

$$\begin{aligned} \pi^+ \rightarrow & \mu^+ + \nu_\mu \\ & \mu^+ \rightarrow e^+ + \nu_e + \bar{\nu}_\mu \end{aligned} \tag{3.8}$$

as described in Section 3.1. There is also a contribution from positive kaons, which decay by the same mode as the pions in Equation 3.8 and also by

$$K^+ \rightarrow \nu_e + \pi^0 + e^+. \tag{3.9}$$

And finally, the smallest electron component in Figure 3-9 is from:

$$K^0 \rightarrow \nu_e + \pi^- + e^+. \tag{3.10}$$

For antineutrino-mode, All of the above applies after interchanging particles with antiparticles.

Most of the muons live for long enough to be absorbed by the absorber, so the magnitude of the flux of ν_es is only 0.4% that of the ν_μ. However, this still contributes to the background (Figure 3-9).

3.7.4 Wrong-sign ν_e Background

As can be seen in Figure 3-1, there is an antineutrino component to the neutrino beam and a neutrino component to the antineutrino beam. These arise from the decays of forward-going pions of the wrong sign, which can escape deflection from the magnetic field of the focusing horn (Figure 3-11). This background is of greater significance in antineutrino mode, since π^+s, which decay into neutrinos, are preferentially produced by about a factor of two. The neutrino cross-section is also a factor of 3 higher than the anti-neutrino cross-section in mineral oil. The analysis of the neutrino component to the antineutrino beam is detailed in Reference [82].

MiniBooNE uses pion production data from proton-beryllium collisions from the HARP experiment [61], which covers most of the phase space relevant to MiniBooNE (indicated in Figure 3-11), but is lacking data for the most forward-going pions.

There are two analyses used to directly measure the neutrino component of the antineutrino beam. First, charged-current single π^+ (CC1π^+) data is compared to MC event rates. A clean sample $CC1\pi^+$ events are identified by detecting the μ^-,

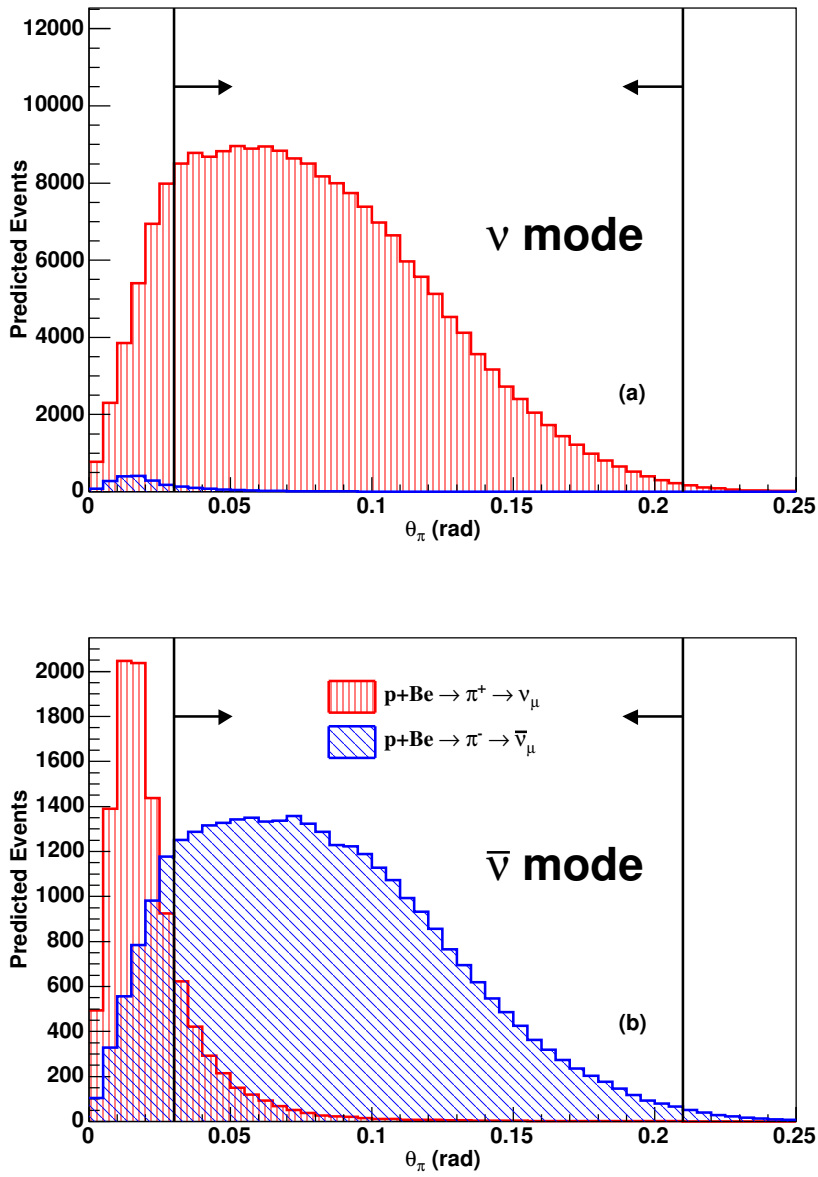

Figure 3-11: Angular distribution of pions relative to the proton beam for neutrino mode (a) and antineutrino mode (b). The area indicated by arrows represents the angles where HARP [61] data is available. Distributions represent 5.66 $\times 10^{20}$ POT. From Reference [82].

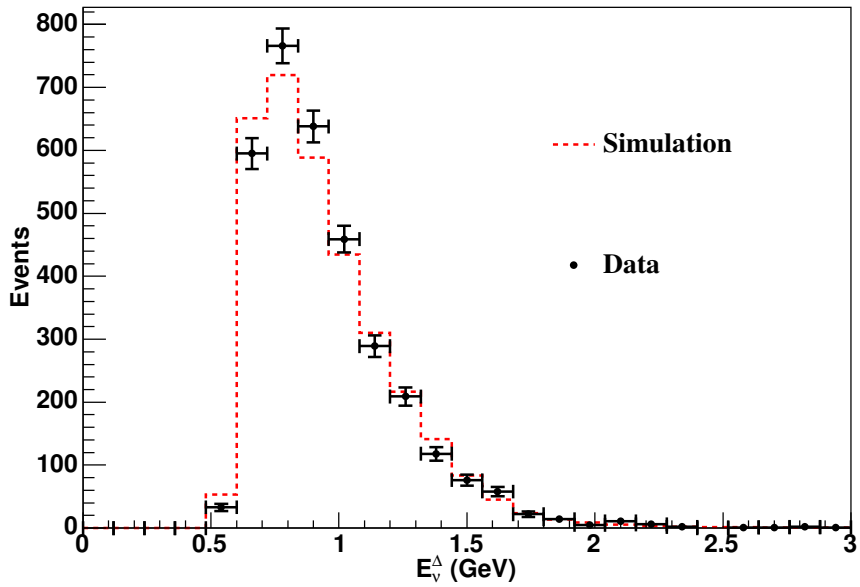

Figure 3-12: The $CC1\pi^+$ sample reconstructed energy spectrum comparing data (stat-only errors) to MC. The MC is normalized to data. From Reference [82].

e^-, and e^+ from the decay chain:

$$\begin{aligned} \nu_\mu + N \rightarrow \mu^- + N + \pi^+ \\ \pi^+ \rightarrow \mu^+ + \nu_\mu \\ \mu^- \rightarrow e^- + \bar{\nu}_e + \bar{\nu}_\mu \\ \mu^+ \rightarrow e^+ + \nu_e + \bar{\nu}_\mu, \end{aligned} \tag{3.11}$$

where N is either a proton or a neutron. The requirement of the detection of all three of these sub-events eliminates most of the $\bar{\nu}_\mu$-induced $CC1\pi^-$ events since the majority of the π^- are captured by carbon and therefore do not produce a decay electron. An additional requirement for this analysis is that the first subevent happens within 3 μs of the proton spill. Events that are near the edge of the detector are rejected to ensure the containment of the entire event for proper reconstruction. Low energy muons are also rejected, to make sure that the first subevent is not a Michel electron, but the second and third subevents must have the appropriate number of hits to be consistent with a Michel electron. It is also required that the closest Michel electron vertex is spatially consistent with the end of the muon track. These cuts lead to an $\sim 80\%$ pure ν_μ sample. The results of this study are shown in Figure 3-12.

The second analysis used to measure the neutrino component to the antineutrino beam compares the different angular distributions from CCQE interactions with MC. CCQE events are identified by two sub-events; a μ^+ from the initial interaction and the positron from the μ^+ decay:

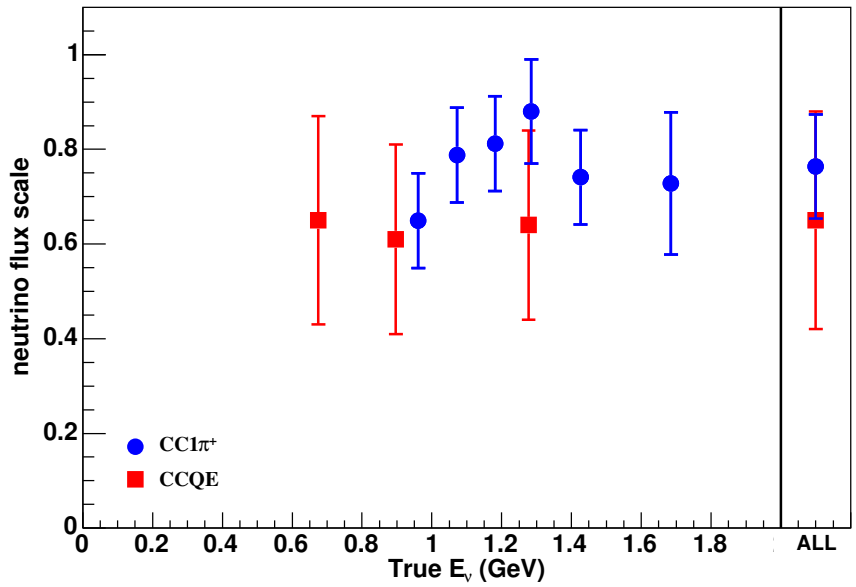

Figure 3-13: The constraint of the neutrino component to the antineutrino mode beam from the two analysis described in the text. From Reference [82].

$$\bar{\nu}_\mu + p \rightarrow \mu^+ + n \qquad (3.12)$$
$$\mu^+ \rightarrow e^+ + \nu_e + \bar{\nu}_\mu.$$

The sample is required to contain two subevents, with the first occurring between 4000 and 7000 ns of the event time window and having a vertex located less than 500 cm from the center of the tank. The first subevent must have greater than 200 tank hits and the second must have less than 200 hits. The veto hits cannot exceed 6 for either subevent. There is also a spatial requirement that the distance between the end of the first subevent and the beginning of the second cannot exceed 100 cm. These cuts and efficiencies are described in more detail in References [73] and [82].

The $\bar{\nu}_\mu$ component of the primary muon angular distribution is suppressed in the backward-scattering region due to an axial-vector interference term that differs between neutrino and antineutrino CCQE cross sections. This can be used to illuminate the difference between the cross sections.

These two analysis complement each other, as they cover slightly different energy regions. The results are summarized in Figure 3-13.

3.7.5 Dirt Backgrounds

We define dirt events as events with a vertex outside of the fiducial volume of the detector, either in the veto region or outside of the detector itself. The dirt background

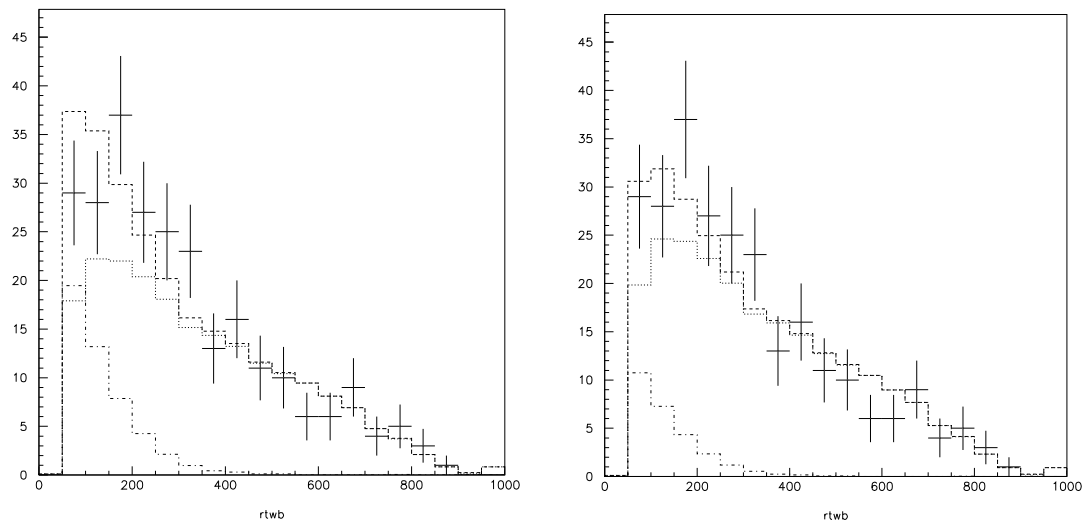

Figure 3-14: The R_{btw} distribution before (left) and after (right) the fit was done. Dashed line: total MC prediction, dotted line: in-tank event contribution, dot-dashed line: dirt event contribution. From Reference [83].

for the appearance analysis consists mainly of single photons from π^0 events that occurred outside of the fiducial volume, but where one of the photons makes it to the fiducial region before leaving any sign in the detector.

These events usually occur close to the detector boundaries, have inward-pointing tracks, and have lower visible energies. They are studied in MiniBooNE by making a sample using cuts on R_{btw} – the back-to-wall radius (Or rather, the distance from the edge of the fiducial volume), $(UR)/R$ – the scalar product of the event track direction and direction from the tank center to the vertex, and E_{vis} – the visible energy. The "Dirt-enriched" sample that arises from these cuts enables a comparison to be done with Monte Carlo, allowing for a correction to the number of total dirt events predicted by the MC. The results can be seen in Figures 3-14 and 3-15. Normalized to the original prediction, this correction factor comes out to be $70 \pm 10\%$ for neutrino-mode and $81 \pm 24\%$ for antineutrino mode.

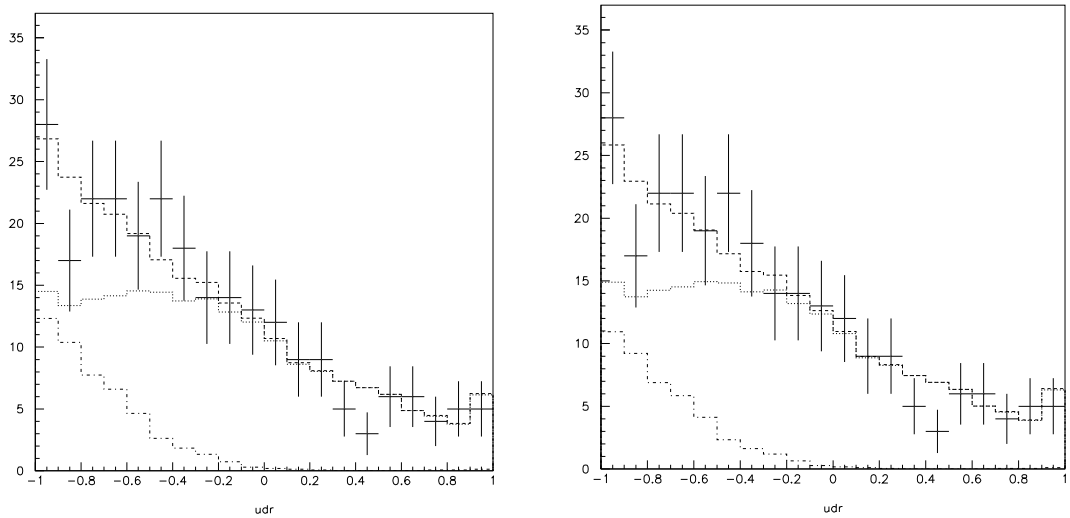

Figure 3-15: The UR/R distribution before (left) and after (right) the fit was done. Dashed line: total MC prediction, dotted line: in-tank event contribution, dot-dashed line: dirt event contribution. From Reference [83].

Chapter 4

The MiniBooNE Electron-Flavor Appearance Analyses

In the previous chapter, the process of turning the raw data and low-level Monte Carlo into reconstructed events was described. In this chapter, we describe how these events are used in the electron-flavor appearance analysis. The two step process involves first determining the systematic errors and then implementing an oscillation analysis. The results of the neutrino mode oscillation analysis, performed before I joined the experiment, are reported. This is followed by the results of the antineutrino oscillation analysis, in which I participated.

4.1 Systematic Uncertainties in the Oscillation Analysis

There are a total of 13 sources of systematic errors accounted for in the oscillation analysis, and they are assumed to be uncorrelated with each other. The energy-bin correlations for each systematic are accounted for in this analysis using a covariance matrix. The covariance matrix is constructed for each of these uncertainties and they are summed, along with the statistical uncertainty on the data, to produce a full covariance matrix. The contributions from each of these systematic errors are summarized in Tables 4.1 and 4.2 for neutrino mode and antineutrino mode respectively.

4.1.1 Covariance Matrix Construction

Each covariance matrix is constructed by varying 1000 Monte Carlo reconstructed-energy distributions for the ν_e CCQE background events, the ν_e CCQE predicted oscillation events, and the ν_μ CCQE sample. The predicted parameters for each uncertainty are varied within their own errors. The full covariance matrix can be derived from the variance of these distributions. This process is called a unisim or multisim method, where the unisim method fluctuates parameters independently, and

		ν_e signal		ν_e background		ν_μ CCQE	
Matrix	Section	200-475	475-1100	200-475	475-1100	0-700	700-1400
Beam	4.1.2	3.1	3.65	1.26	2.6	3.54	4.39
CC$\pi^{\pm}$	4.1.2	0	0	0	0	1.72	1.88
Dirt	4.1.2	0	0	0.91	0.5	0	0
Hadronic	4.1.2	0.23	0.09	0.8	0.56	0.05	0.02
K^0 Production	4.1.2	0	0.02	0.5	1.48	0.02	0.02
K^- Production	4.1.2	0	0	0.03	0	0.01	0.01
K^+ Production	4.1.2	0.06	0.07	0.41	1.74	0.09	0.11
Electronics	4.1.2	7.42	4.03	3.97	3.16	1.9	2.43
π^0 Yield	4.1.2	0.03	0.01	0.03	1.46	0	0
π^- Production	4.1.2	0.05	0.13	0.15	0.06	0.1	0.17
π^+ Production	4.1.2	14.22	4.74	5.35	3.76	5.95	4.04
Other xsec	4.1.2	17.89	15.87	16.22	5.78	14.53	15.89
Optical Model	4.1.2	19.61	3.49	8.26	2.17	4.93	2.64
Total		31.17	17.78	19.47	8.77	17.03	17.45

Table 4.1: Systematic errors (%) for the ν_e signal (oscillated from MC events for each mass and mixing model), ν_e background, and ν_μ CCQE samples before the ν_μ constraint is applied. The optical model and total uncertainties only include the systematic uncertainties.

the multisim method accounts for correlations between different parameters, fluctuating parameters according to their correlations rather than independently.

4.1.2 Sources and Determination of Errors

The systematic uncertainties can be broken up into three categories: neutrino flux uncertainties, neutrino cross section uncertainties, and detector modeling uncertainties.

Neutrino Flux Uncertainties

Neutrino flux uncertainties account for 6 out of the 13 systematic uncertainties. Five of these are uncertainties on the normalization and momentum distributions of each of the mesons produced from proton interactions with the target (π^+, π^-, K^+, K^-, and K^0). The sixth includes uncertainties on the beam including the horn current,

		$\bar{\nu}_e$ signal		$\bar{\nu}_e$ background		$\bar{\nu}_\mu$ CCQE	
Matrix	Section	200-475	475-1100	200-475	475-1100	0-700	700-1400
Beam	4.1.2	2.14	2.77	1.63	2.92	2.96	3.4
CC$\pi^\pm$	4.1.2	0	0	0	0	5	0.65
Dirt	4.1.2	0	0	1	0.47	0	0
Hadronic	4.1.2	0.2	0.18	0.41	0.21	0.04	0.03
K^0 Production	4.1.2	0.02	0.02	1.92	5.25	0.05	0.05
K^- Production	4.1.2	0.02	0.08	0.45	1.22	0.06	0.13
K^+ Production	4.1.2	0	0	0.68	1.39	0.14	0.16
Electronics	4.1.2	4.8	1.95	4.2	4.33	2.13	2.42
π^0 yield	4.1.2	0.03	0.04	1.47	1.4	0	0
π^- Production	4.1.2	14.78	4.42	3.09	2.46	6.03	3.62
π^+ Production	4.1.2	0.05	0.05	0.42	0.83	1.83	3.31
Other xsec	4.1.2	16.63	17.39	6.41	12.71	14.72	15.99
Optical model	4.1.2	8.94	2.79	8.21	3.06	3.1	2.13
Total		24.55	18.47	12.09	15.43	17.45	17.39

Table 4.2: Systematic errors (%) for the $\bar{\nu}_e$ signal (oscillated from MC events for each mass and mixing model), $\bar{\nu}_e$ background and $\bar{\nu}_\mu$ CCQE samples before the $\bar{\nu}_\mu$ constraint is applied. The optical model and total uncertainties only include the systematic uncertainties.

nucleon interactions within the target and horn, and pion cross sections throughout the beamline.

The majority of ν_μ events are from π^+ decay in neutrino mode and both π^+ and π^- decay in antineutrino mode. At higher energies, K^+ production accounts for larger fractions of ν_μ events, dominating at energies above 2 GeV. The number of neutrinos produced from each type of decay is summarized in Figures 4-1 and 4-2.

π^- and K^0 production errors are calculated from the Sanford-Wang parametrization [63] to world π^- and K^0 production data respectively, which is used to describe the differential production cross sections of the mesons as a function of beam momenta. Parameters from this model are determined in a fit to production data, as described in Reference [64]. The π^+ errors can also be determined in this way, but a more accurate method involves propagating the error matrix from HARP [61] using a spline interpolation of the HARP data [84].

The K^+ errors were originally formed by propagating the error matrix from the

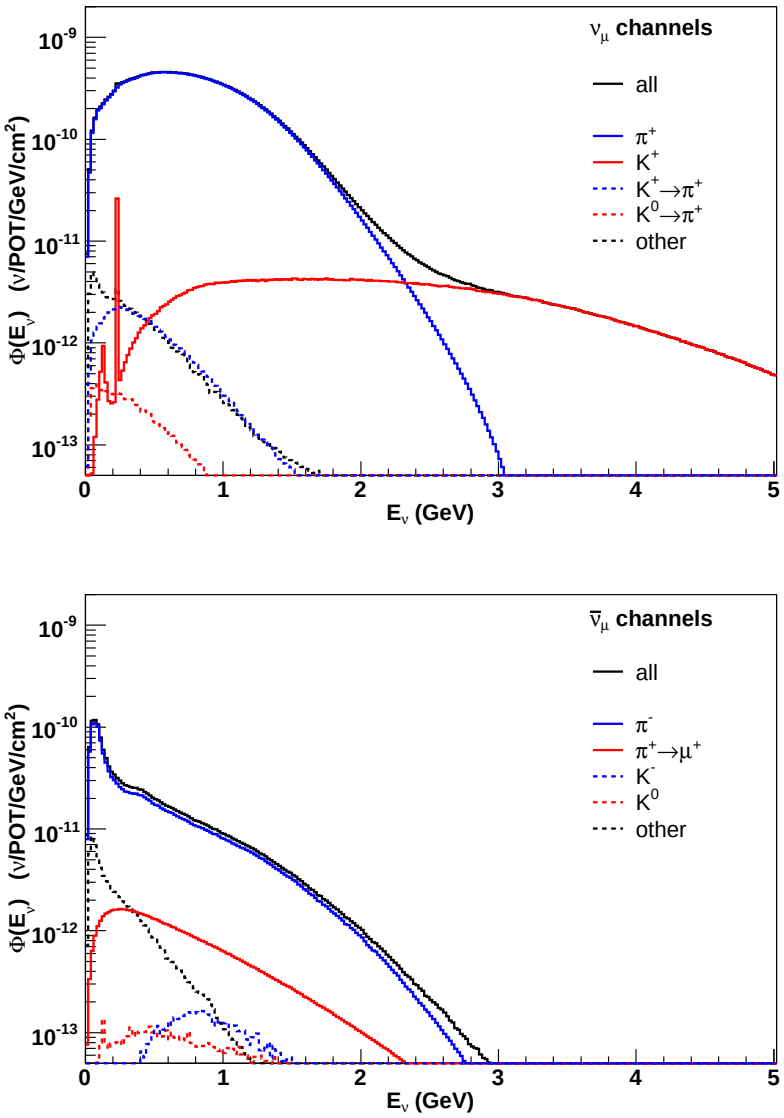

Figure 4-1: The predicted ν_μ and $\bar{\nu}_\mu$ flux in neutrino mode divided by parent meson. The primary channels colored in red and blue are from nucleon-induced meson production, while the dashed black histogram labeled "other" includes primarily contributions from secondary mesons in chains stemming from the initial meson-nucleus interaction from Reference [64].

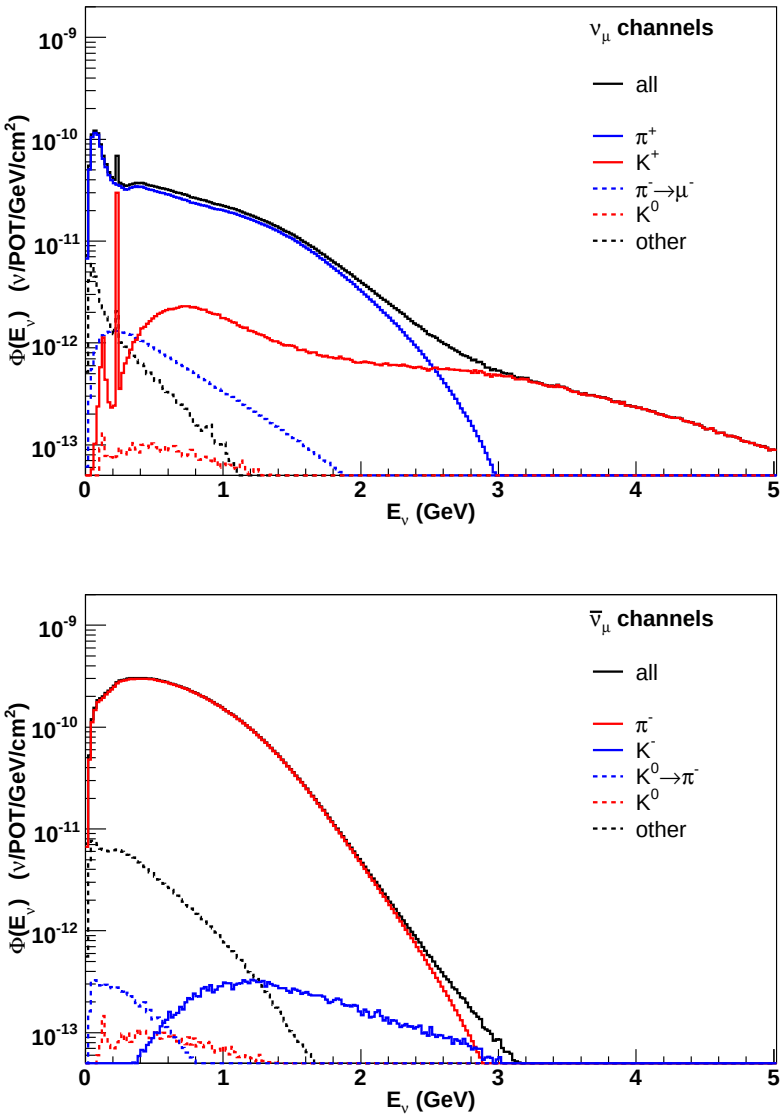

Figure 4-2: The predicted ν_μ and $\bar{\nu}_\mu$ flux in antineutrino mode divided by parent meson. The primary channels colored in red and blue are from nucleon-induced meson production, while the dashed black histogram labeled "other" includes primarily contributions from secondary mesons in chains stemming from the initial meson-nucleus interaction from Reference [64].

Feynman scaling fit [85]. The Feynman scaling hypothesis was used to determine the expected production at the BNB primary momentum of 8.89 GeV/c, which had not previously been explicitly measured, using production measurements at different energies from world K^+ production data [64]. The K^+ rate prediction has been constrained and verified by the SciBooNE experiment [86]. For the particle production uncertainties, the measured cross sections are varied according to the covariance matrix describing the uncertainties in each particular measurement. The neutrino flux is recalculated for each set of randomly generated parameters. The errors in the neutrino flux uncertainty can then be derived from the variance of these distributions.

The beam uncertainty matrix includes several considerations. First, the number of protons delivered to the target is measured by two toroids upstream of the target and errors are an overall normalization uncertainty. The uncertainties due to hadronic interactions in the target and horn come from agreement between available hadron-nucleus measurements and the Glauber model calculations. These uncertainties are included by varying the total hadronic cross section, the total inelastic cross section, and the quasi-elastic cross sections separately. Relations between the cross sections for nucleons on beryllium and aluminum (the materials of the target and horn respectively) are accounted for[64]. Magnetic field modeling of the horn also contributes in the uncertainty of the horn current itself and uncertainty in modeling of the current within the inner cylinder which is complicated by the skin effect. Beamline geometry uncertainty is not included due to variance studies yielding no significant changes.

Neutrino Cross Section Uncertainties

Five additional uncertainties come from neutrino cross sections. The rates of π^0s, dirt events, $CC\pi^\pm$, hadronic final state interactions, and "other cross section events" are included.

The π^0 and dirt events are discussed in Section 3.7, and these uncertainties represent the errors on those measurements. "$CC\pi^\pm$" is the uncertainty on the $CC\pi^\pm$ event rate. "Hadronic uncertainties" include processes such as pion absorption and charge exchange. "Other" includes other neutrino cross-section parameters such as uncertainties on Fermi momentum, binding energy, and other cross section parameters.

Detector Modeling

The remaining two uncertainties come from uncertainties in the optical model and detector electronics. The optical model considers the physical and optical properties of the oil such as density, thermal expansion, chemical decomposition, scintillation and fluorescence yields, Rayleigh scattering, etc. It also accounts for PMT properties such as quantum efficiency and angular efficiency, along with processes such as reflections in the tank. Correlations are accounted for using a multisim method as described in Section 4.1.1. Detector electronics uncertainties primarily consist of PMT charge and timing uncertainties and are accounted for by the unisim method.

4.1.3 ν_μ CCQE constraint

MiniBooNE is subject to a large error in overall neutrino flux due to its single-detector configuration. This is overcome by using the large (10^5 in neutrino mode and 10^4 in antineutrino mode) sample of ν_μ CCQE events to constrain the overall neutrino flux. This procedure allows for many of the flux and cross-section related uncertainties to effectively cancel out, significantly reducing systematic errors. This explicitly assumes lepton universality. The ν_μ sample not only provides information on how many ν_e appearance events are expected, but also constrains the ν_e backgrounds. In neutrino mode (signs and bars flip for antineutrino mode), most of the intrinsic ν_e come from the decay of the μ^+ associated with the primary ν_μ sample:

$$\begin{aligned} \pi^+ \rightarrow & \mu^+ + \nu_\mu \\ & \mu^+ \rightarrow e^+ + \nu_e + \bar{\nu}_\mu \end{aligned} \tag{4.1}$$

where the ν_μ on the first line is a ν_μ from the primary ν_μ sample and the ν_e on the second line is the aforementioned background, which is directly correlated with the measured ν_μ rate. Over 90% of ν_μs (and therefore ν_es from $\nu_\mu \rightarrow \nu_e$) come from this decay chain, as do about 1/3 of the ν_e background events. This is considerable overlap leading to a correlation. Other ν_e backgrounds are tied to the same pion decay chains, such as $\pi^+ \rightarrow e^+ + \nu_e$ and are therefore also correlated.

The ν_μ constraint also allows some cross section uncertainties to cancel out, as the ν_e signal events and some ν_e backgrounds share the CCQE cross-section with the ν_μ sample.

4.1.4 Statistical Uncertainties

The statistical uncertainties based on the CCQE ν_e background and ν_μ central value predictions are included by adding them to the diagonal of the total covariance matrix. The statistical uncertainty of the ν_e events from the signal prediction for the particular mass and mixing model being evaluated is also included. A statistical uncertainty on the MC calculations according to the number of generated events is also included.

4.1.5 Differences between neutrino and antineutrino mode systematics

For clarity, the above discussion follows the process of determining the systematic errors for neutrino mode running. The antineutrino analysis proceeded similarly. Differences in the values of the systematics mostly stem from the larger wrongsign component in antineutrino-mode. There is more contamination from positive mesons when attempting to focus negative mesons in antineutrino-mode compared with the contamination when focusing positive mesons in neutrino mode. This is due to the larger number of positive mesons produced by the p-Be interaction (Section 3.1). This leads to higher systematic errors for the antineutrino-mode π^+ (and to a lesser

Process	Neutrino Mode	Antineutrino Mode
ν_μ & $\bar{\nu}_\mu$ CCQE	37.1 ± 9.7	12.9 ± 4.3
NC π^0	252.3 ± 32.9	112.3 ± 11.5
NC $\Delta \to N\gamma$	86.8 ±12.1	34.7 ± 5.4
External Events	35.3 ± 5.5	15.3 ± 2.8
Other ν_μ & $\bar{\nu}_\mu$	45.1 ± 11.5	22.3 ± 3.5
ν_e & $\bar{\nu}_e$ from $\mu^\pm$ Decay	214.0 ± 50.4	91.4 ± 27.6
ν_e & $\bar{\nu}_e$ from $K^\pm$ Decay	96.7 ± 21.1	51.2 ± 11.0
ν_e & $\bar{\nu}_e$ from K_L^0 Decay	27.4 ± 10.3	51.4 ± 18.0
Other ν_e & $\bar{\nu}_e$	3.0 ± 1.6	6.7 ± 6.0
Total Background	797.7	398.2
0.26% $\bar{\nu}_\mu \to \bar{\nu}_e$	233.0	100.0

Table 4.3: The expected background events in the range of $200 < E_\nu^{QE} < 1250$ MeV for both the neutrino and antineutrino analyses. This also includes a prediction for a 0.26% oscillation probability (averaged over neutrino energy) as predicted by LSND. The errors represent the diagonal-element systematic errors. From Reference [35].

extent K^+) systematic compared with the neutrino-mode π^- systematic, especially at higher energies. This can be seen by comparing Tables 4.1 and 4.2.

Note that the CC K^- production and CC$\pi^\pm$ systematic error matrices were not included in the original neutrino-mode analysis, as their effects are minimal in neutrino mode. They have since been included (Section 4.3.1) for consistency with the antineutrino-mode analysis.

4.2 The Oscillation Analysis

MiniBooNE searches for $\nu_\mu \to \nu_e$ and $\bar{\nu}_\mu \to \bar{\nu}_e$ oscillations according to a 2-neutrino model. As described in Section 2.2, this fit can be interpreted as a 3+1 model, that is, a measurement of Δm^2_{41} within the framework of a sterile neutrino hypothesis where $\Delta m^2_{41} \gg \Delta m^2_{32}$ and Δm^2_{21}, outside of the range where oscillation effects from Δm^2_{32} and Δm^2_{21} are observable.

The expected background event rates are given in Table 4.3. A full error matrix is constructed as in Section 4.1, including errors and correlations among each background and systematic uncertainty as well as information about ν_μ and $\bar{\nu}_\mu$ predictions.

4.2.1 Constructing a χ^2

A χ^2 is constructed as follows:

$$\chi^2 = \sum_{i,j} [N_{data}(i) - N_{pred}(i)][M^{-1}(i,j)][N_{data}(j) - N_{pred}(j)] \tag{4.2}$$

where $N_{data}(i)$ is the measured number of ν_e events per energy bin, $N_{pred}(i)$ is the number of MC predicted events for a particular mass and mixing model per energy bin, and $[M^{-1}(i,j)]$ is element (i,j) of the inverse covariance matrix. i and j run from 1 to the number of ν_e energy bins plus the number of ν_μ energy bins. The prediction to be compared with data for a particular point in parameter space is generated by oscillating MC events according to the corresponding oscillation parameters, as described in Section 3.6.4.

The function which is minimized in this fit is the negative log likelihood, which is defined by:

$$-2log(L) = \chi^2 + log|M|, \tag{4.3}$$

where $|M|$ is the determinant of the covariance matrix.

Since this is a two-neutrino mixing model, the prediction is dependent on two parameters, Δm^2 and $\sin^2 2\theta$, according to a probability of $P = \sin^2 2\theta \sin^2(\Delta m^2 \frac{L}{E})$. The log likelihood is calculated for each point in Δm^2 *vs.* $\sin^2 2\theta$ parameter space along a grid to determine the best fit value and draw Confidence Level (CL) contours. The point with the lowest negative-log-likelihood is taken to be the best fit point and the corresponding χ^2 value is used to determine the goodness of fit.

MiniBooNE simultaneously fits the ν_μ CCQE event sample along with the ν_e events (Section 4.1.3) to increase sensitivity lost by the many flux and cross-section related systematic errors associated with this sample. This is accomplished by including the ν_μ bins in the fit and including uncertainties and correlations from both samples in the $N_{bins}^{\nu_e} + N_{bins}^{\nu_\mu}$ by $N_{bins}^{\nu_e} + N_{bins}^{\nu_\mu}$ error matrix.

The ν_e events are then fit as a ratio to the ν_μ events, allowing many systematic uncertainties to cancel out such as errors in the CCQE cross-section uncertainties. Errors in the predictions of meson decays will also cancel, since branching ratios among decays like $\pi^+ \to \mu^+ + \nu_\mu$ and $\pi^+ \to e^+ + \nu_e$ are well known, so errors in π^+ production predictions will affect both the ν_e and ν_μ samples equally.

The typical method of calculating the goodness of fit is to determine the χ^2 probability by assuming a Gaussian approximation. This method uses the best-fit χ^2 value and approximates the number of degrees of freedom determined as $N_{bins} - N_{parameters}$. In this case, the number of parameters is equal to two: Δm^2 and $\sin^2 2\theta$. We also subtract an additional parameter to account for a normalization correction applied to pion decay events. This correction adds a normalization factor to the ν_μ prediction based on comparing the ν_μ CCQE prediction with measurements.

While we do use this Gaussian approximation as a crosscheck, for the analysis we explicitly calculate the number of degrees of freedom corresponding to our best-fit value. We do this by generating a large number of fake data distributions according to our full scaled error matrix at the null and best-fit points. We then determine

what percentage of these "fake experiments" have a higher best-fit χ^2 value than that of our actual point. This percentage corresponds to the χ^2 probability of our point. From this probability, we can extrapolate the effective number of degrees of freedom. Note that this can lead to non-integer degrees of freedom when we report results.

4.2.2 Drawing Confidence Level Contours

Assuming Gaussian errors, Confidence Level (CL) contours can be drawn after a best-fit value and best-fit χ^2 (χ^2_{BF}) are found. A cut is made on the $\Delta\chi^2$ ($\chi^2 - \chi^2_{BF}$) value for 2 degrees of freedom corresponding to the CL interval we wish to draw. For example, the $\Delta\chi^2$ value for a 90% CL interval is 4.61, meaning points in the parameter space with a $\chi^2 < \chi^2_{BF} + 4.61$ will lie within the 90% CL contour and points that have a higher χ^2 will not.

To account for the errors not being exactly Gaussian, due to correlations between the fit parameters which vary across the parameter space, we instead employ the use of frequentist studies using fake data to determine CL intervals [87]. This method requires a large number of fake data distributions to be generated according to the full scaled error matrix for each point in Δm^2 *vs.* $\sin^2 2\theta$ parameter space. For each of the fake data distributions, an oscillation fit is performed and a best-fit χ^2 value is determined. From this, at each point, we can generate a distribution of $\Delta\chi^2$ ($\chi^2_{fake} - \chi^2_{BF}$) and determine what percentage of fake data experiments have a χ^2 that is less than the χ^2 from the real data at that point. Points with a percentage less than or equal to than the CL interval we are drawing will fall within the contour.

4.3 Results

4.3.1 First Results: $\nu_\mu \to \nu_e$ Appearance

The neutrino-mode run had 6.46×10^{20} protons on target (POT) and observed a total of 952 ν_e events within the energy range of 200 MeV $< E_\nu^{QE} <$ 1250 MeV. This compares with an expected background of $790.1 \pm 28.1(stat.) \pm 38.7(sys.)$, and corresponds to an excess of 162.0 ± 47.8 events above a no-oscillation hypothesis. Most of these events are in the region below 475 MeV. Above 475 MeV (the region that corresponds to the LSND event excess), the observed number of events are consistent with no excess. The excess in the region below 475 MeV is known as the "low-energy excess". The histogram showing the binned events above the predicted background is shown in Figure 4-3, and the excess (data minus background) is shown in Figure 4-4. Since the neutrino mode publications [88, 89], several changes have been made to the analysis and are as follows:

- **K^+ constraints from SciBooNE were incorporated**: The rate of K^+ production from proton-beryllium interactions has been measured by SciBooNE [86]. This has further constrained previous predictions which use the Feynman scaling hypothesis with production measurements at different energies from world K^+ production data. SciBooNE is a particularly important addition to

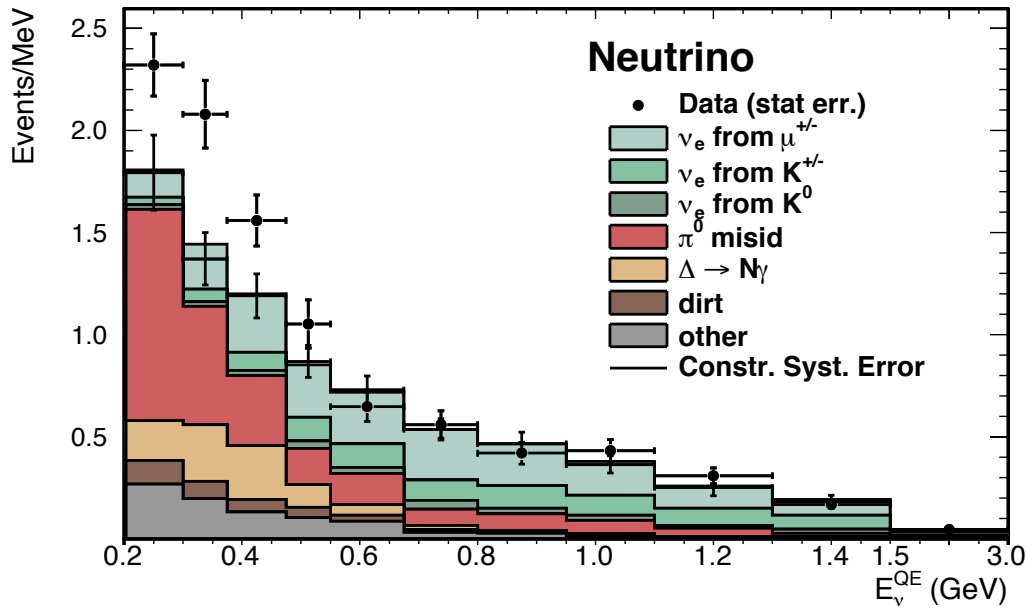

Figure 4-3: Neutrino mode data over predicted backgrounds for CCQE events as a function of reconstructed neutrino energy, E_ν^{QE}. The data points are plotted with statistical errors and backgrounds (from Figure 3-9) with systematic errors.

the global K^+ production constraints for MiniBooNE since it is sensitive to the same kaons that result in neutrinos at MiniBooNE. This addition results in a cross-section that is $\sim 3\%$ lower than the previous cross-section.

- **Log likelihood fit method**: The log likelihood method described in Section 4.2.1 was introduced. Previously it was the χ^2 rather than the negative-log-likelihood that was minimized.

- **Added the uncertainty on the CC$\pi^\pm$ event rate.** This is more relevant to the antineutrino mode analysis but was added to the neutrino mode analysis for consistency.

The χ^2/dof from this new neutrino-mode analysis is 13.2/6.8, corresponding to a χ^2 probability of 6.1%. This compares to a no-oscillation (null) hypothesis of χ^2/dof = 22.8/8.8 which yields a 0.5% probability. Although the best-fit parameters yield a higher probability than the null hypothesis, a two-neutrino fit is not a good description of the data. The shape of the low-energy excess does not appear to be consistent with a two-neutrino oscillation model. Adding a second sterile neutrino can lead to a shape that does (Section 4.4), as can learning that part or all of the low-energy excess is not due to ν_e events (Chapter 6).

Fitting only the region above 475 MeV yields a limit in Δm^2 *vs.* $\sin^2 2\theta$ space which excludes most of the LSND allowed region, as seen in Figure 4-5, while fitting the entire region yields closed contours (Figure 4-6).

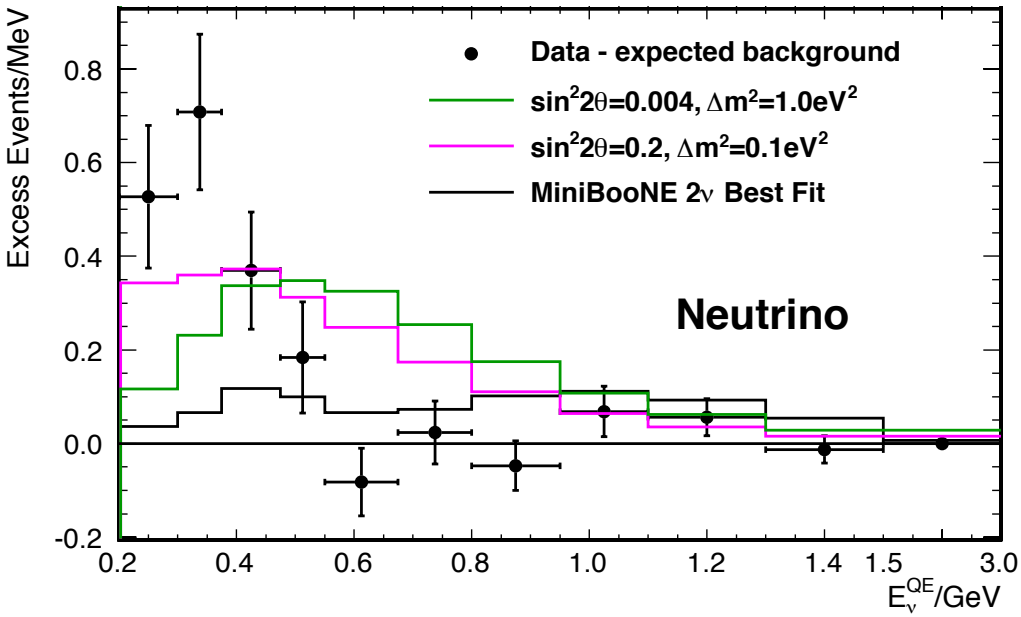

Figure 4-4: Neutrino mode data minus background. The data points should be consistent with zero for a no-oscillation hypothesis. The black line indicates the best fit point in parameter space and the pink and green lines indicate two points in the region of parameter space favored by LSND.

.

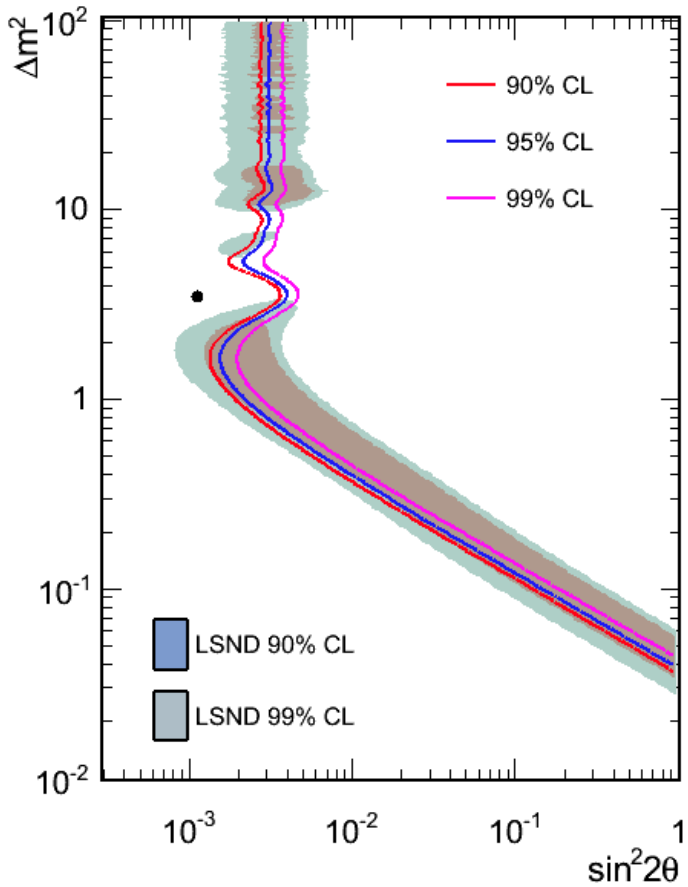

Figure 4-5: CL contours from a fit to MiniBooNE neutrino-mode data in an energy range between 475 MeV $< E_\nu^{QE} <$ 1250 MeV.

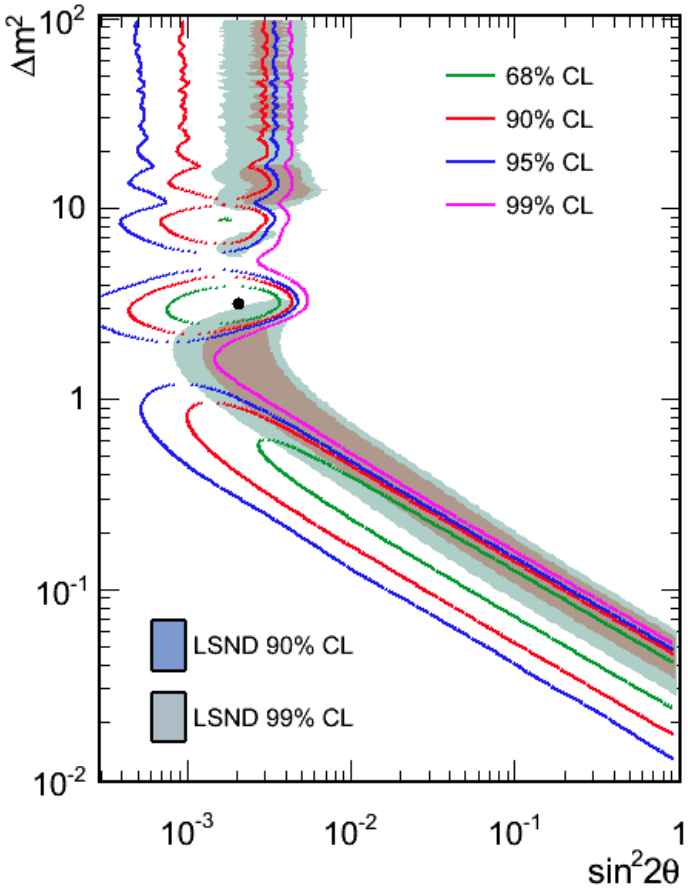

Figure 4-6: CL contours from a fit to MiniBooNE neutrino-mode data in an energy range between 200 MeV $< E_\nu^{QE} <$ 1250 MeV.

4.3.2 Discussion of Low-Energy Excess

The low energy excess is unlikely to be a statistical fluctuation, indicating that something must be unaccounted for or unexplained. It is unlikely to be the intrinsic ν_e in the beam since the ν_e background at this energy range is small. The π^0 background dominates at this regime, but is constrained by direct π^0 measurements in the MiniBooNE detector. The reducible π^0 rate with two visible gammas is well-measured and the irreducible case with only one visible gamma is constrained by the reducible rate. The rate would need to approximately double to account for the observed excess. Similarly, the rate of $\Delta \to N\gamma$ is tied to the NC π^0 rate. See Section 3.7 for more details. Many cross-checks have shown that the events that make up the low-energy excess do not have any discrepancies in parameters such as timing, position in the detector, direction, scattering angle, etc. compared to the Monte Carlo [88].

Though the focus of this thesis is on sterile neutrino oscillations, there are other theoretical models that introduce new physics to explain the low-energy excess unrelated to sterile neutrino oscillations [90, 91, 92]. Section 5.3 comments on the status of sterile neutrino models with and without the low energy excess being a result of sterile neutrino oscillations.

4.3.3 Antineutrino Mode: $\bar{\nu}_\mu \to \bar{\nu}_e$ Appearance

In antineutrino mode, there were a total of 11.27 $\times 10^{20}$ POT, which yielded a total of 478 oscillation candidate events in the detector. This compares to a background of 399.6 $\pm$ 20.0 $\pm$ 20.3 events, corresponding to an excess of 78.4 $\pm$ 28.5 events. Unlike in neutrino mode, the antineutrino mode data shows an excess above 475 MeV as well as at low energies (Figure 4-7), and the shape of this excess is consistent with the LSND expectation (Figure 4-9). The fit yields a χ^2/dof of 5.0/7.0 corresponding to a probability of 66% compared with a null χ^2/dof of 16.6/8.9 corresponding to a probability of 5.4%. The best-fit point sits at $\Delta m^2 = 0.043$, $\sin^2 2\theta = 0.88$, though the χ^2 surface is shallow in the diagonal region extending from the best-fit point to higher Δm^2 values and lower $\sin^2 2\theta$ values, as seen in Figure 4-9. The best-fit point itself is in a region excluded by many other experiments such as Karmen [93] (see Section 5.1), but the favored region extends into an allowed regime. Global fits including constraints from many other experiments are explored in Chapter 5.

Explanations for deviation from null in neutrino mode stemmed mostly from a similarity between the shape of the excess with gamma backgrounds, suggesting that there may be an unexpected background effect. In antineutrino mode, the excess at higher energies cannot be explained in this way. Assuming there are no sterile neutrinos, the questions that remain can be summarized as:

- "What is the low-energy excess?"
- "What is the higher-energy excess in antineutrino mode?"
- "Why does neutrino mode appear to be inconsistent with antineutrino mode?"

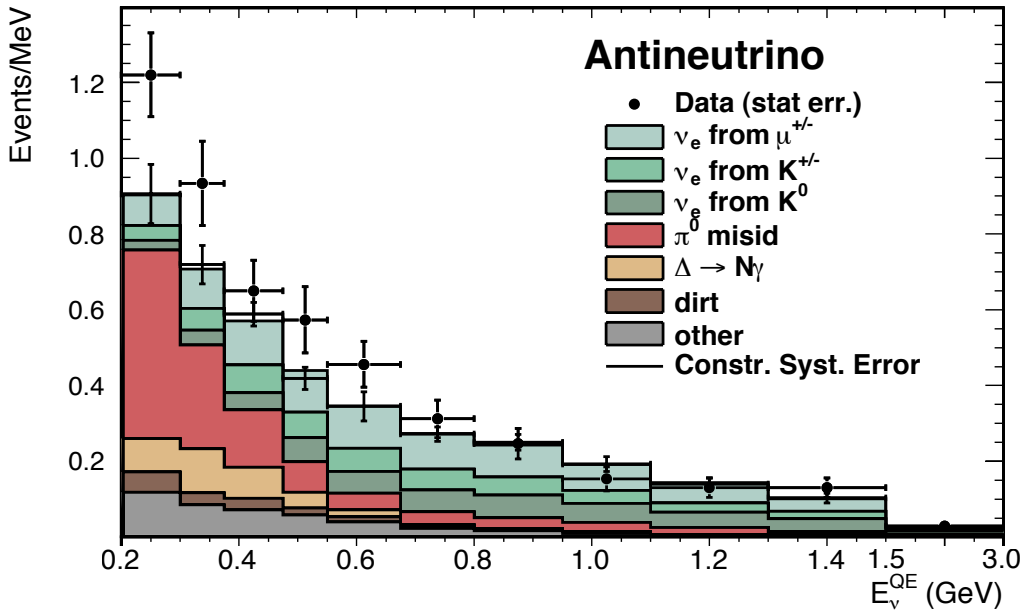

Figure 4-7: Antineutrino mode data over predicted backgrounds for CCQE events as a function of reconstructed neutrino energy, E_ν^{QE}. The data points are plotted with statistical errors and backgrounds with systematic errors.

The MicroBooNE Experiment (Chapter 6) is designed to shed light on the first question, but the second two will remain. The consistency between the neutrino and antineutrino mode datasets is explored further in the next section.

If one were to introduce sterile neutrinos, these three questions remain. Introducing sterile neutrinos leads to a better fit than a background-only fit, but tension still remains, particularly between neutrino mode and antineutrino mode. One way to relieve this tension is by introducing a second sterile neutrino (Section 2.2.2), which permits for CP-violation and therefore a mechanism for a difference between neutrino and antineutrino oscillations. This also allows for wave interference which can provide a good fit to the low-energy excess (Sections 4.4). However, the parameter space in which this happens is disfavored by other experiments, as will be explored further in Section 5.3. Though a combination of additional sterile states and some of the low-energy excess being from unexplained background processes leads to good agreement.

4.3.4 Combined Fit

The fits in published MiniBooNE papers assume a two-neutrino fit, which is interpreted as a $3+1$ model as explained in Section 2.2. If this was a good approximation, neutrinos and antineutrinos would have to oscillate with the same parameters, since a two-neutrino model does not accommodate CP-violating parameters. This means that they can be considered together within a $3+1$ model.

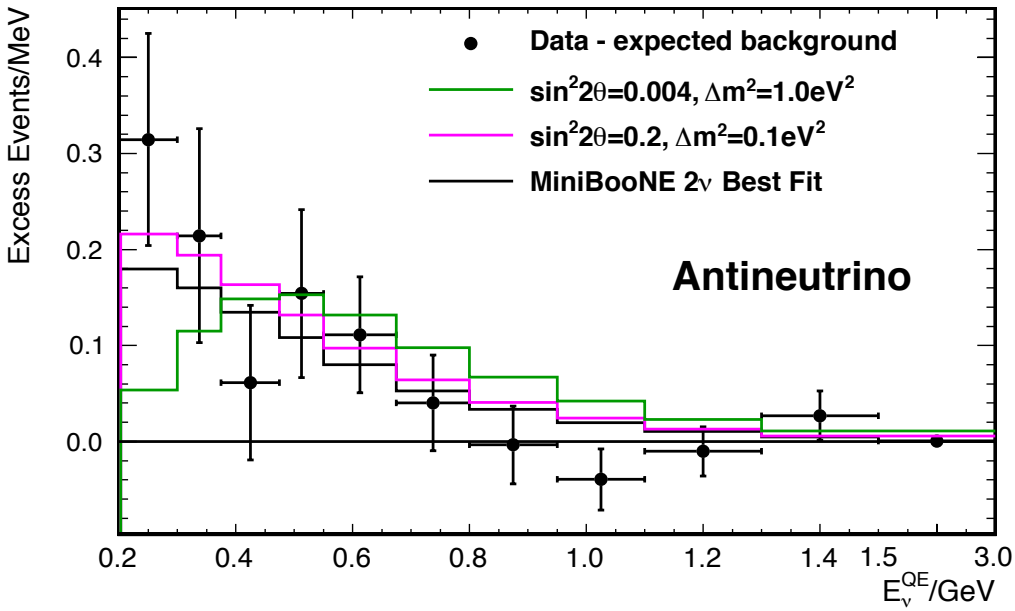

Figure 4-8: Antineutrino mode data minus background. The data points should be consistent with zero for a no-oscillation hypothesis. The black line indicates the best-fit point in parameter space and the pink and green lines indicate two points in the region of parameter space favored by LSND.

The bins for neutrino and antineutrino mode are fit side-by-side, with their bins falling along the diagonal of the new error matrix (which has twice as many rows and twice as many columns as the original matrices). The original neutrino mode and antineutrino mode matrices fall in the top-left and bottom-right quadrants of the new matrix, while the off-diagonal quadrants represent correlations between the neutrino-mode and antineutrino-mode datasets.

The χ^2/dof from the resulting fit is 24.7/15.6, which corresponds to a probability of 6.7%. This compares to a null probability of 0.1%. The best-fit parameters are $\Delta m^2 = 0.037$ and $\sin^2 2\theta = 1.0$. The combined fit is sitting at a large $\sin^2 2\theta$ value, in a region excluded by many other experiments. Like the antineutrino-mode fit, the χ^2 surface is shallow along the diagonal region extending to lower $\sin^2 2\theta$ values and higher Δm^2 values, as seen in Figure 4-11. This means that similar probabilities are found in a region which is not yet excluded by other experiments. When comparing to neutrino-mode data, the fit results in a prediction that is too low at lower energies and too high at higher energies (Figure 4-8).

4.4 Fitting MiniBooNE Data to a $3+2$ Model

Adding a second ~ 1 eV^2 sterile neutrino state includes the addition of a CP-violating parameter, which allows for a difference between neutrino and antineutrino oscillation predictions. As shown in Section 2.2.2, The mixing parameters for an appearance

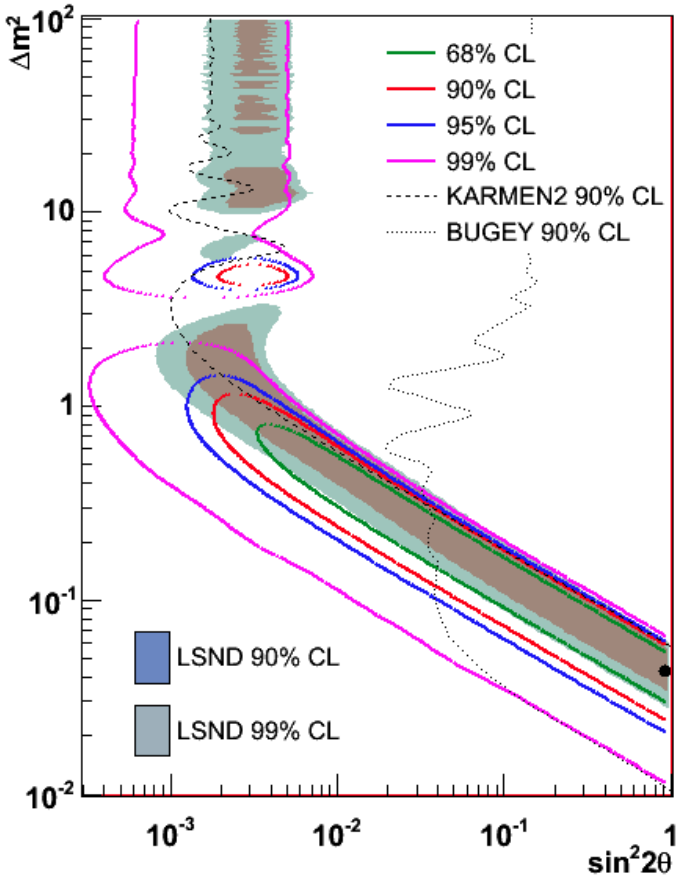

Figure 4-9: CL contours from a fit to MiniBooNE antineutrino-mode data in an energy range between 200 MeV < E_ν^{QE} <1250 MeV.

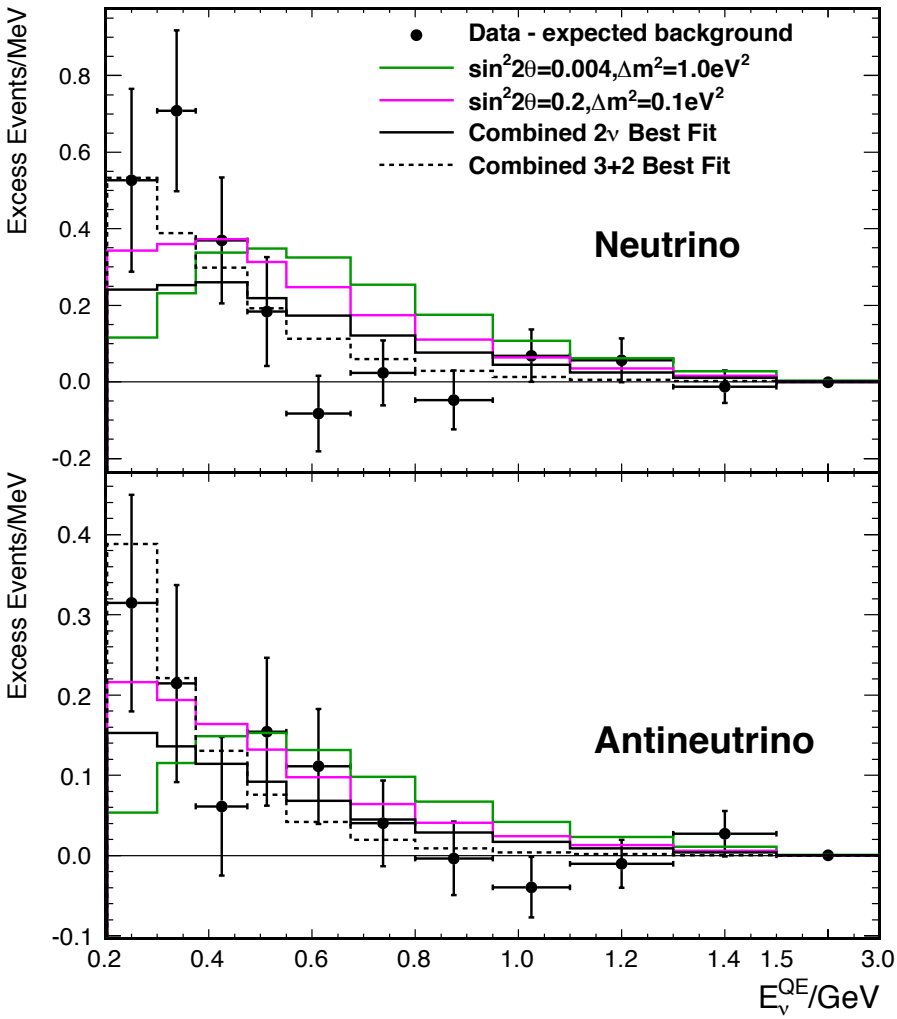

Figure 4-10: The data minus background histograms from Figures 4-4 and 4-8 here plotted with predictions representing the best fit values from a combined $3+1$ (two-neutrino) fit (solid black line) and a combined $3+2$ fit (dashed black line).

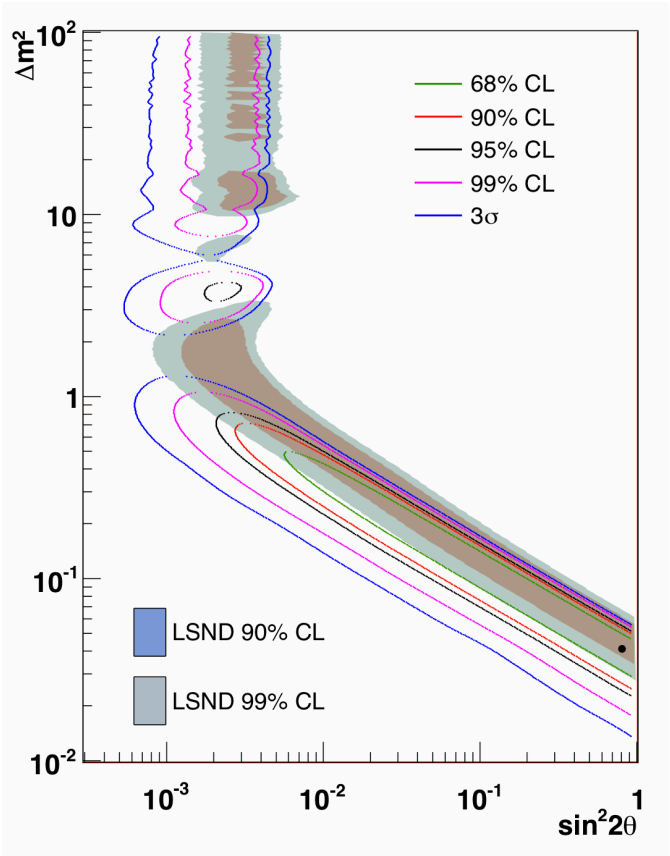

Figure 4-11: CL contours from a combined fit to MiniBooNE neutrino-mode data and antineutrino-mode data in an energy range between 200 MeV $< E_\nu^{QE} <$1250 MeV.

experiment only appear as products, in the form of $|U_{e4}|^2|U_{\mu4}|^2$ and $|U_{e5}|^2|U_{\mu5}|^2$, which along with Δm^2_{41} and Δm^2_{51}, are the parameters used in the fit.

It can be seen in Figure 4-10 that the interference between the two Δm^2 parameters allows the fit to rise up at lower energies to accommodate the low-energy excess, while also remaining consistent with the 475 MeV - 800 MeV region in both neutrino and antineutrino mode. The parameter space in which this happens is excluded by other experiments, as will be explored further in Section 5.3.

The best fit parameters from this fit are $\Delta m^2_{41} = 0.082$, $\Delta m^2_{51} = 0.476$, $|U_{e4}|^2|U_{\mu4}|^2 = 0.184$, $|U_{e5}|^2|U_{\mu5}|^2 = 0.00547$, and $\phi = 1.0005\pi$.

4.5 Accounting for Disappearance Within the Appearance Analysis

If there were a sterile neutrino with oscillation parameters Δm^2 and $\sin^2 2\theta$, where $\sin^2 2\theta = 4|U_{e4}|^2|U_{\mu4}|^2$, the ν_μ sample and the ν_e backgrounds would be subject to disappearance according to

$$4|U_{\mu4}|^2(1-|U_{\mu4}|^2)\sin^2(\Delta m^2_{41}\frac{L}{E}) \tag{4.4}$$

and

$$4|U_{e4}|^2(1-|U_{e4}|^2)\sin^2(\Delta m^2_{41}\frac{L}{E}) \tag{4.5}$$

respectively.

The analyses presented in the previous sections do not account for this effect, as it has a small effect on the analysis and requires the addition of a third parameter. Instead of expressing the oscillation parameters as Δm^2 and $\sin^2 2\theta$, which contains the product of $|U_{e4}|$ and $|U_{\mu4}|$ as a single parameter, $|U_{e4}|$ and $|U_{\mu4}|$ would need to be split into two separate parameters since each disappearance effect is only dependent on one of them.

These disappearance effects are not strong enough to constrain these parameters individually, but the magnitude of the effect on the analysis is explored by assuming equal muon and electron flavor disappearance, that is:

$$|U_{e4}|^2 = |U_{\mu4}|^2 = \sqrt{\frac{\sin^2 2\theta}{4}}. \tag{4.6}$$

The result of this study is that in the best fit parameters shift from $\Delta m^2 = 0.043$ eV^2, $\sin^2 2\theta = 0.88$ to $\Delta m^2 = 0.177$ eV^2, $\sin^2 2\theta = 0.070$. The best fit χ^2 shifts from 5.0 to 5.4. The new best fit point is well within the allowed region from the original analysis. Since the χ^2 in that region is shallow, this represents a negligible change. The change in χ^2 for the rest of the parameter space is similarly negligible. For example, the χ^2 of the point at $\Delta m^2 = 0.5$ eV^2, $\sin^2 2\theta = 0.01$ changes from 6.2 to 6.7.

The reason including the effects of disappearance is minimal is that the absolute normalization of the ν_μ sample is not well constrained, and thus absorbs most of the

effects of the disappearance. For the ν_e sample, the magnitude of the disappearance is also well within errors on the ν_e background.

4.6 Multinucleon Effects

Energy reconstruction (Section 3.6) assumes an independent particle model, taking the bound nucleons of the carbon nuclei to be independent and described by the Fermi Gas model. Multinucleon effects, which remain unaccounted for, have the potential to affect the visible energy in the detector. This could change the energy distributions for the backgrounds. Fortunately, many of the gamma background measurements (such as the π^0 background) are determined from direct measurements in the detector, reducing any potential effect on the energy distributions.

Several models exist which attempt to account for multinucleon processes. In an effort to study whether accounting for these effects changes the result of the oscillation analysis, the model of Reference [94] was used to form event predictions. The result of this test is that the antineutrino best fit point shifted from $\Delta m^2 = 0.043$ eV^2, $\sin^2 2\theta = 0.88$ to $\Delta m^2 = 0.059$ eV^2, $\sin^2 2\theta = 0.64$, shifting the χ^2 from 5.0 to 5.4. As in the previous section, this represents a negligible change considering how shallow the χ^2 region is in this area. A test point at $\Delta m^2 = 0.5$ eV^2, $\sin^2 2\theta = 0.01$ yields a shift from a χ^2 of 6.2 to 6.7.

Chapter 5

Global Fits

In the previous chapter, MiniBooNE was analyzed as a stand-alone experiment. However, to interpret the data within $3 + N$ sterile neutrino models, it is necessary to include results from other data sets. This is done within the context of global fits, described here. In this chapter, I discuss the experiments included in our fits, the fitting procedure, and the fit results. Our fits are consistent with global fits from other groups [95, 96].

5.1 Experiments Included in the Fits

In order to fully constrain a sterile neutrino model that describes the present anomalies, one must include all of the muon-to-electron appearance, muon disappearance and electron disappearance data that constrain the parameter space. Table 5.1 provides a list of all of the data sets which we use in the global fits. It lists information on what type of search was done, the number of bins used in the experiment, the energy range explored by the experiment and the average baseline.

Figures 5-1, 5-2, and 5-3 show the parameter space addressed by these experiments at 90% and 99% CL. Note that some experiments show signals while other experiments provide limits, excluding the space to the upper right of the limit. In this section we review the experiments, beyond the MiniBooNE appearance data discussed previously, that contribute to our fits.

Dataset	Process	N_{bins}	Energy	Average Baseline
LSND	$\bar{\nu}_\mu \to \bar{\nu}_e$	5	20 - 53 MeV	29.8 m
KARMEN	$\bar{\nu}_\mu \to \bar{\nu}_e$	9	16 - 50 MeV	17.7 m
BNB-MB(νapp)	$\nu_\mu \to \nu_e$	18	200 - 3000 MeV	541 m
BNB-MB($\bar{\nu}$app)	$\bar{\nu}_\mu \to \bar{\nu}_e$	18	200 - 3000 MeV	541 m
NuMI-MB(νapp)	$\nu_\mu \to \nu_e$	10	200 - 3000 MeV	745 m
NOMAD	$\nu_\mu \to \nu_e$	30	2.5 - 40 GeV	0.6 km
BNB-MB(νdis)	$\nu_\mu \to \nu_\mu$	16	200 - 1900 MeV	745 m
CCFR84	$\nu_\mu \to \nu_\mu$	18	40 - 230 GeV	0.715 km, 1.116 km
CDHS	$\nu_\mu \to \nu_\mu$	15	500 - 7000 MeV	130 m, 885 m
MINOS-CC	$\bar{\nu}_\mu \to \bar{\nu}_\mu$	25	0.5 - 50 GeV	730 km
ATM	$\nu_\mu \to \nu_\mu$	1	-	-
Bugey	$\bar{\nu}_e \to \bar{\nu}_e$	60	1 - 6 MeV	15 m, 45 m, 90 m
Gallium	$\nu_e \to \nu_e$	4	430, 750, 812 keV	$\sim$ 1 m
KARMEN/LSND(xsec)	$\nu_e \to \nu_e$	11	28 - 50 MeV	17.7 m, 29.8 m

Table 5.1: Details about the process, energy range, and baseline for each data set used in the global fits.

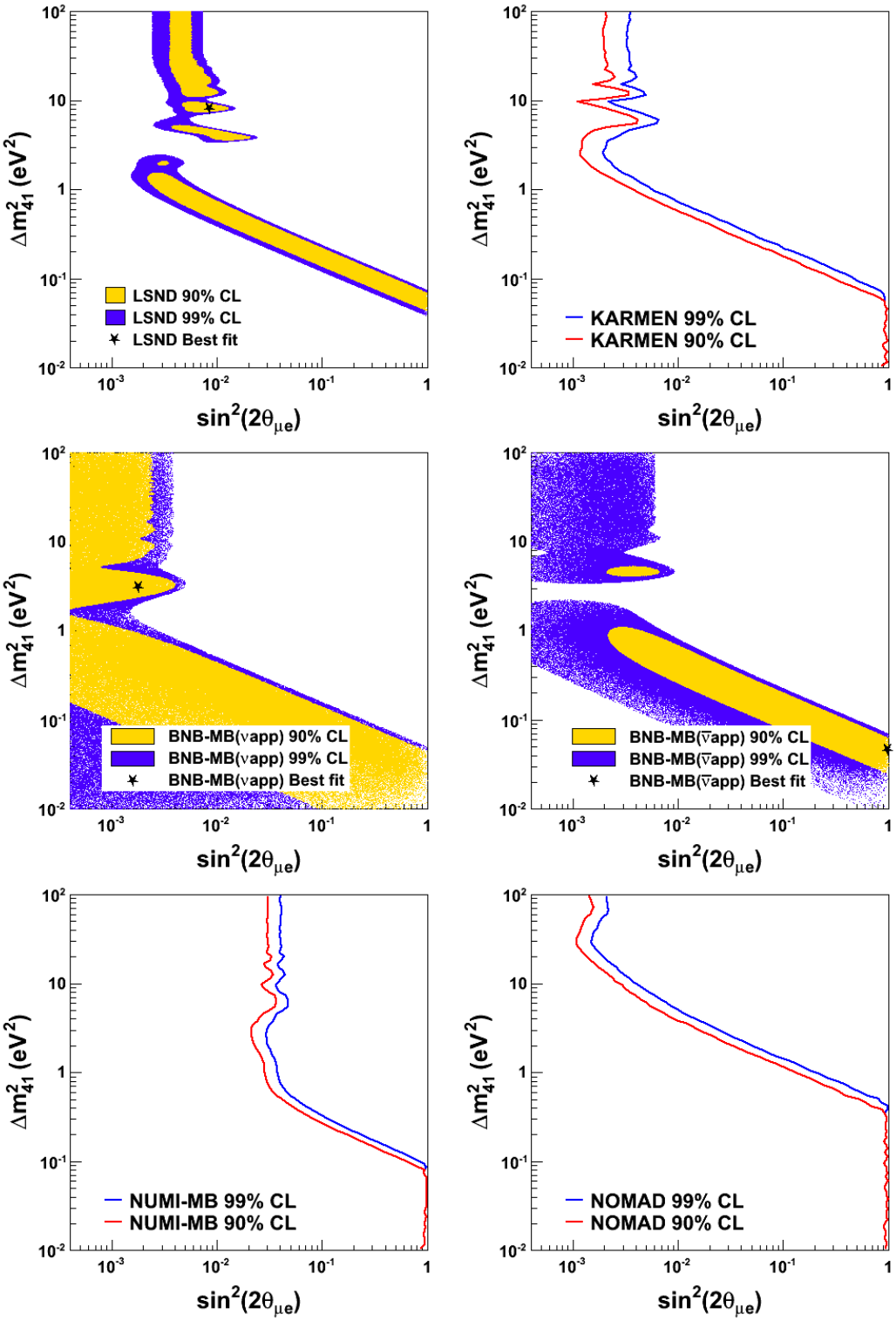

Figure 5-1: Summary of $\bar{\nu}_\mu \to \bar{\nu}_e$ and $\nu_\mu \to \nu_e$ results, shown at 90% and 99% CL. Top: LSND, KARMEN; middle: BNB-MB(νapp), BNB-MB($\bar{\nu}$app); bottom: NuMI-MB(νapp), NOMAD.

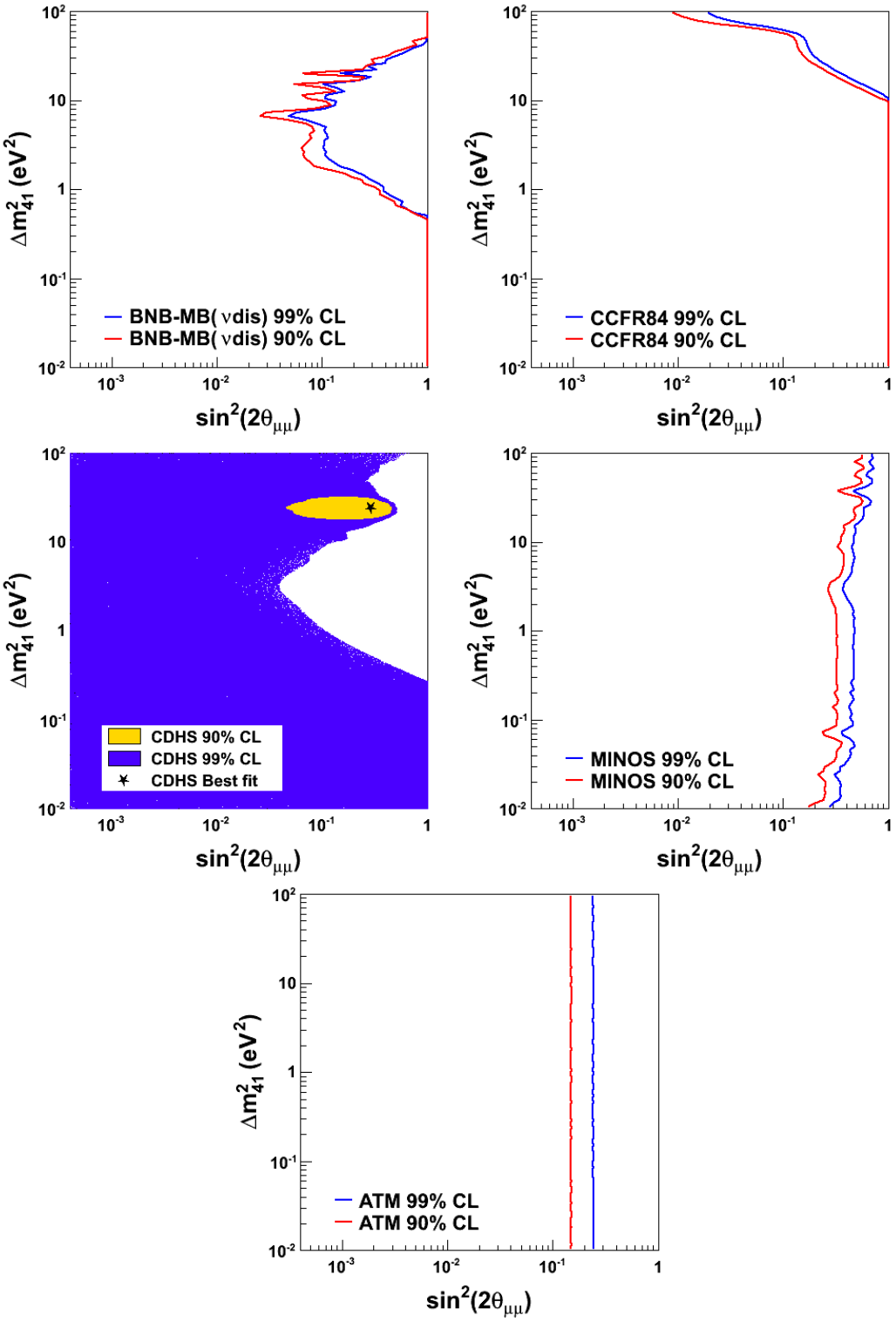

Figure 5-2: Summary of $\bar{\nu}_\mu \to \bar{\nu}_\mu$ and $\nu_\mu \to \nu_\mu$ results, shown at 90% and 99% CL. Top: BNB-MB(νdis), CCFR84; middle: CDHS, MINOS; bottom: ATM.

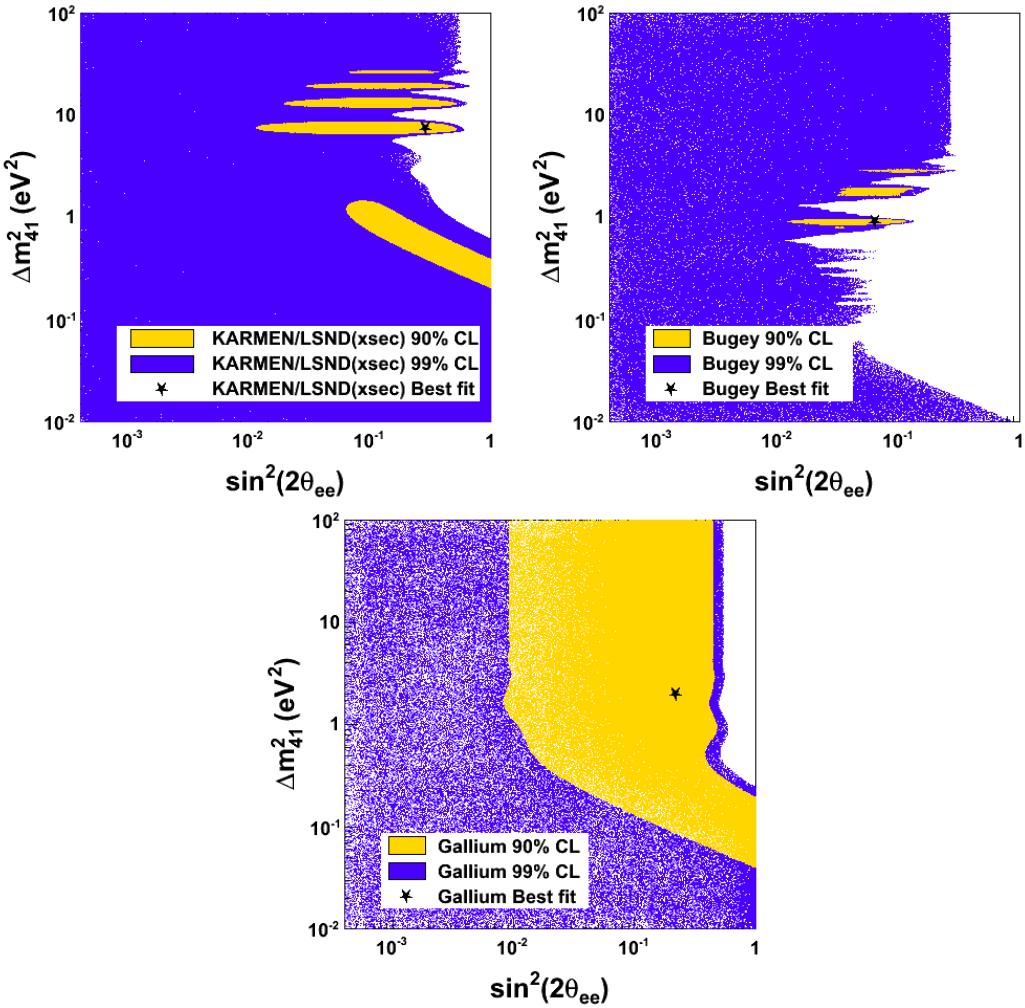

Figure 5-3: Summary of $\bar{\nu}_e \to \bar{\nu}_e$ and $\nu_e \to \nu_e$ results, shown at 90% and 99% CL. Top: KARMEN/LSND(xsec), Bugey; bottom: Gallium.

5.1.1 Muon-to-Electron-Flavor Appearance

LSND $\bar{\nu}_\mu \to \bar{\nu}_e$

LSND [40] used a Decay At Rest (DAR) beam on a lightly doped scintillator target to search for $\bar{\nu}_\mu$ to $\bar{\nu}_e$ appearance. The details of the detector and beam are discussed in detail in Section 2.1.1. LSND observed a signal corresponding to an oscillation with a mass splitting on the order of 1 eV^2 at 3.8σ. This anomalous result has still not been resolved as of today and is discussed in Section 2.1.1.

Energy resolution and smearing due to the size of the detector are taken into account in our analysis. The neutrino energy is reconstructed by comparing the measured prompt positron energy with the predicted positron spectrum correlating the positron energy with the neutrino energy [97]:

$$E_{\bar{\nu}_e} = E_{e^+} + 0.78 \text{ MeV}. \tag{5.1}$$

KARMEN $\bar{\nu}_\mu \to \bar{\nu}_e$

KARMEN [93] also used a DAR beam and so operated in the same energy regime as LSND, though with a shorter baseline (see Table 5.1), which shifts the sensitivity region. It also had lower statistics due to a less intense beam (0.2 mA for KARMEN *vs.* 1 mA for LSND). While LSND was located almost directly downstream of the target, at an angle of around 30 degrees, KARMEN was at a much larger angle of 90 degrees. This considerably reduced their $\bar{\nu}_e$ background from the few pion decay-in-flight events.

KARMEN was located at Rutherford Laboratory in the UK and used the ISIS neutrino beam. It did not see a signal at 90% CL and as can be seen in Figure 5-1, excludes the top portion of the LSND signal. KARMEN detects neutrinos through inverse beta decay. It utilized a highly doped segmented detector and used gadolinium paper wrapped around their scintillator modules to capture the outgoing neutron from the interaction. Like LSND, the signature for anti-electron neutrino detection was a prompt positron followed by delayed γ signal, as described in Section 2.1.1, and therefore followed a similar analysis procedure as LSND.

MiniBooNE $\nu_\mu \to \nu_e$ and $\bar{\nu}_\mu \to \bar{\nu}_e$

MiniBooNE was built to explicitly explore the LSND anomaly with a different detector design and different systematics. It used a pion decay in flight beam with a higher energy spectrum and longer baseline, but preserving $L/E \sim 1$ to probe the same region of Δm^2 parameter space.

The MiniBooNE experiment and analysis are described in detail in Chapters 3 and 4. The analysis of this chapter follows the analysis described in Chapter 4, oscillating MC ν_μ events, using the full error matrix, and constraining the ν_e appearance sample with measured ν_μ events (Section 4.1). This analysis includes the full MiniBooNE neutrino (6.46×10^{20} POT) and antineutrino (11.27×10^{20} POT) datasets. We use

a log likelihood minimization for the contribution from MiniBooNE as described in Section 4.2.1.

MiniBooNE was also able to detect off-axis neutrinos from the nearby NUMI beam, primarily used for the MINOS experiment. This dataset is isolated from the neutrino flux coming from the Booster beam because there is no time overlap of the proton pulses. Both beams are pulsed with small duty-factors ($\sim 10^{-5}$). The neutrinos from the NUMI beam have an average baseline of 745 m compared with the 541 m baseline of the BNB, and are 6.3° off-axis. An analysis was performed using these events in neutrino mode. This sample is generated from an off-axis beam where most of the neutrinos are coming from kaon decays. The three-body kaon decay increases the ν_e background. The analysis follows the usual appearance analysis and is called "NUMI-MB" in these fits. More information can be found in References [98] and [99].

NOMAD $\nu_\mu \to \nu_e$

The NOMAD experiment [100] used the Super Proton Synchrotron (SPS) beamline at CERN, which accelerates protons up to an energy of 450 GeV, to create a high energy muon neutrino source. NOMAD was originally built to explore $\nu_\mu \to \nu_\tau$ oscillations in the 1980s and early 1990s, when the ν_τ was thought to be a candidate for dark matter. Δm^2_{32} was previously unmeasured, and could have potentially been large (> 1 eV^2). No oscillations to ν_τs were observed, but a $\nu_\mu \to \nu_e$ search was also performed. The limits obtained by this analysis are shown in Figure 5-1.

The 1.7 ton NOMAD detector contains a collection of forty-four 3 m $\times$ 3 m drift chambers surrounded by a 0.4 T dipole magnet with internal dimensions of 3.5 m $\times$ 3.5 m $\times$ 7 m. Transition radiation detector modules and an electromagnetic calorimeter are located inside of the magnet, followed by hadronic calorimeters and muon chambers.

5.1.2 Muon Flavor Disappearance

MiniBooNE $\nu_\mu \to \nu_\mu$

MiniBooNE also performed a ν_μ disappearance analysis [101]. The search was done in both neutrino and antineutrino mode, but as the antineutrino mode data is too weak to have a noticeable affect the fits, we only include the neutrino mode data. A shape-only analysis was performed, meaning that the predicted spectrum for a given Δm^2_{41} and $\sin^2 2\theta_{\mu e}$ model was renormalized to the number of observed events for comparison with data. Statistical and shape-only systematic errors are included using a covariance matrix.

The CL contours in the original analysis (Reference [101]) were drawn using a Pearson χ^2 test, calculating the number of degrees of freedom through fake data studies, and then drawing confidence level intervals based on 16 DOF. This method uses the absolute χ^2 to draw the contours. For example, a χ^2 of 23.5 corresponds to a 90% probability for 16 DOF, so all points with a χ^2 less than or equal to 23.5 are

included in the 90% CL region. In our treatment of this dataset for drawing global CL intervals, we use the $\Delta\chi^2$ procedure (Section 5.2), to maintain consistency with our other datasets.

CCFR84 $\nu_\mu \to \nu_\mu$

CCFR84 [102] consisted of two detectors, both calorimeters, consisting of segmented steel and scintillator plates, located at Fermilab. They were located at baselines of 715 m and 1116 m, serving as near and far detectors respectively. CCFR84 detected muon flavored neutrinos through the charged current interaction. Since it was a two-detector experiment, it compared a ratio of events in the near detector *vs.* the far detector to prediction.

CDHS $\nu_\mu \to \nu_\mu$

CDHS [103] was similar in design to CCFR84, located at CERN at two baselines and consisting of two calorimeter detectors with interspersed iron and scintillator plates, with the near detector at 130 m and the far detector at 835 m. It also searched for muon flavor disappearance through the charged current interaction.

It may be surprising to see the closed contours in Figure 5-2 at 90% CL which seem to be contradictory to Reference [103]. The reason for this is that we are using $\Delta\chi^2$ from the overall minimum, for two degrees of freedom, to create our plot. Alternatively, the CDHS collaboration used a raster scan approach, using 1 degree of freedom and taking the $\Delta\chi^2$ from the minimum χ^2 in each bin slicing up the Δm^2 axis. We have chosen to represent data using the 2-dimensional approach for all experiments which have closed contours at 90% CL (Note that this does not change the χ^2 at each point and therefore does not affect the global fits).

MINOS $\bar{\nu}_\mu \to \bar{\nu}_\mu$

Minos is a long baseline ν_μ disappearance experiment located along the NuMI beamline at Fermilab. Tuned to the atmospheric oscillation parameters, the near and far detectors are located at 1 km and 730 km respectively. The far detector is sensitive to disappearance from sterile neutrino oscillations, which would manifest as a deficit of events in the far detector. No deficit was observed, meaning the data can be used to set a limit on the magnitude of muon-flavored disappearance The antineutrino-mode data is included in our fits as we were lacking a $\bar{\nu}_\mu$ disappearance constraint. The ν_μ disappearance parameter space covered by MINOS is better constrained by the ATM data set described below, and the MiniBooNE dataset described above. Therefore it is not included in our fits.

Our analysis uses both the antineutrino data from Reference [104] and the wrong-sign (antineutrino contamination from neutrino-mode running) data from Reference [105]. We use the far to near detector ratio, allowing for oscillations in the near detector in addition to the far detector, depending on each mass and mixing model. We also include Δm^2_{atm} in the oscillation probability using published values and errors for the atmospheric mass and mixing parameters measured by MINOS [106].

There has recently been a more robust analysis done by the MINOS collaboration [107] which we plan to include in our fits once the details of the analysis become available. It leads to a similar contour so this update will not significantly affect the fit results.

ATM $\nu_\mu \to \nu_\mu$

The ATM dataset refers to a constraint on muon flavored neutrino mixing based on world atmospheric oscillation data. The constraint is on the total muon flavor composition allowed in the fourth mass state and is implemented using the parameter d_μ:

$$d_\mu = \frac{1 - \sqrt{1 - 4A}}{2} \ , \tag{5.2}$$

$$\begin{aligned} A = (1 - |U_{\mu 4}|^2 - |U_{\mu 5}|^2 - |U_{\mu 6}|^2)(|U_{\mu 4}|^2 + |U_{\mu 5}|^2 + |U_{\mu 6}|^2) \\ + |U_{\mu 4}|^2 |U_{\mu 5}|^2 + |U_{\mu 4}|^2 |U_{\mu 6}|^2 + |U_{\mu 5}|^2 |U_{\mu 6}|^2 \ . \end{aligned} \tag{5.3}$$

The parameter d_μ is then compared to measurements, which come primarily from Super-K and K2K. This analysis is detailed in Reference [108]. The constraint is taken to be a neutrino dataset in our fits as it mostly consists of neutrino data, though there is a small antineutrino component.

5.1.3 Electron Flavor Disappearance

KARMEN/LSND(xsec) $\nu_e \to \nu_e$

The KARMEN and LSND experiments measured cross-sections of ν_e scattering on Carbon (separately from the oscillation searches):

$$\nu_e +^{12} \mathrm{C} \to^{12} \mathrm{N} + e^- . \tag{5.4}$$

Given the difference in baselines and similarity of the neutrino energies and detectors, one can search for an inconsistency in these measurements due to ν_e disappearance. The correlated systematics of the two detectors are taken into account and the analysis proceeds as described in Reference [109]. Note that in References [109], 95% limits were shown which do not show closed contours, however there are closed contours at the 90% CL as seen in Figure 5-3. Reference [36] shows that our 95% contours match those of the original analysis.

BUGEY $\bar{\nu}_e \to \bar{\nu}_e$

BUGEY was a three-detector reactor experiment located at 15, 45, and 90 m from the reactor. The analysis has changed since the 1994 BUGEY publication of Reference [110] due to reanalysis of the reactor flux predictions [46, 47], further discussed in

Section 2.1.3. Although there has been recent controversy over the new predictions [50], there is no corresponding quantitative information at this time to update our fits. For this reason, we continue to use the predictions of Reference [47]. We choose to represent the reactor anomaly only through the BUGEY experiment, as it is the strongest constraint and allows us to avoid the correlated systematics between the various reactor experiments.

Gallium $\nu_e \to \nu_e$

Low-energy ^{51}Cr and ^{37}Ar ν_e sources were inserted into the GALLEX [6] and SAGE [7] solar neutrino detectors for calibration. The short baseline and low energies allow sensitivity to ν_e disappearance, and a signal is seen [52]. This result is discussed in greater detail in Section 2.1.4.

In the analysis, the rate of expected events for a given mass and mixing model is integrated over the detector volume and compared with the null hypothesis. This follows the analysis of Reference [52]. This analysis uses the cross-sections from 2010. Updates to these cross-sections are expected to have only a minor impact on the fits but will be included in the analysis in a future update.

5.2 Fitting Procedure

In this section, the fitting procedure is described for a $3+1$ model, but $3+N$, with $N > 1$, follows the same procedure. As described in Section 2.2.1), $\Delta m^2_{41} \gg \Delta m^2_{31} > \Delta m^2_{21}$, so m_1, m_2, and m_3 can be taken as degenerate. This means that a $3+1$ model is a simple two-neutrino model between the degenerate first three mass states and the fourth state. As in Equation 1.11, the probability for two-neutrino oscillations is usually expressed as:

$$P = \sin^2 2\theta \ \sin^2 \left(\frac{1.27 \ \Delta m^2 \left(\mathrm{eV}^2\right) \ L \left(\mathrm{km}\right)}{E \left(\mathrm{GeV}\right)} \right) \ , \tag{5.5}$$

where $\sin^2 2\theta$ can also be expressed in terms of the mixing parameters as $4|U_{e4}|^2|U_{\mu 4}|^2$ for appearance experiments or $4|U_\mu|^2(1-|U_\mu|^2)$ or $4|U_\mu|^2(1-|U_e|^2)$ for disappearance experiments. This results in 3 parameters for a $3+1$ fit to both appearance and disappearance type experiments ($\Delta m^2_{41}, |U_{e4}|$, and $|U_{\mu 4}|$).

For a particular point in parameter space, a prediction using the corresponding oscillation parameters is calculated and compared with the data from each experiment. The individual χ^2's (one from each experiment) are summed together to form a global χ^2, and the point with the lowest χ^2 is considered the best-fit point.

The best-fit point is found using a Markov Chain minimization procedure [111]. This begins by choosing a random point in parameter space as a starting position, testing the χ^2, and stepping to a new position. The probability that the new point is accepted as the next point in the chain is:

$$P = min(1, e^{-(\chi^2 - \chi^2_{old})/T}), \tag{5.6}$$

where T is the Markov Chain parameter "temperature". The temperature controls how quickly the Markov Chain diffuses toward the minimum χ^2 value. Points with a lower χ^2 value than the proceeding point are always accepted, and points with a higher χ^2 value than the proceeding point are more likely to be accepted the closer their value is to the proceeding point. There will always be some probability that even a point with a high χ^2 will be accepted. Higher temperature values will increase this probability, making it more likely for the chain to go in the "wrong" direction, but also preventing the chain from getting stuck in local minima.

If the point is accepted, the chain will take a step from the new point. If it is rejected, the chain will backtrack to the proceeding point and take a new step from there. The size of the step is determined by another user-set Markov chain parameter called the "stepsize", where the step taken is randomly chosen within the defined stepsize. So the new value for parameter x will be:

$$x = x_{old} + s(R - 0.5)(x_{min} - x_{max}), \tag{5.7}$$

where x_{old} is the value of the parameter previously tested in the χ^2 minimization chain; x_{min} and x_{max} represent the boundaries on the parameter x; R is a random number between 0 and 1, which is varied as one steps from x_{old} to x; and s is the user-defined stepsize. The values of temperature and stepsize are optimized by varying them and calculating how quickly the best-fit point is converged upon for a variety of values. Multiple (randomly determined) initial start-points, and their resulting Markov chains, are used for each fit to crosscheck convergence upon the same parameters.

Closed contours are drawn in two-dimensional parameter space by assuming Gaussian errors and using $\Delta\chi^2$ cuts on $\Delta\chi^2 = \chi^2 - \chi^2_{min}$ for dof. This cut on $\Delta\chi^2$ is 4.61 for 90% Confidence Level (CL) regions and 9.21 for 99% CL regions. When the null point is allowed at 90 % CL, we instead draw raster scan limits with 1 dof. The raster scan limits involve splitting up the parameter space into bins that slice up the Δm^2 space. The $\Delta\chi^2$ is then determined using the minimum χ^2 in each bin rather than the global minimum χ^2 value. We choose to draw contours using the $\Delta\chi^2$ method, contrary to the Feldman-Cousins method using fake-data-studies described in Section 4.2.2. A full fake-data analysis for every experiment in our fits would require prohibitively large amounts of computing time.

We also quote a compatibility resulting from a Parameter Goodness-of-fit test (PG test) to compare datasets [112]. This test aims to reduce biases introduced when comparing experiments with drastically different numbers of bins, as it treats each experiment equally rather than each bin equally. This also solves dilution effects which arise when experiments contain bins that are not actually sensitive to the oscillation parameters.

The PG test quantifies a compatibility, given by:

$$PG = Prob(\chi^2_{PG}, ndf_{PG}), \tag{5.8}$$

where χ^2_{PG} and ndf_{PG} are unique to this statistic [112]. The χ^2_{PG} is calculated by subtracting the minimum χ^2 from each dataset that is to be tested from the global minimum point:

$$\chi^2_{PG} = \chi^2_{min,global} - \sum_d \chi^2_{min,d}, \tag{5.9}$$

where d runs over the datasets to be compared. $\chi^2_{min,global}$ represents the minimum χ^2 value found when all datasets are fit simultaneously. $\chi^2_{min,d}$ represents the minimum χ^2 value obtained when fitting only the experiments within the specified dataset. For example, if comparing neutrino *vs* antineutrino datasets, $\chi^2_{min,global}$ represents the minimum χ^2 when fitting all 14 experiments from Section 5.1. The two values of $\chi^2_{min,d}$ would be $\chi^2_{min,\nu}$ and $\chi^2_{min,\bar{\nu}}$. $\chi^2_{min,\nu}$ would be the minimum χ^2 from a fit to only the 9 neutrino datasets and $\chi^2_{min,\bar{\nu}}$ would be a fit to only the 5 antineutrino datasets (as distinguished in Table 5.1).

The number of degrees of freedom used in the PG test is given by:

$$ndf_{PG} = \sum_d N_{p,d} - N_{p,global}. \tag{5.10}$$

Here, $N_{p,d}$ represents the number of independent parameters for dataset d and $N_{p,global}$ represents the number of independent parameters in the global fit. For example, if comparing neutrino *vs* antineutrino datasets within a 3+1 model, there would be three independent parameters for each dataset (Δm^2, U_{e4}, and $U_{\mu 4}$), meaning that ndf_{PG} would be $3 + 3 - 3 = 3$.

This fit is independent of the number of bins in each experiment due to subtraction of these χ^2 values. In addition, bins which are not sensitive to the fit parameters will have the same χ^2_{min} for the global best-fit and for the "individual dataset" best-fit, and therefore not contribute to the PG test.

5.3 Results

Table 5.2 shows the χ^2 values and probabilities for each of the models. We find a 55% probability for the $3 + 1$ model, which slightly improves to 69% for the $3 + 2$ model. There is no further improvement for the $3 + 3$ model, with a probability of 67%. Contours for $3 + 1$ and $3 + 2$ global fits can be seen in Figures 5-4 and 5-5 respectively.

In order to explore where incompatibilities in the datasets lie, they are also split into subsets in order to perform the PG test. These results are shown in Table 5.3. The PG test suggests that tension exists among both divisions—neutrinos *vs.* antineutrinos and appearance experiments *vs.* disappearance experiments—in a $3+1$ model. The addition of a CP violating terms in the $3 + 2$ model begins to relieve the tension between neutrinos and antineutrinos, also leading to an improved overall fit. This tension is further relieved in the $3 + 3$ model, though we do not observe an increase in the quality of the fit in going from $3 + 2$ to $3 + 3$.

The tension between appearance and disappearance experiments, however, does

	χ^2_{min} (dof)	P_{best}
Null	286.5 (240)	2.1%
3+1	233.9 (237)	55%
3+2	221.5 (233)	69%
3+3	218.2 (228)	67%

Table 5.2: The χ^2 values and corresponding probabilities for the best-fit points to the models considered.

		χ^2_{PG} (dof)	PG(%)
3+1	ν vs. $\overline{\nu}$	15.6 (3)	0.14%
	App vs. Dis	17.8 (2)	0.013%
3+2	ν vs. $\overline{\nu}$	13.9 (7)	5.3%
	App vs. Dis	23.9 (4)	0.0082%
3+3	ν vs. $\overline{\nu}$	10.9 (12)	53%
	App vs. Dis	27.1 (6)	0.014%

Table 5.3: The compatibility between appearance *vs.* disappearance experiments and neutrino *vs.* antineutrino experiments for each model.

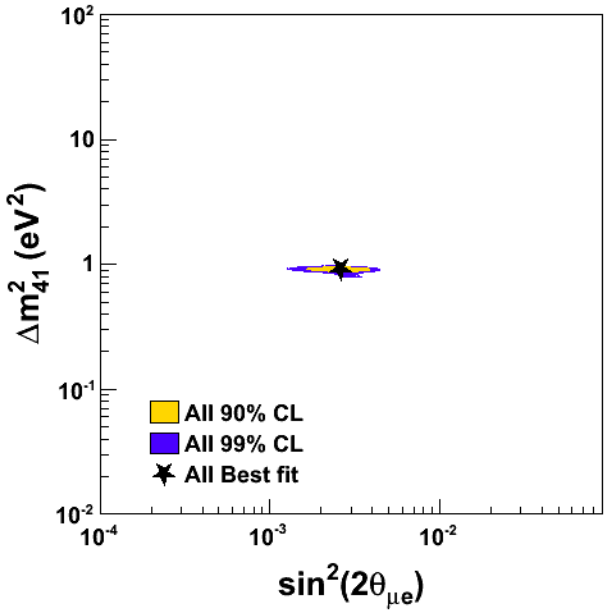

Figure 5-4: Confidence level contours projected onto two-dimensional parameter space (Δm^2_{41} *vs.* $\sin^2(2\theta_{\mu e})$) from a $3+1$ global fit. From Reference [36].

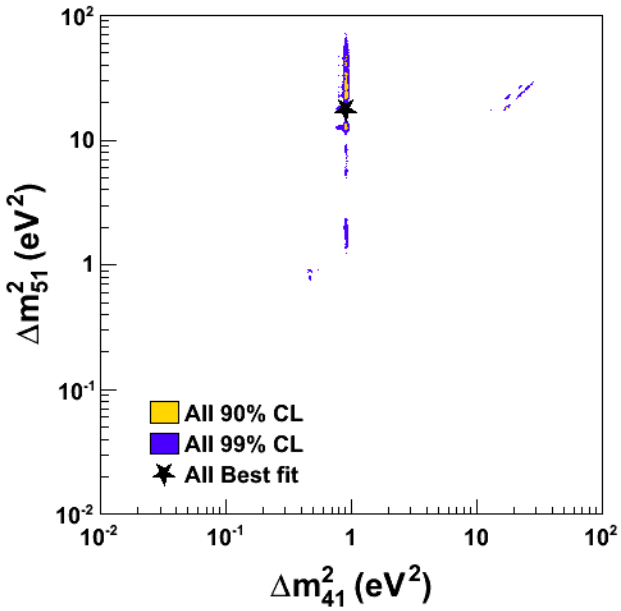

Figure 5-5: Confidence level contours projected onto two-dimensional parameter space (Δm^2_{51} *vs.* Δm^2_{41}) from a $3+2$ global fit. From Reference [36].

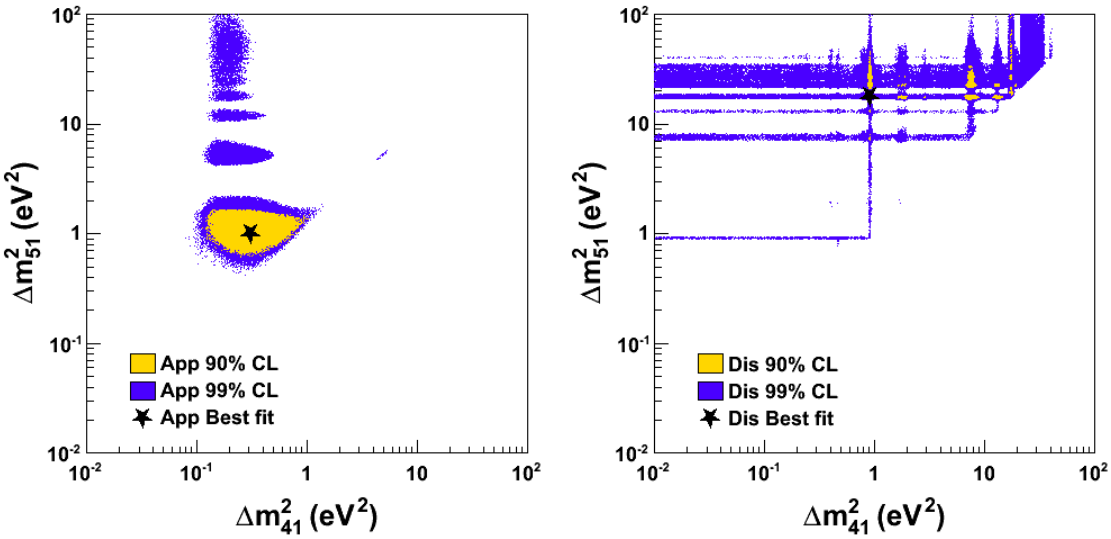

Figure 5-6: Confidence level contours projected onto two-dimensional parameter space (Δm^2_{51} *vs.* Δm^2_{41}) resulting from a $3+2$ fit to appearance experiments (left), and disappearance experiments (right). From Reference [36].

not improve with additional sterile states. It can be seen in Figure 5-6 that the appearance and disappearance fits exclude the favored regions of the other. A large contributor to this tension can be seen by comparing the results of these fits with the MiniBooNE data (Figure 5-7). The MiniBooNE low energy excess drives the appearance fit into a region which is not allowed by the disappearance experiments.

Figure 5-8 shows the oscillation probability as a function of L/E for appearance and disappearance experiments for the best-fit points of these fits to $3+1$, $3+2$, and $3+3$ models. This exemplifies the sensitivity in L/E that will be required if future experiments are to observe these oscillations.

While the $3+N$ models considered produce better results than fits without sterile neutrinos, we find that current data are still insufficient to determine the viability of these models. Future experiments are necessary to further investigate these scenarios to confirm them or rule them out. There are a number of future and proposed experiments that will be sensitive to sterile neutrinos including many sensitive to the preferred parameter space from these fits. Some of these experiments will be discussed in Chapter 8.

5.4 Recent Constraints Since Published Work

The results presented in this section were published in Reference [36] and are now over a year old and therefore will be updated in the near future. I provide a discussion of potential updates in this section.

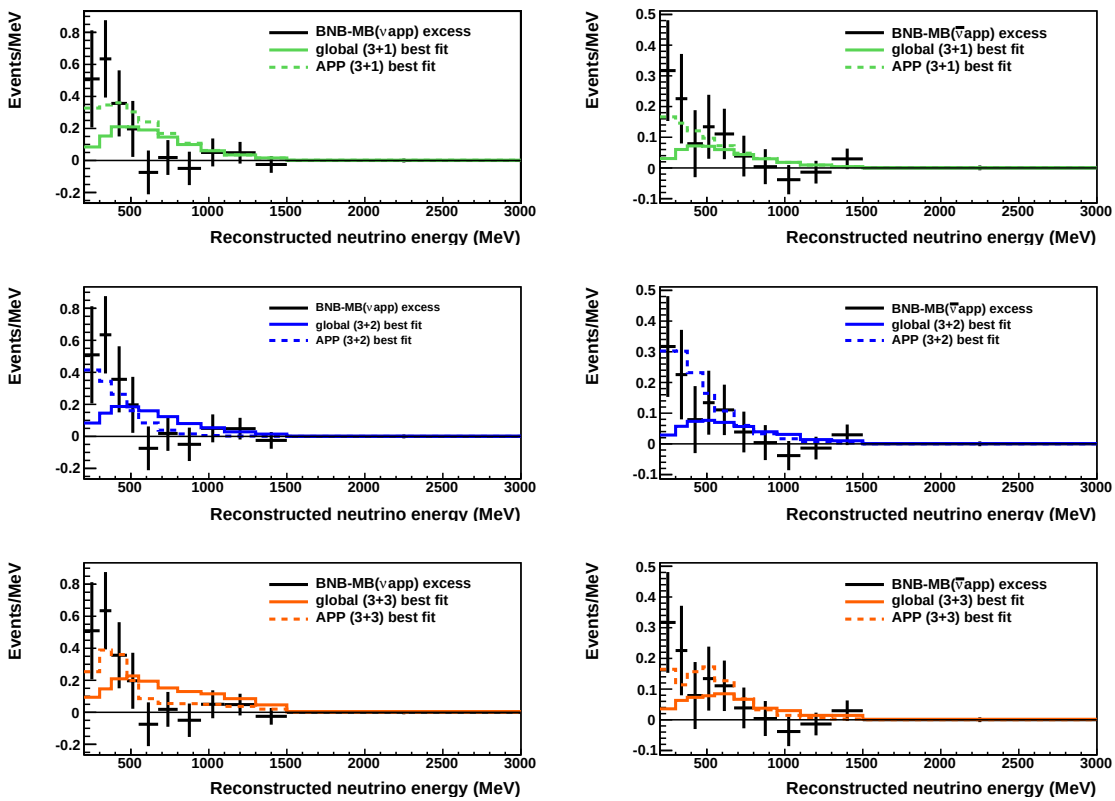

Figure 5-7: The MiniBooNE neutrino (left) and antineutrino (right) excess data with signal predictions for each of the global best-fit oscillation signal predictions, $3+1$ (top, green), $3+2$ (middle, blue), and $3+3$ (bottom, orange). The global best-fit predictions to all experiments are indicated by solid lines and the appearance-only fit results are indicated by dotted lines. From Reference [36].

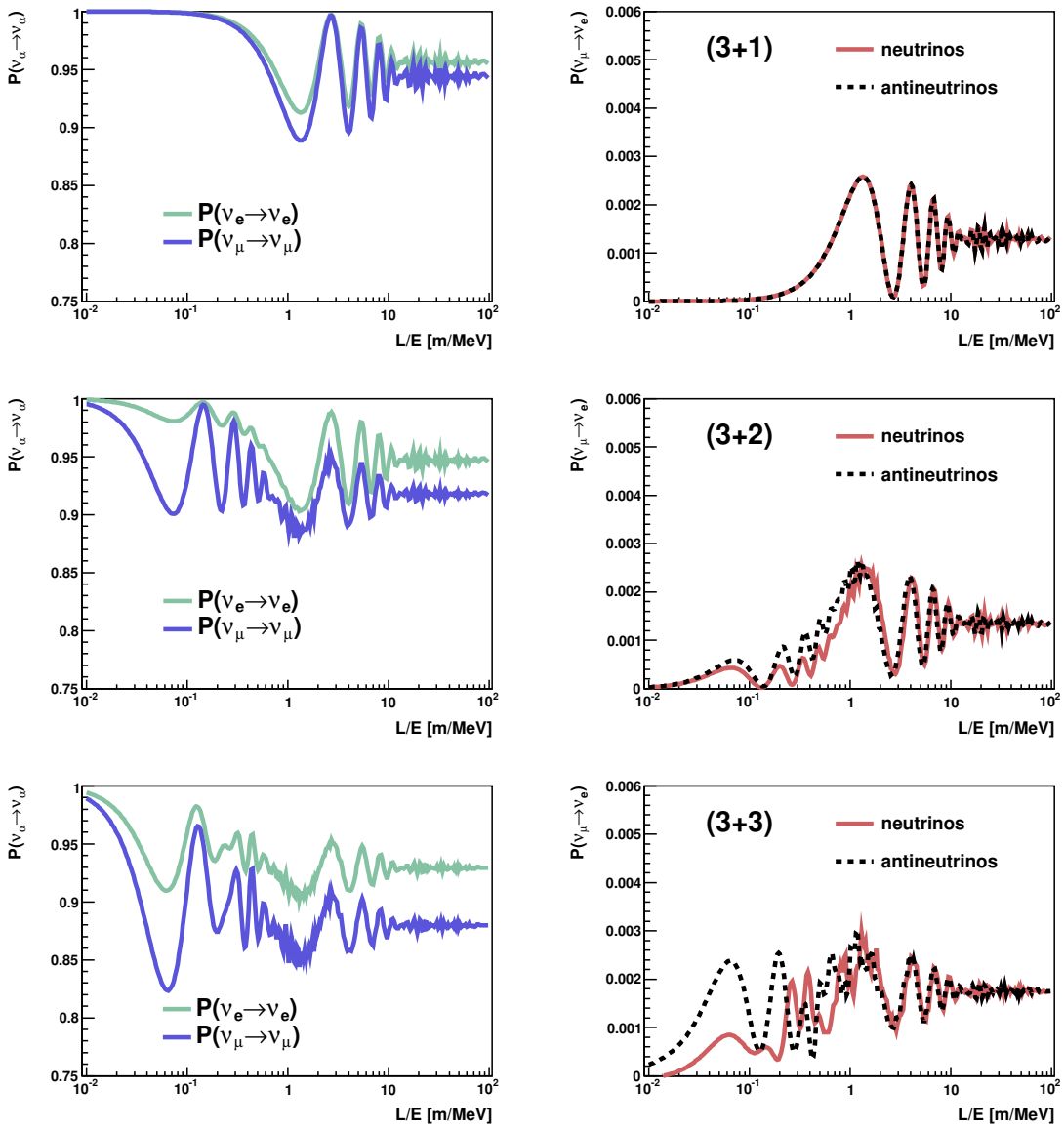

Figure 5-8: The $3+1$, $3+2$, and $3+3$ oscillation probabilities for the global best-fit values with 10% resolution in L/E. From Reference [36].

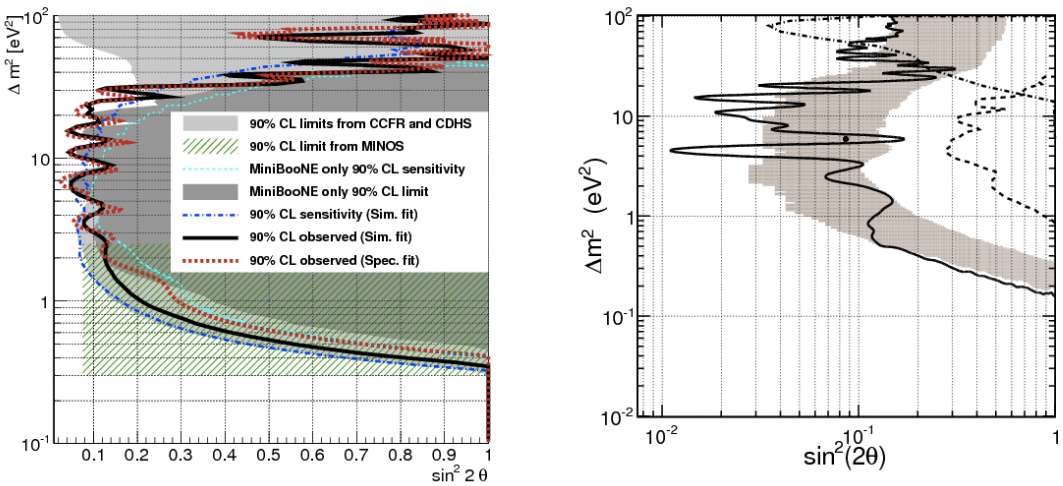

Figure 5-9: The limits from a MiniBooNE/SciBooNE dual-baseline search for muon neutrino (left, from [113] and antineutrino (right, from [114]) disappearance. Note that the neutrino mode x-axis is linear and the antineutrino mode axis is logarithmic. The limits for neutrino mode are indicated in the figure. For antineutrino mode, the solid line represents the MiniBooNE+SciBooNE disappearance analysis, the dotted line represents the MiniBooNE only disappearance analysis, and the dot-dashed line represents the CCFR limit.

5.4.1 MiniBooNE/SciBooNE

The MiniBooNE and SciBooNE collaborations performed a 2-detector fit to search for muon flavor neutrino and antineutrino disappearance [113, 114]. The limits are shown in Figure 5-9. These datasets will be included in the next iteration of our fits.

5.4.2 ICARUS

The ICARUS experiment did a search for electron flavor appearance in both neutrino and antineutrino modes [115], Figure 5-10. We plan to include these limits in our next iteration of fits, however, they are not expected to have a significant effect. This is because these limits are still weak compared to those of our other datasets, and so will not affect the global best-fit points.

5.4.3 OPERA

OPERA performed a search for ν_τ appearance from a ν_μ beam [116]. OPERA has set some limits on $|U_{\mu 4}|^2|U_{\tau 4}|^2$, however including this result requires the addition of the extra parameter, $U_{\tau 4}$, for a $3+1$ model and an additional parameter for each additional sterile state. Without separate limits on $U_{\tau 4}$, constraints on the product of $|U_{\mu 4}|^2|U_{\tau 4}|^2$ will not constrain $|U_{\mu 4}|$ in our fits. So while this does not provide

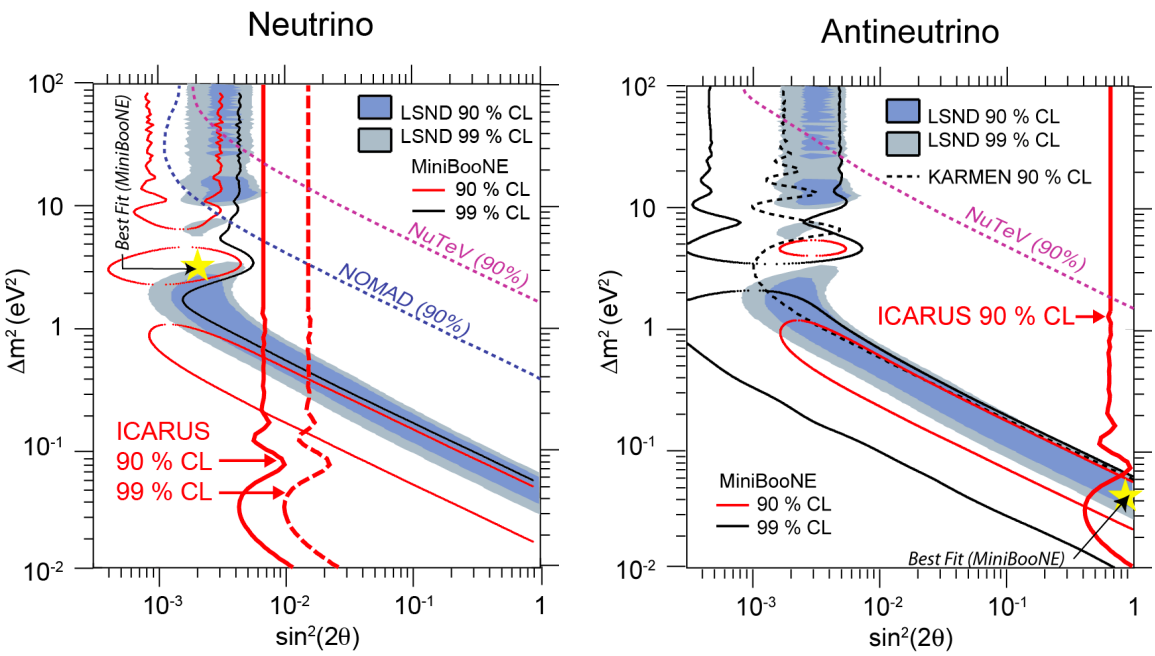

Figure 5-10: The limits from the ICARUS experiment for an electron-flavor appearance search for neutrino-mode (left) and antineutrino mode (right).

additional information for a global fit, it is an interesting result and we will explore ways to include this result in the future.

Chapter 6

MicroBooNE

6.1 Overview

MicroBooNE [117] is a Liquid Argon Time Projection Chamber (LArTPC). The experiment is primarily motivated by the MiniBooNE low-energy excess (Chapter 4). Unlike MiniBooNE, MicroBooNE will be able to distinguish electrons from gammas, significantly reducing the γ-induced backgrounds which dominated the low-energy background in MiniBooNE. It is able to do this using the unique properties of a LArTPC, providing high-resolution reconstruction of charged particle tracks. Use of a track is much more powerful than use of a Cherenkov ring because the initial few centimeters of the track can be isolated and studied. The initial $\gamma \to e^+e^-$ can be detected and separated from an initial e^- using information about the energy deposited per unit distance (dE/dx) at the early points along the track.

MicroBooNE is an important step in the U.S. LArTPC program, demonstrating several components of LArTPC technology that will be necessary in scaling up the technology. Along the route of using LArTPCs for neutrino physics, MicroBooNE will follow ArgoNeuT [118] and Icarus [119], which have both made important contributions to the technology and related measurements. The technology developed for MicroBooNE will play a vital role in future LArTPCs such as LAr1-ND [120] and LBNF (formerly LBNE) [21]. These experiments, and others, are further discussed in Chapter 7.

MicroBooNE will demonstrate a 2.5 m long drift distance, a filling procedure that does not include prior evacuation of the vessel but still maintains ultra high purity LAr, a 120 kV high voltage with a drift field of 500 V/cm, and the development of cold electronics. These aspects are new to MicroBooNE and are critical to the success of scaling up the technology to significantly larger detectors. MicroBooNE is also developing the generic reconstruction and analysis tools necessary to achieving the predicted resolution and sensitivity.

MicroBooNE is located less than 100 m upstream of MiniBooNE, using the same beamline, at a baseline of 470 m. MicroBooNE will initially run with 6.6 $\times 10^{20}$ protons on target in neutrino mode, with a possible extension for antineutrino-mode running or additional neutrino-mode running. 6.6 $\times 10^{20}$ will provide enough neutrino

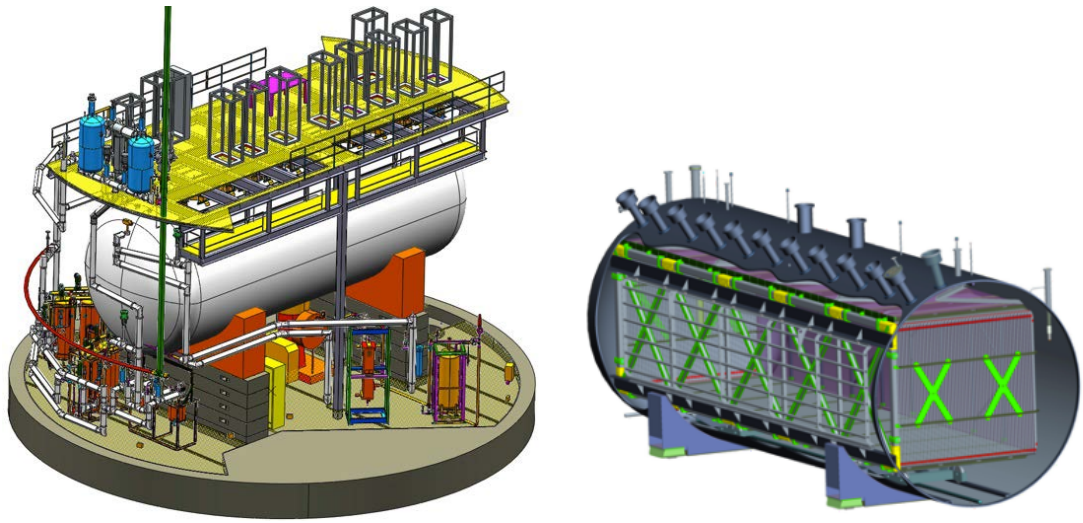

Figure 6-1: A schematic of the outside of the MicroBooNE cryostat (left) and internal TPC (right).

interactions to determine whether the MiniBooNE excess is due to electron-like events.

6.2 The MicroBooNE Detector

LArTPCs measure the ionization electrons liberated from argon atoms as charged particles traverse a volume of LAr. These ionization electrons are drifted by an applied electric field and measured with crossed wire planes, giving reconstruction information in three dimensions. Two dimensional information comes the detected position along the wire planes, and the third comes from the timing of when the ionization electrons reach the wire planes. MicroBooNE has 3 wire planes consisting of two induction planes and one collection plane. The vertically-oriented collection plane consists of 3456 wires and the induction planes, oriented at $\pm 60^o$, consist of 2400 wires each. Wires have a separation of 3 mm. Scintillation light is also produced as charged particles pass through the argon, and is detected by an array of 32 PMTs located behind the wire planes. The PMT system is discussed in more detail in Section 6.3.

The MicroBooNE TPC volume is is 10 m $\times$ 2.3 m $\times$ 2.5 m and contains a total of 170 tons of LAr, 70 of which make up the fiducial volume. A schematic of the MicroBooNE detector is in Figure 6-1, and a photo in Figure 6-2.

MicroBooNE has overcome many challenges associated with scaling up prior technology. For example, It has designed and implemented new cool-down, refrigeration, and purification systems. High voltage breakdown within an ultra-pure noble liquid has become a major concern across liquid-noble-gas TPCs. MicroBooNE has solved this issue by inserting surge protection devices [121].

Figure 6-2: The MicroBooNE TPC and cryostat. The TPC is on a rail system, allowing it to slide in and out of the cryostat.

6.2.1 Event Signatures and e-γ Separation

LArTPC technology provides high-efficiency reconstruction of particle tracks. An example event display is shown in Figure 6-3. LArTPCs use dE/dx information and event topology to identify neutrinos and to distinguish electrons from gammas. Figure 6-3 shows an example of reconstruction of MC muon, electron, and π^0 events. Instead of a solid ring as in a Cherenkov detector, the long track of a muon is fully visible and its dE/dx measured as a function of position. The Michel electron is also visible from the muon decay in this event. Instead of a fuzzy ring as a byproduct of the electromagnetic shower induced by an electron, the full shower is reconstructed. And instead of two fuzzy rings from the shower induced by each γ in a $\pi^0 \to \gamma\gamma$ background event, two distinct showers can be seen. In addition, the spacing between the vertex and the shower initialization is visible in-between the invisible tracks of the π^0 and γ before the $\pi^0 \to \gamma\gamma$ and $\gamma \to e^+e^-$ reactions.

In the case of the π^0 reconstruction, the MiniBooNE background where one of the γ's is not detected is not important for MicroBooNE. Both γ's will be visible at much lower energies than in MiniBooNE. When only one γ is present, such as the case of the other exiting the detector, MicroBooNE is still explicitly able to distinguish an electron from a gamma using dE/dx information. While an electron will deposit about 1 MIP [1] of energy in the first few cm of its track, a γ will deposit 2 MIPs, due

[1] A "MIP" is a unit of energy that is defined as the amount of energy deposited by a minimum

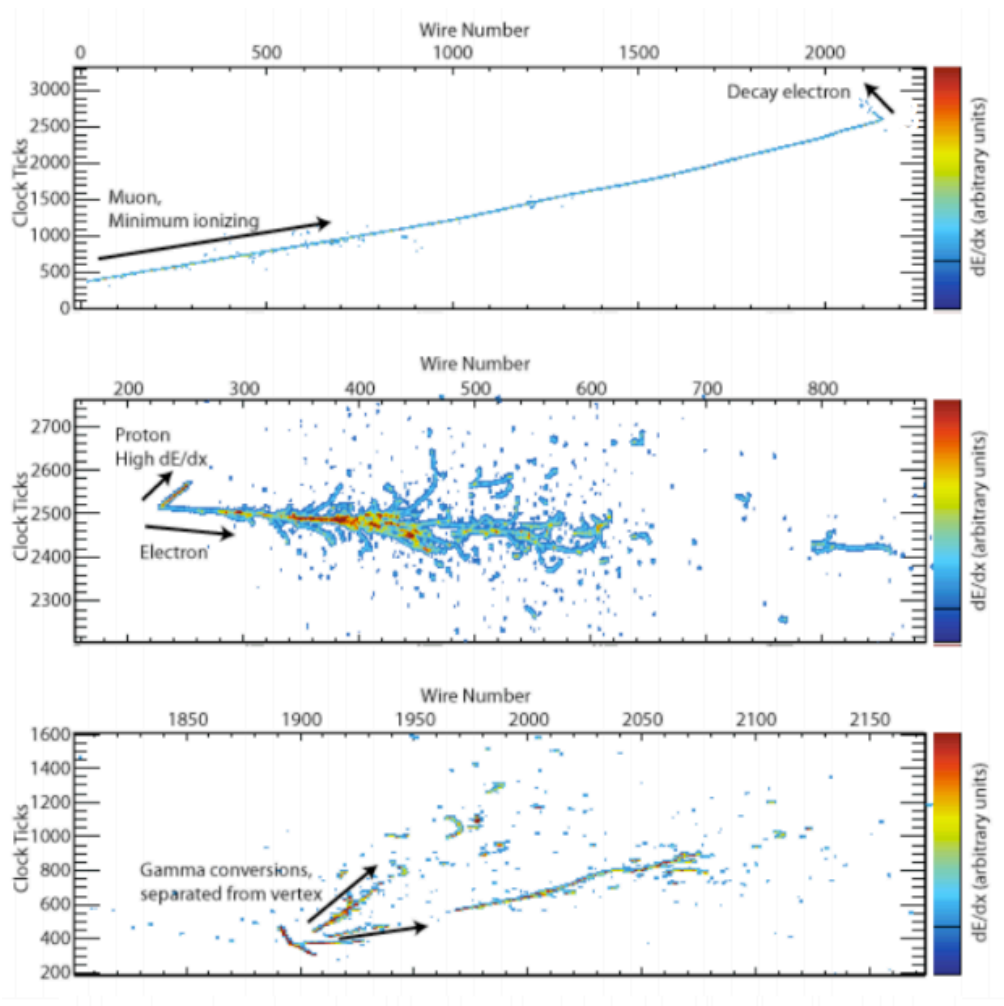

Figure 6-3: A muon (top), electron (middle), and π^0 (bottom) event in the MicroBooNE detector, using information from one of the three wire planes. Information from all three wire planes can be used in combination with timing information to produce a 3D reconstruction of tracks (not shown).

to the initial $\gamma \to e^+e^-$. The capability of MicroBooNE to separate electrons from photons is shown in Figure 6-4.

Because of this excellent e-γ separation, MicroBooNE will be able to separate excess photons above a photon-like background from excess electrons above an electron-like background. While the result may end up being a mixture of these two cases, the cases where the excess is due to either only photons or only electrons are shown in Figure 6-5.

---

ionizing particle

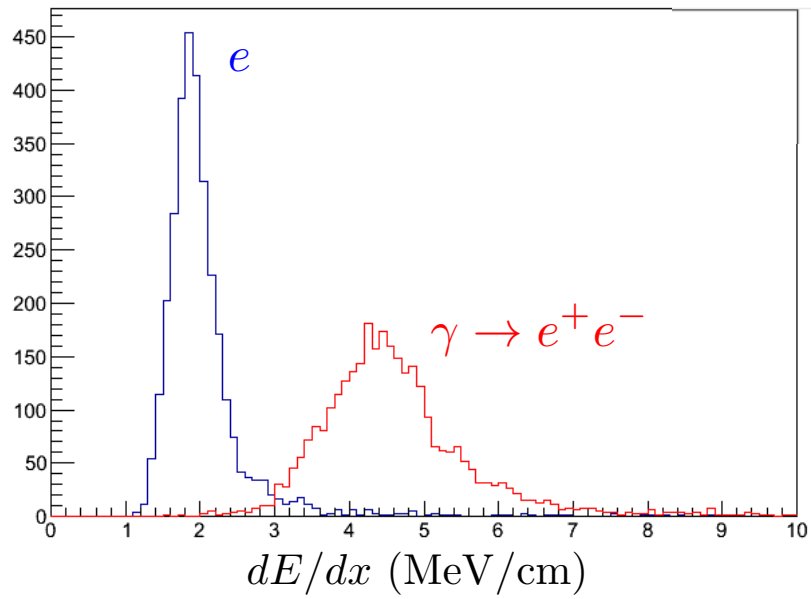

Figure 6-4: Energy loss for 0.5 - 5 MeV electrons and photons. The electrons are easily separated from the gammas, allowing for rejection of the photon-induced backgrounds that affected MiniBooNE. From Reference [122].

6.3 MicroBooNE Light Collection System

The light collection system serves several purposes. First, the "fast" scintillation light (∼6 ns for the fast light vs ∼1.6 μs for the slow light) provides a t_0 within a few nanometers. Both the time structure of the beam and the drift time of ionization electrons are on the order of a microsecond. For this reason, although most neutrino events can be successfully linked with a beam pulse, there is uncertainty between exactly when the event occurred and exactly where it occurred. This information is provided by the light collection system and is important since drift-distance-dependent effects must be accounted for. These include charge loss due to electron absorption, dispersion, and space charge effects.

The exact t_0 also assists in background rejection for the case where background events from external sources overlap with the beam window. This is especially important for a surface detector like MicroBooNE, where the cosmic ray rate is expected to be ∼5 kHz. Comparing optical data with TPC data can also prevent accidental trigger by TPC noise. In addition, the t_0 from the PMT system is the only mechanism of triggering on non-beam events and determining the location of their vertices.

In addition to trigger-related benefits, light information may be used for particle ID. The ratio of the fast-to-slow scintillation light (see Section 6.3.1) is dependent on the dE/dx of the ionizing particle, as the slow component is quenched more significantly than the fast light for a higher dE/dx. The feasibility of being able to extract and use this information is still being explored.

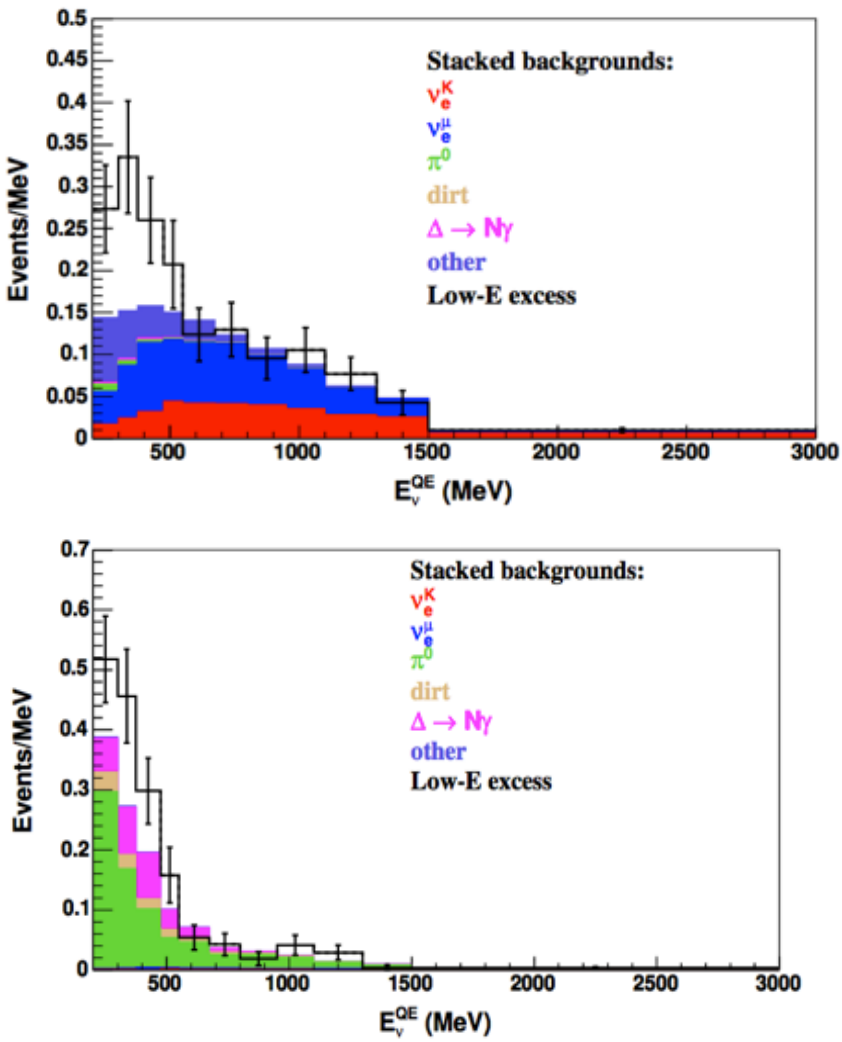

Figure 6-5: Top: A simulated signal over photon-like backgrounds. This assumes that all of the events as seen in MiniBooNE are photon-like. In this case there would be no observed signal above electron-like backgrounds. Bottom: A simulated signal over electron-like backgrounds. This is the opposite case to the top plot, assuming that all of the MiniBooNE low-energy excess events are electron-like (meaning there would be no signal over photon backgrounds).

6.3.1 Scintillation Light in Liquid Argon

Scintillation light is produced in liquid argon through two processes: [123, 124, 125]:

Self-trapped exciton luminescence occurs as a charged particle travels through the LAr and excites the argon atoms in its path. When this occurs, the excited argon atom may combine with another argon atom, in a process called "self-trapping". This results in the formation of an excimer, which consists of Ar_2^+ with a bound electron. The excimer will then radiatively decay to form two argon atoms and a 128 nm photon.

Recombination luminescence begins with a charged particle traveling through the LAr ionizing argon atoms. This is the same process by which the ionization electrons are produced. The resulting argon ion from this process can recombine with another argon atom and another electron to produce the excimer described in the previous process. As before, this excimer then decays into two argon atoms and a 128 nm photon. The rate of this process varies with the electric field since the field has the ability to remove electrons from within the range of the ionized argon atoms. It also depends on the dE/dx of the particle, as a higher dE/dx increases the density of electrons and therefore the probability of recombination.

The excimer that results from both of these processes forms a Rydberg state, so the spins of the electron and the Ar_2^+ can exist in a singlet or triplet state. The singlet state decays with a time constant of 6 ns and is known as "fast," or "prompt" scintillation light. The triplet state has a time constant of 1.5 μs and is known as "slow," or "late" scintillation light. There is not a one-to-one correspondence between self-trapped exciton luminescence and recombination luminescence with the singlet *vs.* triplet states, with the former being made up of about a third fast light and two-thirds slow light and the latter consisting of about half fast light and half slow light. The ratio of self-trapped exciton luminescence to recombination luminescence is dependent on the dE/dx of the charged particle (as described above). Studies are underway to determine whether this ratio can be used to assist with particle ID.

The 128 nm scintillation light produced by these processes is in the "vacuum UV," a range of wavelengths which is unable to pass through most substances, including air. This 128 nm light is unable to pass through any material that can be used in the fabrication of photomultiplier tube glass, and therefore must be shifted to a wavelength that can be detected. The wavelength-shifting material that we used for MicroBooNE is called Tetraphenyl Butadiene (TPB), and is further discussed in Section 6.4. The opacity of most materials to 128 nm light also leads to purity considerations in addition to those necessary for optimal functioning of the TPC. Our main concern in this regard is nitrogen contamination, as oxygen is already strictly limited for TPC functioning. Studies of the effects of nitrogen contamination on scintillation yields are discussed in detail in Reference [126]. The specification for nitrogen contamination in MicroBooNE will be 2 ppm, which was measured to yield an absorption length of 30 $\pm$ 3 m for argon scintillation light, meaning that nitrogen

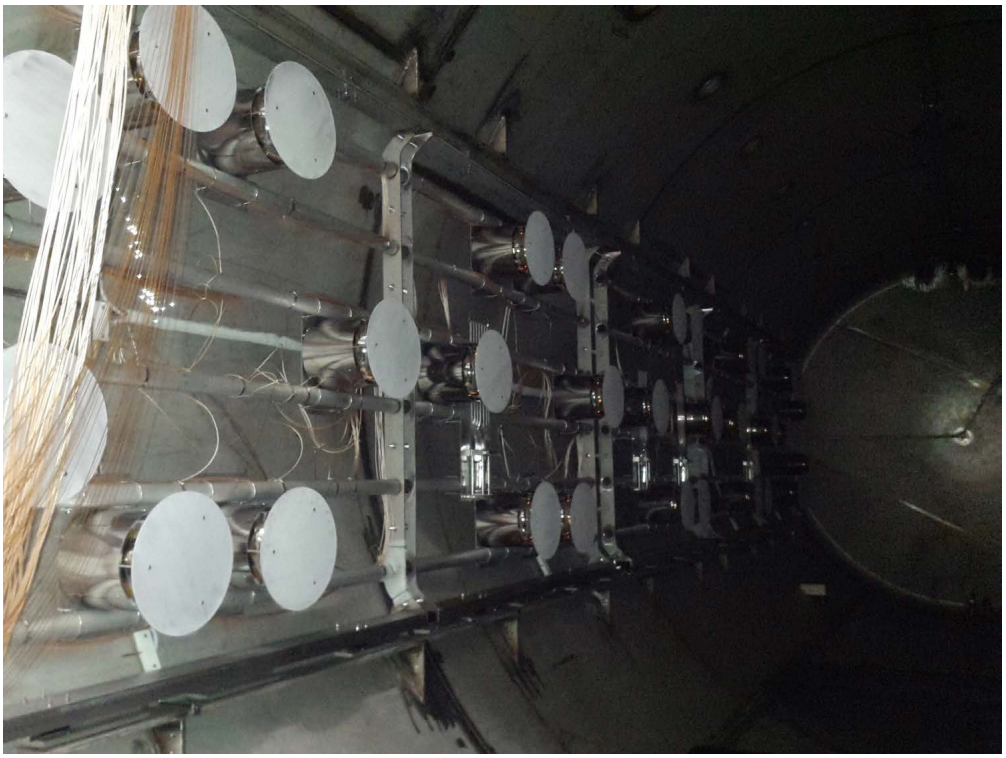

Figure 6-6: The PMT units including TPB coated plates mounted on the PMT rack in the MicroBooNE cryostat (before the TPC was installed).

contamination will not be an issue for us. These effects have been incorporated into the optical Monte Carlo.

6.3.2 PMT System Design

MicroBooNE uses 32 Hamamatsu R5912-02mod 8" cryogenic PMTs to detect the argon scintillation light. This PMT model has 14 stages, an average operating voltage of ∼1700 V, and a gain on the order of 10^9. It contains a platinum undercoating to allow the bi-alkali photocathode to maintain its conductance at LAr temperatures. The PMTs are arranged on a rack that slides into the cryostat behind the wire planes, providing 0.9% photocathode coverage. Figure 6-6 shows PMTs sitting on the rack in the cryostat.

Each PMT unit consists of a PMT inside of a mount contained within a magnetic shield. A 12" diameter TPB-coated plate is located directly in front of the PMT. Figure 6-7 shows a schematic of the PMT mount and a photo of a PMT unit. The PMT is held in place by an aluminum ring with teflon spacers and a teflon-coated wire attached to an aluminum ring by spring loaded wires. This allows for a secure fit without the risk of the mount being too tight, which can cause implosion. The magnetic shield prevents interference from the Earth's magnetic field, which deflects electrons traveling along the dynode chain within the PMT. Without the shields, we

have observed a difference in PMT response with various orientations with respect to the earth's field, and have demonstrated the absence of this effect with the shields in place [127].

6.4 TPB Wavelength-Shifting Coating

A wavelength-shifting material called Tetraphenyl Butadiene (TPB) is used to detect the 128 nm argon scintillation light (to which the glass of a PMT is opaque). The TPB spectrum for an evaporative coating (Section 6.4.1) peaks at 425 nm, and can be seen in Figure 6-8. We use a mixture that consists of 50% TPB and 50% polystyrene (PS) and deposit it onto 12" plates placed directly in front of the PMTs.

The efficiency of a 1.5 μm thick evaporative TPB coating (Section 6.4.1) has been measured to be 120% at 128 nm by Reference [128]. We find that the 50% TPB-PS chemical coating chosen for MicroBooNE is more robust and less expensive than the evaporative coatings we have studied, and has a total efficiency of about $70 - 80\%$.

6.4.1 Types of TPB Coatings in MicroBooNE and Other Experiments

TPB is usually applied to PMTs or plates by evaporative or chemical coatings. Evaporative coatings yield the highest efficiency but are the most fragile, as loose TPB may brush off during handling. Chemical coatings use a solvent, usually toluene, to dissolve the TPB and a plastic such as polystyrene. The mixture is painted onto a surface and the toluene is allowed to evaporate, forming a coating consisting of TPB embedded in plastic which is left behind. The surface and coating must have similar coefficients of expansion to prevent crazing at cryogenic temperatures. This leads to a more robust but less efficient coating. Details on the different coatings are described below.

Evaporative coatings

Evaporative coatings yield the highest conversion efficiency and are used in experiments such as WArP [129] and MiniCLEAN [130]. They are created by evaporating TPB onto a surface in a vacuum chamber, producing a coating with a powdery white appearance. The absolute efficiency of 1.5 μm thick evaporative TPB coatings has been measured as a function of wavelength by Reference [128]. The evaporative samples used for the measurements in this thesis have a thickness of 1.87 μm.

TPB in Polystyrene (PS25%)

TPB and polystyrene are dissolved in toluene in a ratio of 3:1 PS to TPB by mass, and a ratio of 1 g PS per 50 ml of toluene. The mixture is brushed onto acrylic where the toluene is allowed to evaporate, producing a clear film of TPB in PS. This coating was used in Reference [38] for use in TPB-coated lightguide systems (See Section 7.3).

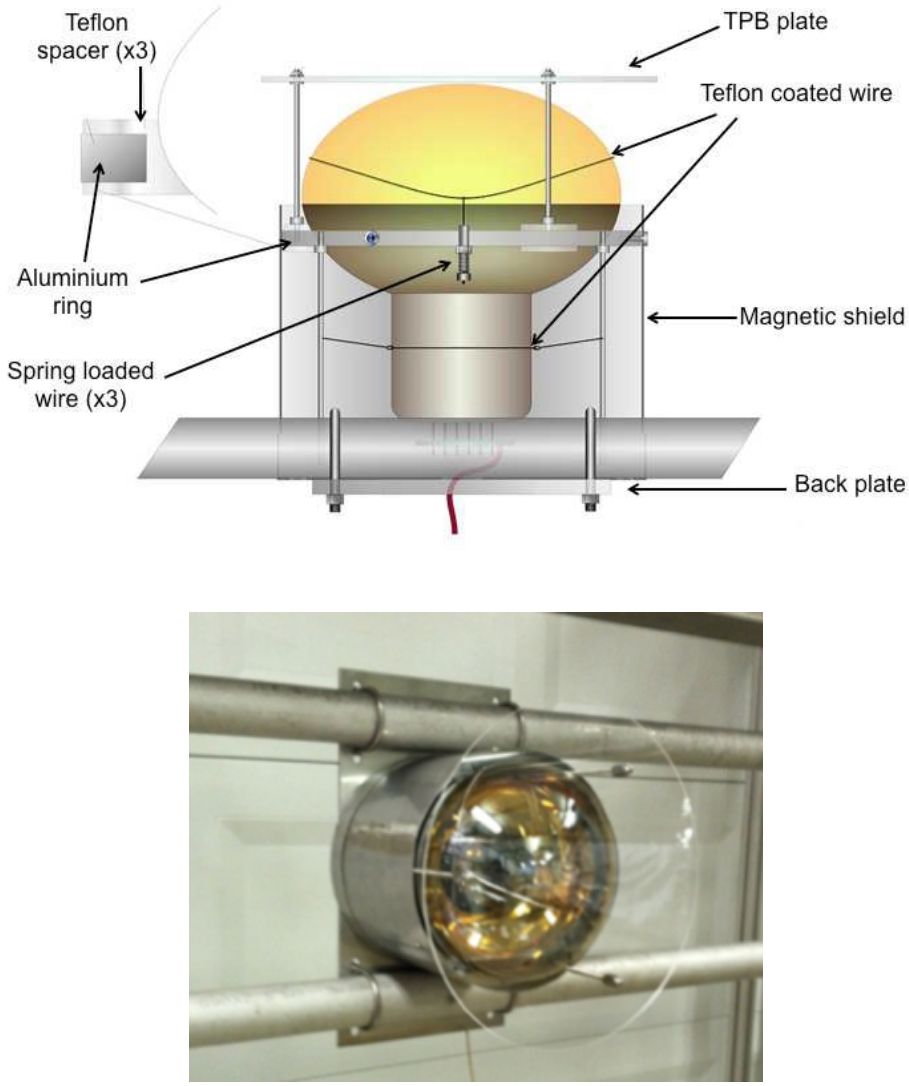

Figure 6-7: Top: A schematic of a PMT unit which includes the components of the mount, the magnetic shield, the wavelength-shifting plate, and the PMT. Bottom: A photograph of the unit with an uncoated plate.

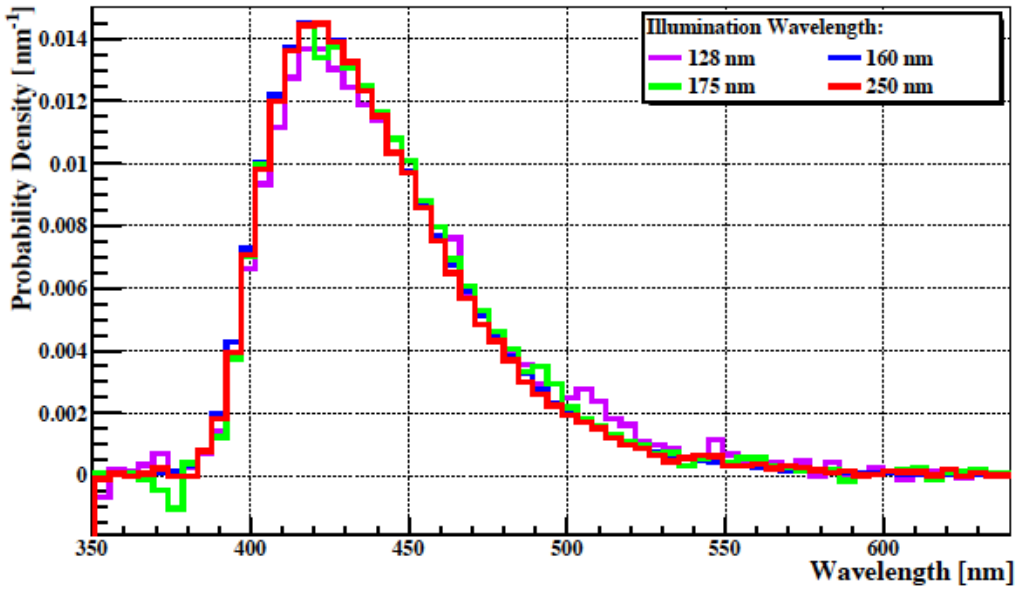

Figure 6-8: The TPB emission spectrum from an evaporative coating for a variety of different incident wavelengths. The measurement was taken in a vacuum monochrometer by Reference [128].

TPB in Polystyrene (PS50%)

TPB and polystyrene are dissolved in toluene in a ratio of 1:1 by mass and a ratio of 1 g PS per 50 ml of toluene. This amount of TPB over-saturates the PS and crystalizes out of solution onto the surface of the PS, leading to a higher efficiency than PS25% or UVT33%. This type of coating is more robust and less expensive than evaporative coatings and is used in the MicroBooNE experiment [117] (Figure 6-9). The mixture is applied, using a paintbrush, in three coats, with the small particles of TPB from the previous coat becoming dislodged and contributing to the surface layer of TPB. A small amount of ethanol is added, preventing large TPB crystals from forming. It is added at the time of the application of the coating, as opposed to in advance, to prevent interaction between the ethanol and the rest of the solution. The TPB crystals are held firmly in place by the PS.

TPB in Acrylic (UVT33%)

This coating is similar to PS25% except that UV transmitting acrylic is used in place of the PS. UVT acrylic has a higher saturation point of TPB, enabling a ratio of 2:1 UVT acrylic to TPB by mass. Like the previous coatings, the ratio of UVT acrylic to toluene is 1 g UVT acrylic per 50 ml of toluene. This is the primary coating studied in [37] for use in TPB-coated lightguide systems. This coating has replaced the PS25% coating in our lightguide studies due to the closer index of refraction match to the

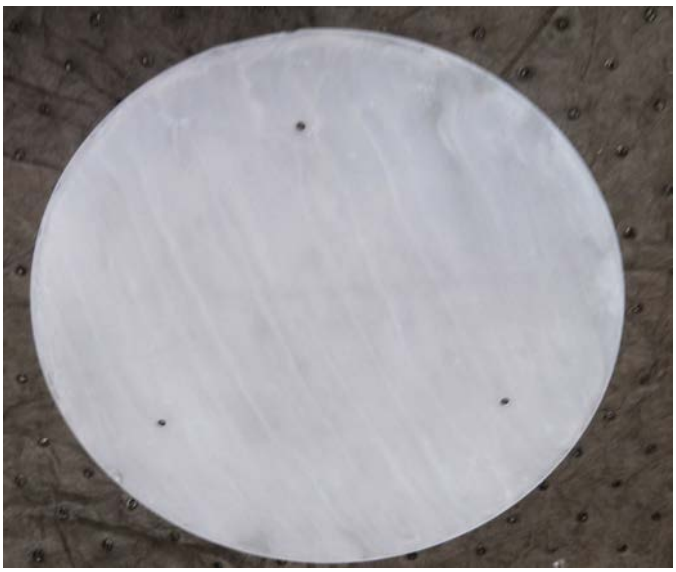

Figure 6-9: A photograph of one of the MicroBooNE TPB coated plates immediately after it was coated. Streaking is visible due to the brushing method of application, but does not affect the uniformity of the plate's response.

bulk acrylic. The higher index of refraction of the PS25% caused some of the light to become trapped in the coating rather than the bulk acrylic as intended, dissipating the light much more quickly (see Section 7.3).

6.4.2 Comparing TPB Coatings

The relative efficiencies of TPB coatings were tested in a McPherson 234 vacuum monochrometer at wavelengths between 128 nm and 250 nm and also in LAr at 128 nm. The setup and results of these tests are described in this section.

Coating Samples

Samples were made by applying the different coatings of Section 6.4.1 to a 4" x 4" square pieces of acrylic. Three such pieces were created for each coating type. Each piece was then cut into several 1.5" $\times$ 1.5" squares, as that is the maximum size allowable by the vacuum monochrometer test setup. The 1.5" $\times$ 1.5" squares can not be coated directly using our method of coating, as adequate surface area is needed to brush the solution onto the samples evenly.

The efficiency of samples of the same coating-type that were cut from the same initial square were statistically indistinguishable from those that did not come from the same initial square. For this reason, each 1.5" $\times$ 1.5" square samples is treated independently.

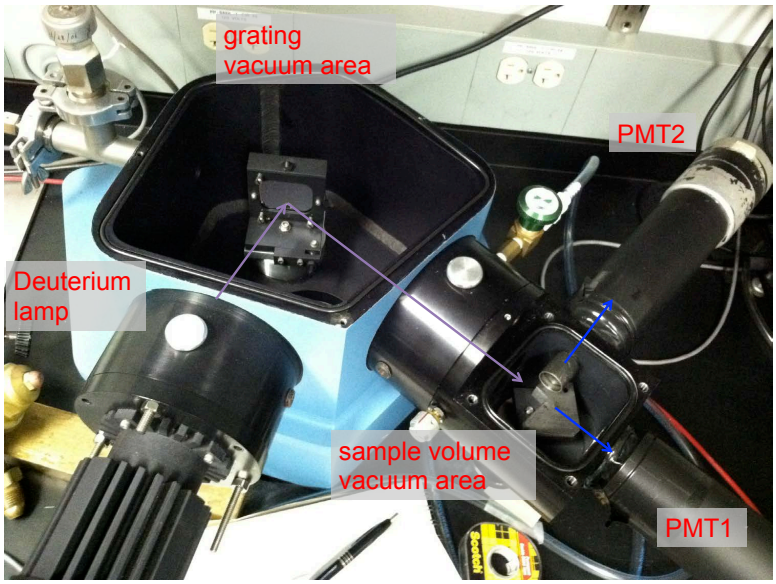

Figure 6-10: Setup for the vacuum monochromator measurement. Light from the deuterium lamp enters a vacuum grating area where a specific wavelength can be selected by the grating to impinge on a sample. For this study, the emission from the sample is observed by PMT1.

Vacuum Monochrometer Test Setup

The vacuum setup is shown in Figure 6-10 and consists of light from a McPherson model 632 UV deuterium lamp impinging on a grating which isolates a particular wavelength to send into the sample chamber. The deuterium lamp spectrum can be seen in Figure 6-11. A PMT is located outside of the vacuum region on the opposite side of the sample to detect the light after it has been shifted and has passed through the coating. The measurements were taken at a pressure of $\sim$ 10 mTorr. Data was taken by measuring the number of pulses that passed a discriminator threshold of 30 mV in 10 s. A variety of wavelengths between 128 nm and 250 nm was tested for each of the samples.

Liquid Argon Test Setup

The liquid argon measurements were made using a ^{210}Po alpha source which produces 128 nm light via argon scintillation. During testing, the source is located directly in front of the sample with a Hamamatsu R7725mod 2-inch PMT directly behind the sample. The setup can be seen in Figure 6-12. The sample-holder consists of two stainless-steel plates held together with set-screws which are tightened after the sample is inserted, wedging it in place. The metal plates each contains 1" diameter holes to allow the incident and emitted light to pass through. The plate holder was designed to be sufficiently long to allow it to be removed without removing the PMT

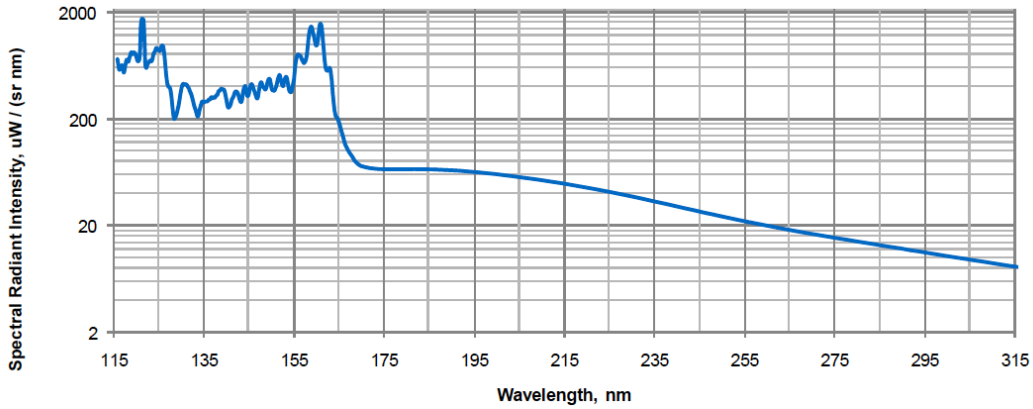

Figure 6-11: The spectrum from a McPherson model 632 vacuum UV deuterium source [131].

from the argon.

The PMT sits horizontally within a 11" diameter stainless steel dewar. The alpha source is fixed within a 4.5" metal disk, secured to the mount of the PMT. The metal disk contains a slot that allowed the sample holder to fit snugly. This ensures that the relative positions of the PMT, sample, and alpha source are fixed for each measurement.

These tests were done using an open-air test stand using "Industrial Grade" liquid argon purchased from Airgas [132]. This grade of argon is not sufficient for any absolute-efficiency measurements of the samples, but it is sufficient as a mechanism for 128 nm scintillation light production. This allows us to perform relative measurements of different coatings using the correct wavelength and temperature. Due to the open-air nature of the dewar, if the argon is poured through the air it becomes contaminated with nitrogen [126]. For this reason, the filling procedure requires first allowing argon gas to displace the air from the inside of the dewar. LAr is then allowed to enter the dewar from a height just above the LAr level. This filling procedure leads to argon of sufficiently repeatable purity immediately after filling. Measurements of a reference sample after multiple repeats of this procedure yielded consistent results.

If left for a period of time, however, the argon within the open dewar will become contaminated over time, with the reference light output decreasing at a rate of about 0.2% per hour if left undisturbed. Pulling samples in and out during the course of measurements may further increase this rate to as high as a few percent per hour. For this reason, a reference sample was tested frequently and the rest of the measurements were adjusted accordingly. Measurements relative to the reference sample were consistent among different batches of argon and different amounts of argon contamination.

Data is acquired using an Alazar Tech ATS9870 digitizer. An example pulse can be seen in Figure 6-13. Pulses are integrated from 20 ns before the trigger to 40

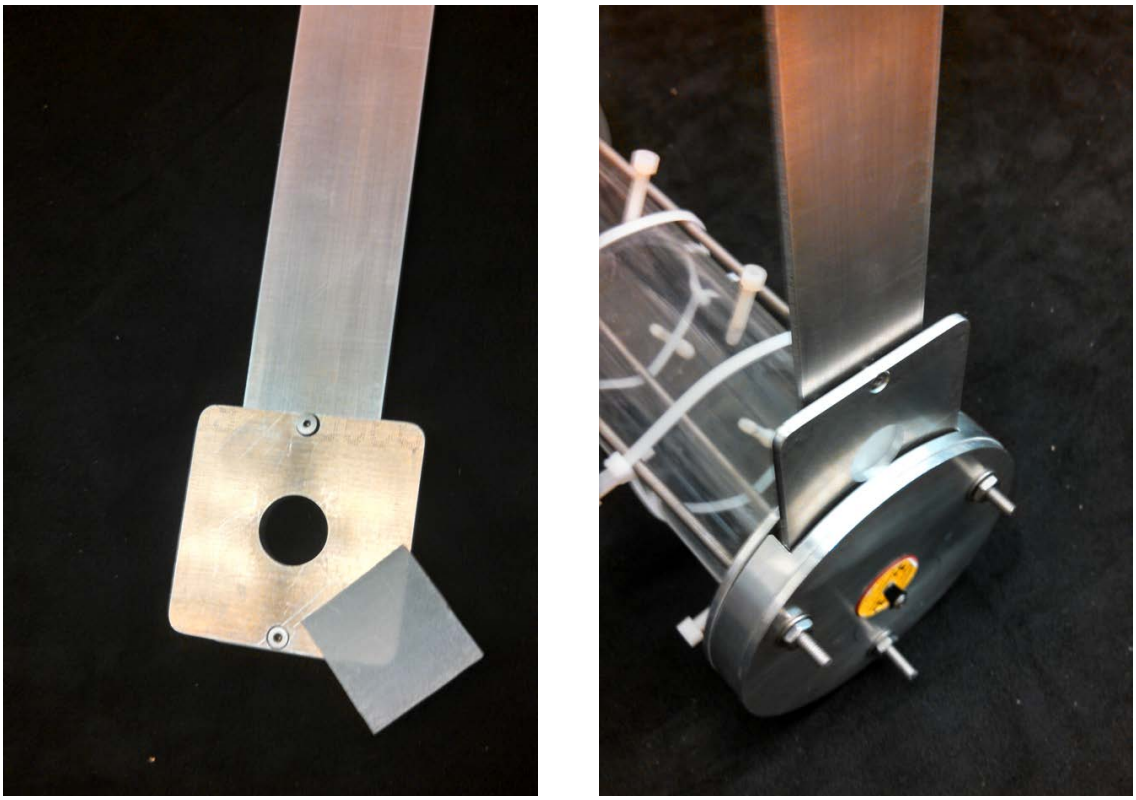

Figure 6-12: Left: The plate holder described in the text and a 1.5" × 1.5" sample coated with a PS50% coating. Right: The PMT mount (without a PMT). The PMT holder is being inserted into the slot on the mount, where the plate will line up with the alpha source and PMT window. The alpha source is within the yellow disk at the center of the metal plate, and the disk is secured in place. The PMT remains in the dewar submerged in LAr as samples are inserted and removed for testing.

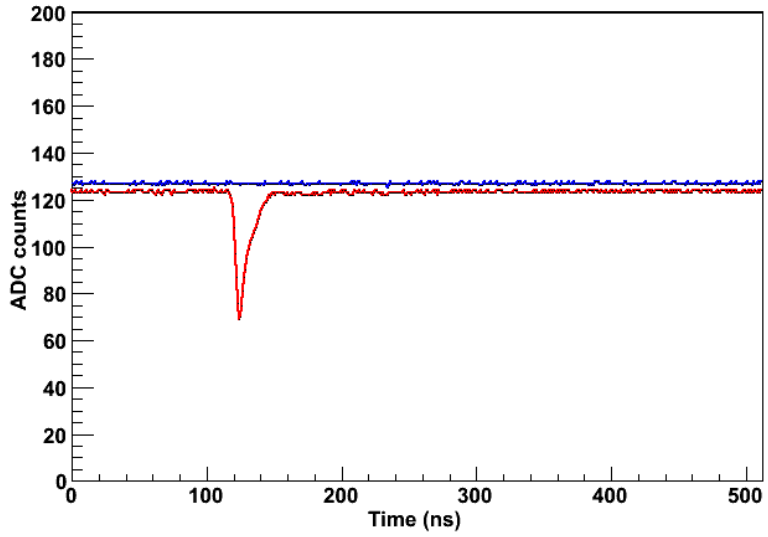

Figure 6-13: An example waveform acquired by the Alazar Tech ATS9870 digitizer.

ns after the trigger (100 ns to 160 ns in Figure 6-13). Note that this analysis uses different digitizer settings than those described in Section 7.3 and so the the y-axis does not correspond to the same voltage as the pulses shown in that section. No late light is visible in Figure 6-13 because the late light pulses are too small to see on this scale.

Results Coating Comparison Studies

The results of both the vacuum studies and the LAr studies are shown in Figure 6-14. For the vacuum measurements, samples are normalized to the evaporative coating measurement to remove the spectrum of the deuterium lamp. Error bars on the bottom three lines only take into account the errors associated with those measurements, allowing for comparison amongst the samples, while error bars on the evaporative sample illustrate errors on the evaporative measurement (which also affect the ratio values of the other points).

The liquid argon measurements are shown in the same plot to the left of the 128 nm vacuum point. These measurements are also normalized to an evaporative coated sample to compare to the vacuum results. Because of this, deviations within errors of either set of evaporative measurements would cause the other samples to shift. This effect must be taking into account when comparing the results. Taking this into account, one can see that the datasets in vacuum and argon are in good agreement.

We have previously seen visible mechanical degradation of evaporative coatings due to the violent boiling of the argon around the sample during submersion. This may account for the the sample-to-evaporative ratios in LAr being high relative to the vacuum measurements. The vacuum measurements were taken using evaporative samples that had never been exposed to LAr. All samples from these studies were carefully stored in a dark environment to mitigate the damaging effects of light (Section 6.4.3).

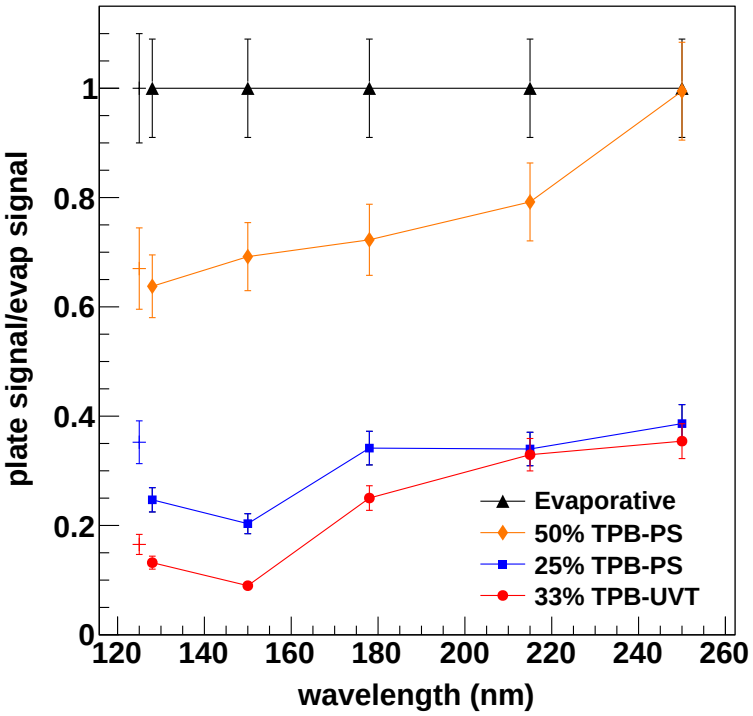

Figure 6-14: **Connected points:** Coating efficiency measured in a vacuum monochrometer as a function of wavelength normalized to measurements of evaporative samples. **Left-most points:** Tests in LAr using an alpha source which are at 128 nm and over-plotted onto the vacuum measurements for comparison to the 128 nm vacuum point. Errors on the evaporative samples must also be taken into account when comparing LAr with vacuum for a particular coating, but not when comparing one type of coating with another in the same medium.

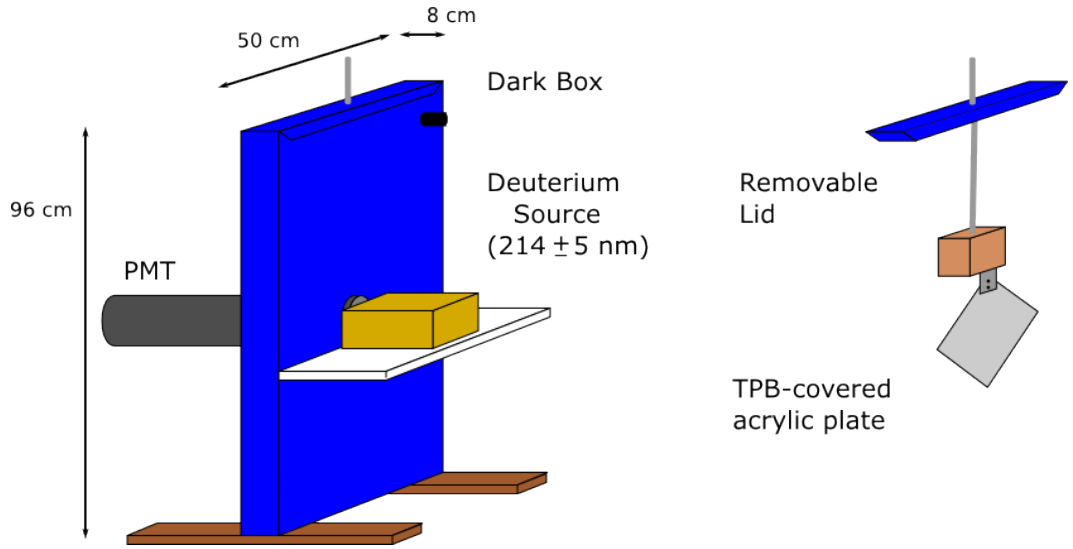

Figure 6-15: The test setup for the TPB degradation studies. From Reference [39].

6.4.3 TPB Degradation

During the process of developing coatings for MicroBooNE, we discovered that TPB suffers substantial degradation when exposed to UV light [39, 133]. A preliminary study attempting to determine the source of the degradation explored both humidity and light, as we expected humidity to have an effect due to reports from Reference [134]. While we did not see any difference between plates placed in an ordinary dark box *vs.* a humidity-controlled box, we saw significant effects from exposure to light. In an effort to better understand this effect, we performed a controlled study comparing plates under different conditions. The results of this study are reported in this section.

Measurements were taken using a StellarNet SL3-Cal deuterium source with a 215 nm bandpass filter. Samples were placed in a tall, thin dark-box with light from the deuterium source impinging on the sample and a PMT collecting light emitted from the other side. The setup can be seen in Figure 6-15. The samples consisted of 4" × 4" square acrylic plates coated with a MicroBooNE-style TPB coating (Section 6.4.1).

We measured the samples in air, hence the use of 215 nm light, as light under 200 nm is absorbed by the air. All measurements were compared to a reference sample (which had previously degraded enough such that the degradation had leveled off) to account for variations in the output of the deuterium source over time. The results of this study can be seen in Figure 6-16. We observe a drop of about 30% after just one day of exposure to ambient light in the lab.

We have determined the degradation to be primarily caused by the sunlight coming in through the windows rather than the fluorescent lights in the lab. A followup study seeking to isolate the wavelength responsible for the degradation showed UV light to be the main culprit [39]. Further studies showed that UV-blocking films are somewhat effective at preventing the degradation. Samples placed under fluorescent light (and

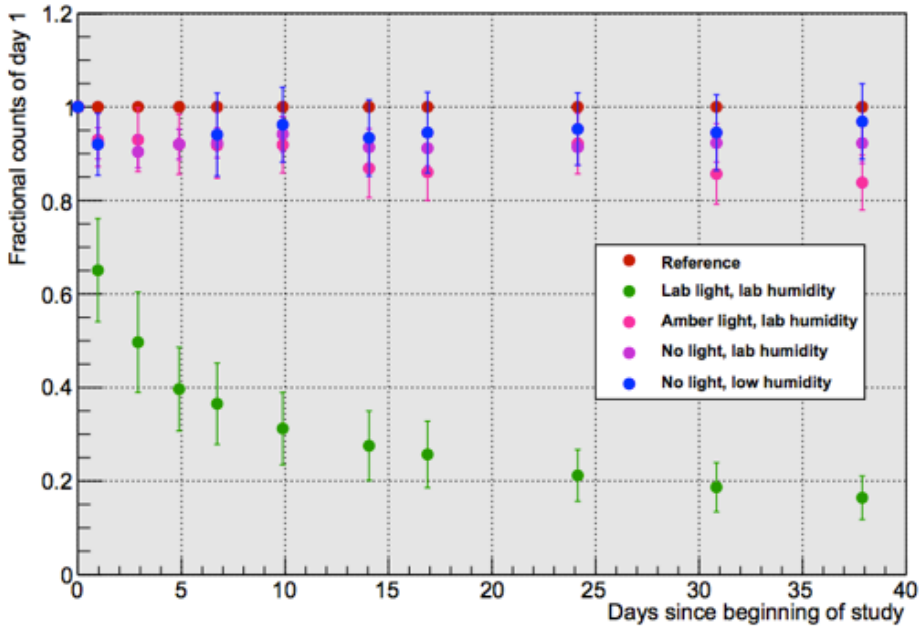

Figure 6-16: The results of the TPB degradation study on PS50% plate samples. The points are normalized to a reference sample and to their initial measurement directly after they were coated, and so all start at 1.0. We see substantial degradation of samples left out in the lab under normal light conditions but do not see an effect due to humidity and only a minimal effect on samples left under an amber light filter.

isolated from sunlight) degraded by 14% after three days, compared with 4% after fitting the bulbs with UV blocker. Plates left in direct sunlight degrade by about 50% after only 3.5 hours, and by 14% with filtered sunlight.

6.4.4 MicroBooNE Plate Production and Deployment

Production of the MicroBooNE plates proceeded in Lab 6 at Fermilab under a fume hood. The TPB-PS-toluene solution was made as described in Section 6.4.1, and an ultrasonic bath was used to expedite dissolving the TPB and PS in solution. Each of the three coatings used about 70 ml of solution, with 8 ml of ethanol applied with the solution. The coating is spread evenly across the plate with a large round paintbrush and allowed to dry before the addition of the next coating. Subsequent coatings require pressure to partially dissolve the previous layer to generate more TPB on the surface. Each 12" diameter plate uses approximately 4 g of TPB, though some of this is lost to the brush.

The degradation effects of Section 6.4.3 were considered during this process. The plates were made in a windowless environment and immediately individually wrapped and placed in a dark box, where they remained until installation. Installation proceeded under blocked lights and as late in the installation process as possible.

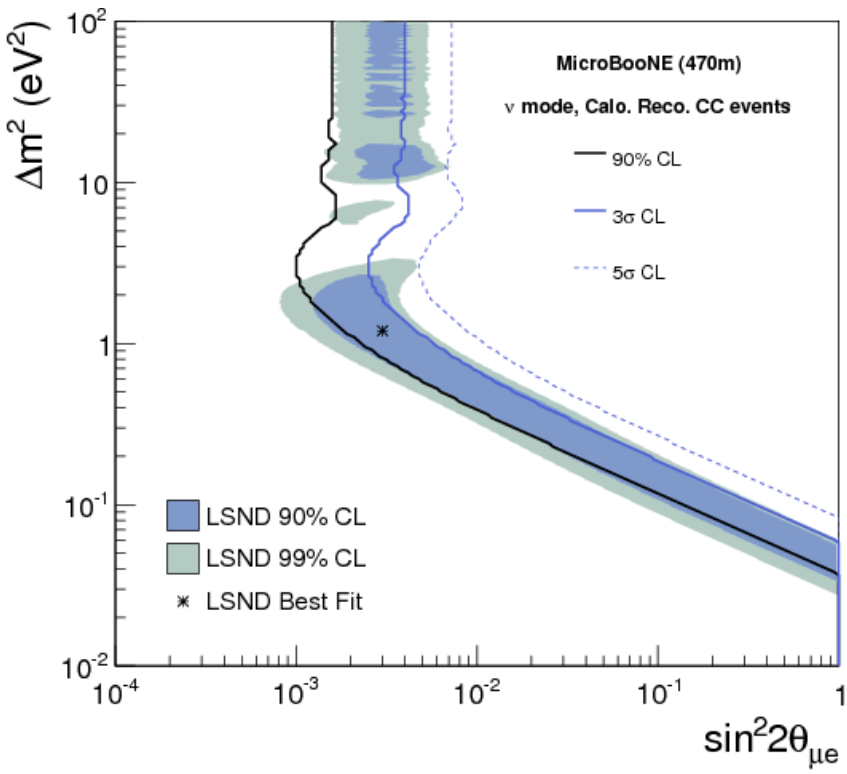

Figure 6-17: The sensitivity expected by the MicroBooNE experiment from a run of 6.6×10^{20} protons on target in neutrino mode for a search for ν_e appearance.

6.5 MicroBooNE Physics Goals

The primary physics goal of MicroBooNE is to explore the MiniBooNE low-energy excess, which can be achieved as described in Section 6.2.1. The sensitivity to the sterile neutrino oscillation parameters in a $3+1$ ν_e appearance search is shown in Figure 6-17 assuming 20% systematic uncertainties on ν_e backgrounds.

MicroBooNE also has sensitivity to perform a disappearance analysis (Figure 6-18). The predicted sensitivity is comparable to the MiniBooNE + SciBooNE joint disappearance analysis (Reference [113]).

MicroBooNE can also make important cross section measurements, sensitive to the same energy regime as MiniBooNE (Figure 3-4) since it uses the same beam.

Future LAr detectors can also play an important role in supernova neutrino studies as well as proton decay searches. To that end, MicroBooNE will study backgrounds and develop analysis tools for these future searches.

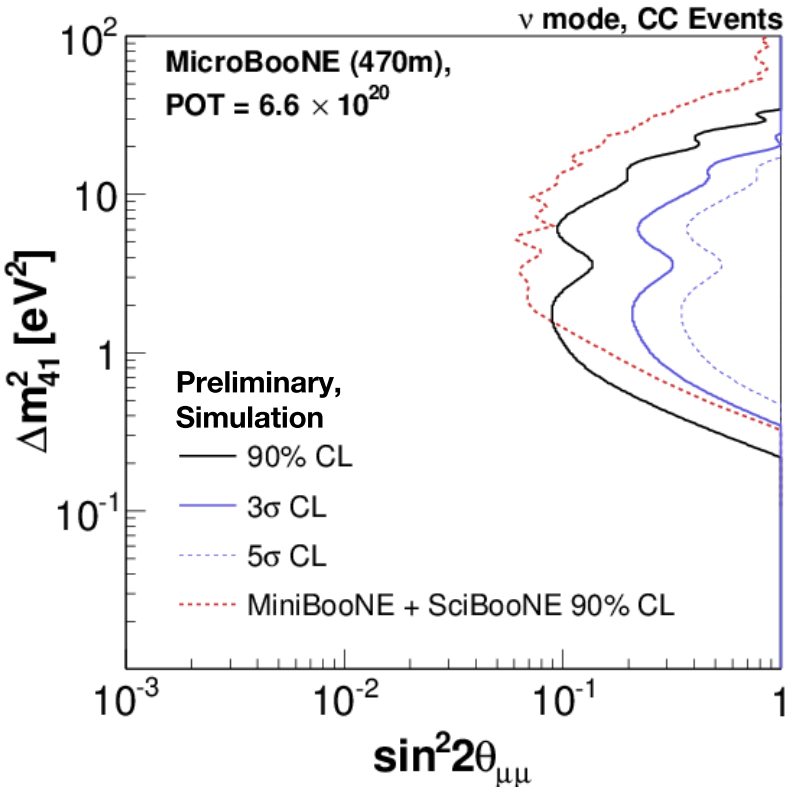

Figure 6-18: The sensitivity expected by the MicroBooNE experiment for a ν_μ disappearance analysis. Overlaid is the 90% CL interval from the MiniBooNE + SciBooNE analysis. From Reference [135].

Chapter 7

Other Current and Future LArTPCs

LArTPCs are planned to play a large role in the next generation of particle physics measurements. These include the most important areas of research for the next few decades (Section 1.3) including the determination of the neutrino mass hierarchy, the measurement of δ_{CP} (and therefore the answer to whether CP is violated in the neutrino sector), and the detection of a supernova within our galaxy.

7.1 Previous and Current Experiments

So far, there have been two major LArTPC neutrino experiments that predate MicroBooNE: ICARUS [119] and ArgoNeuT [118].

ICARUS is the pioneering neutrino physics experiment to utilize LArTPC technology [119]. It consists of 600 tons of LAr and is located at a baseline of 732 km from the "CERN Neutrinos to Gran Sasso" (CNGS) beam with a neutrino mean-energy of 17 GeV. ICARUS consists of two TPC modules, each containing two sets of TPC wires on either side with the Cathode in the center. Ionization electrons drift, a maximum of 1.5 m, to the closer set of wires due to a uniform 500 V/cm electric field. ICARUS contains ∼53,000 wires divided into 3 planes (horizontal and ± 60 degrees) with 3 mm separation. The light collection system consists of 74 8" PMTs sandblasted and sprayed with a solution of TPB and toluene located behind the wire planes. ICARUS has been taking data since 2010 and has made important contributions to neutrino physics as well as LArTPC technology.

ArgoNeuT was located in the NuMI beamline at Fermilab in the MINOS near-detector hall. The primary physics goal was to measure ν and $\bar{\nu}$ CCQE cross-sections on argon. It was also the first step in a U.S. LArTPC program with an eventual goal to actualize kiloton-scale detectors [118]. ArgoNeuT contained an active volume of 175 liters of LAr and studied neutrinos with energies between 0.1 and 10 GeV.

ArgoNeuT encompasses ∼500 wires in two planes with a 4 mm separation and ± 60 degree orientation. Like ICARUS, it uses a 500 V/cm electric field, but did not utilize a light collection system. ArgoNeuT took data from 2009-2010 and has now been disassembled, having made important contributions to LArTPC instrumentation technology and CCQE cross-section measurements [136]. ArgoNeuT also made additional physics measurements, such as in Reference [137].

7.2 Future Experiments

The major experiments planned in the US LArTPC program are described in this section:

LArIAT, "Liquid Argon In A Test-beam" [138] will be located at Fermilab within a charged particle test beam. Phase one will reuse the ArgoNeuT cryostat for further studies using charged particles within the 200 MeV - 2 GeV range. It will measure charge recombination along particle tracks and perform particle-ID optimizations, measurements, and calibrations. LArIAT will make direct measurements, using fully contained particle tracks, of collected charge to incident particle energy. The second phase of LArIAt will use a larger detector, with a design based in part on information learned from phase 1. It will be able to contain higher energy particle tracks and showers than phase 1, and can measure charge to energy conversion for larger events.

CAPTAIN, or the "Cryogenic Apparatus for Precision Tests of Argon Interactions with Neutrinos," [139] will contain 5 tons of liquid argon. It will first study neutrons at the Los Alamos Neutron Science Center (LANSCE), and is designed to be portable. After LANSCE, it will run in one or more of a number of possible neutrino beams including NuMI at Fermilab or SNS at ORNL.

LAr1-ND will serve as a near detector for multiple neutrino detectors, including MicroBooNE as well as possible future detectors. It will be located in the existing SciBooNE hall at a baseline of 100 m from the Booster Neutrino Beam. It will contain a fiducial volume of 40 tons of LAr and will utilize systems specifically designed toward developmental possibilities for LBNF. LAr1-ND as a near detector to MicroBooNE will also extend the reach of the sterile neutrino search, as it would be able to confirm the nature of any observed excess. The proposed 1 kiloton LAr1 [140] would have served as the primary detector, but it did not receive a favorable report from the recent Particle Physics Project Prioritization Panel (P5) report [141]. Therefore, it is less likely to move forward than LAr-ND alone.

LBNF, the "Long Baseline Neutrino Facility," formally LBNE, the "Long Baseline Neutrino Experiment" was originally designed to be a 35 kton fiducial volume LArTPC with a primary physics goal of measuring CP violation. It will also attempt to measure the neutrino mass hierarchy and perform other long-baseline

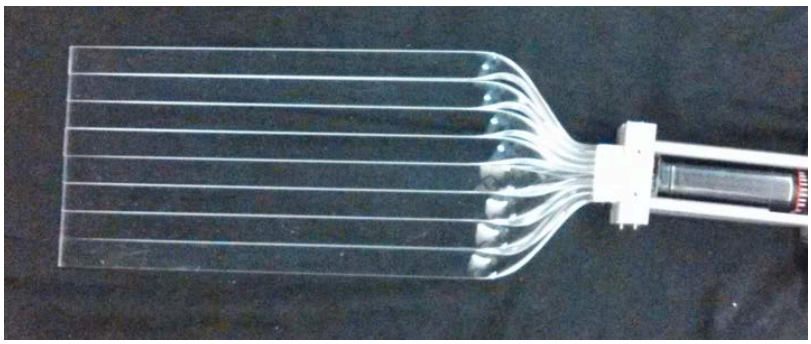

Figure 7-1: A photograph of a collection of lightguide bars adiabatically bent to form a paddle. The bars transmit light to the curved ends where the light is detected by a 2" PMT.

neutrino physics [21]. It was planned to be located at a depth of about 5,000 at the Sanford Underground Research Facility "SURF" with a baseline of 1300 km neutrino energies ranging from 0.5 - 5 GeV. Recently, P5 recommended dissolving the LBNE collaboration and shifting the timescale further into the future, as well as redesigning it as LBNF with design details to be influenced by earlier detectors [141].

Additional proposed experiments include ICARUS+NESSIE [142] (∼100 and ∼500 tons, short baseline) at CERN which would search for sterile neutrino oscillations, MODULAr [143] (∼5 kilotons, long baseline) at Gran Sasso, GLADE [144] (∼5 kilotons, long baseline) along the NuMI beam, and an experiment at Okinoshima [145] (∼100 kilotons, long baseline) using a new beam from J-PARC with similar physics goals to LBNE.

7.3 A Lightguide System for Light Detection in Future LArTPCs

7.3.1 Description of System

Future LArTPCs will require a light collection system with a slimmer profile than that of the MicroBooNE and ICARUS systems. Scaling up the current design would be bulky, consuming valuable LAr volume within the tank, especially for systems which propose multiple TPCs within the same volume of liquid argon.

The system described in References [38] and [37] would place thin, TPB-coated lightguides behind or in-between the anode plane assemblies of these detectors. The lightguides would be instrumented at the ends with PMTs or silicon photomultipliers (SiPMs) and associated electronics located outside of the drift region. A photo of bars adiabatically bent to form a paddle is shown in Figure 7-1. SiPM readout would eliminate the need for the bending.

The basic principle of operation for the lightguide system is that when 128 nm argon scintillation light is incident on the TPB-embedded coating, it is absorbed and re-emitted as blue light inside of the coating. The light is re-emitted isotropically, and some of the light is captured and totally internally reflected to the end of the lightguide.

The primary types of coatings under study for this purpose are PS25% and UVT33%, as described in Section 6.4.1. While Figure 6-14 shows that the PS coating has a higher overall efficiency, it has a lower efficiency when applied to the lightguides due to an index of refraction mismatch with the base acrylic. The higher index of refraction of PS (n=1.59) compared with acrylic (n=1.49) causes some of the light to be trapped via total internal reflection in the coating itself, suffering rapid surface attenuation losses due to the thinness of the coating. The base acrylic used in the reported studies is McMaster Carr cast acrylic, cut and polished by Altec Plastics.

7.3.2 MIT Lightguide Test Stand

Our test stand at MIT uses a cryogenic Hamamatsu R7725mod 2-inch PMT. The lightguide is held in the center of an aluminum cylinder by nylon-tipped screws. The aluminum cylinder fits into a cut-out in the PMT holder, allowing the lightguide to be in contact with the face of the PMT. Photographs of the PMT and lightguide holder can be seen in Figure 7-2. A ^{210}Po alpha source is placed at a distance of 5 mm from the lightguide at a particular location along the guide and emits 5.3 MeV α particles, which produce 128 nm light via argon scintillation. Data is acquired using an Alazar Tech ATS9870 digitizer.

Due to quenching of the late light component by impurities in the argon [146, 147], the light in the trigger pulse primarily consists the fast scintillation light (Section 6.3.1). Despite the quenching, some late light is still seen, and single photons from this process can be seen following the trigger pulse. Example waveforms consisting both of the trigger pulse and trailing late-light pulses are shown in Figure 7-3. Because most of the late light pulses consist of one photoelectron, we can use a distribution of late-light pulses to calibrate the gain of the PMT. Note that this analysis uses different digitizer settings than those described in Section 6.4.2 and so the the y-axis does not correspond to the same voltage as the pulses of that section.

Measurements are made by integrating over the pulse from 30 ns before the trigger to 120 ns after the trigger, where the trigger is set at a pulse height of 17 ADC counts. Examples of measurements of these integrated charge distributions at different distances along a cast acrylic bar with a UVT33% coating can be seen in Figure 7-4.

Characterization of lightguides

Figure 7-5 shows the results of averaging measurements, such as those in Figure 7-4, over four bars and four batches of LAr taken during a period of 60 days. Measurements at each position were averaged for a measurement of the attenuation length.

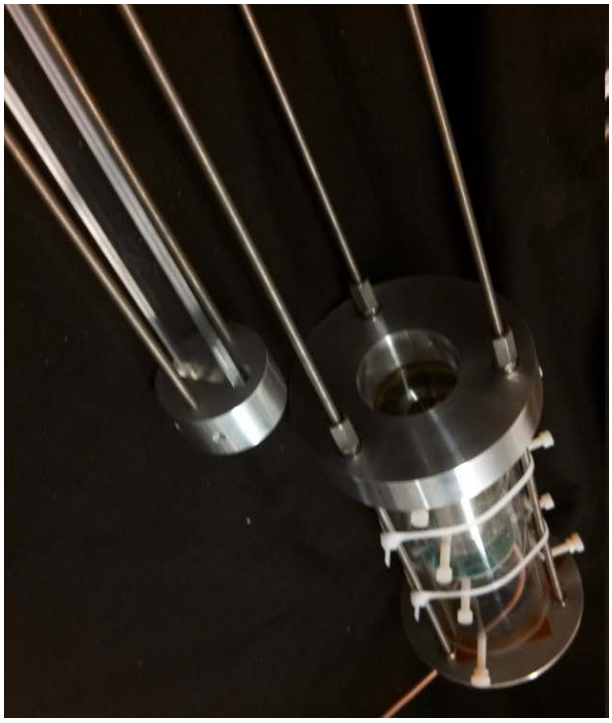

Figure 7-2: A photograph of a lightguide held in place by 4 nylon-tipped set-screws in a cylindrical holder next to a 2 inch PMT in its holder. A ^{210}Po source can be clipped to an adjustable position along the lightguide. The PMT holder is inserted into a glass dewar filled with LAr and allowed to cool, at which point the lightguide holder is inserted. The configuration allows the end of the lightguide to be held in optical connection with the face of the PMT.

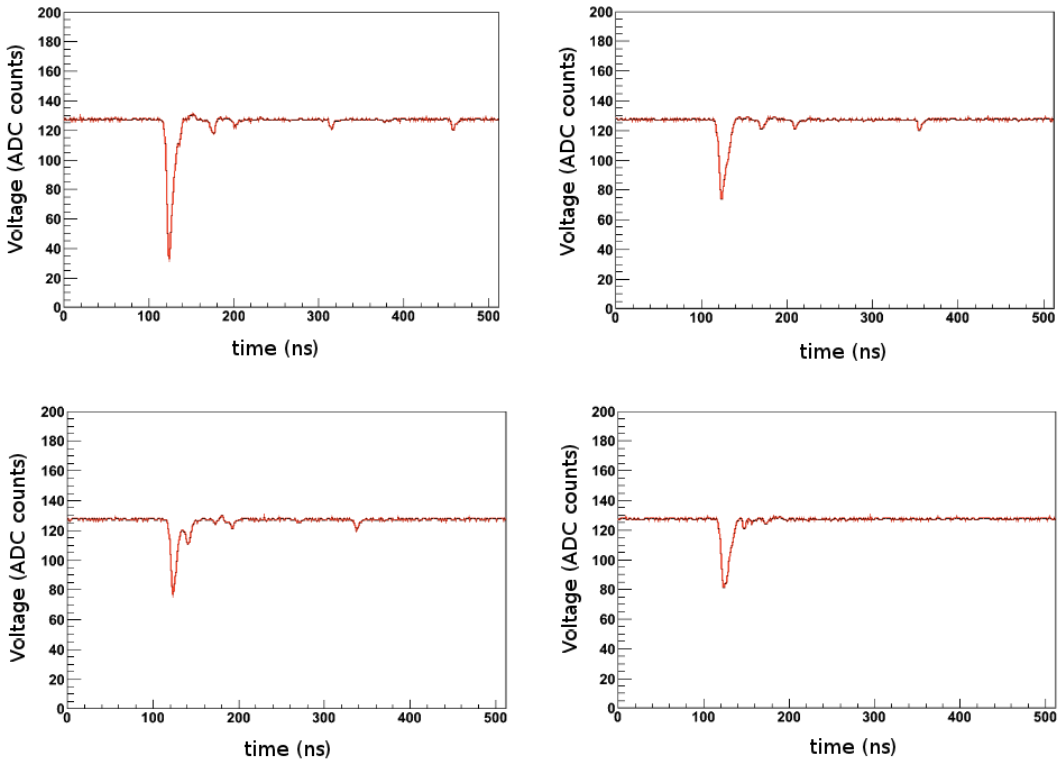

Figure 7-3: Examples of events read-out with a waveform digitizer using a scale of ±200 mV/256 ADC counts. The trigger pulse consisting mainly of early light, and single-p.e. pulses due to the late light, are clearly visible in each event. From Reference [37].

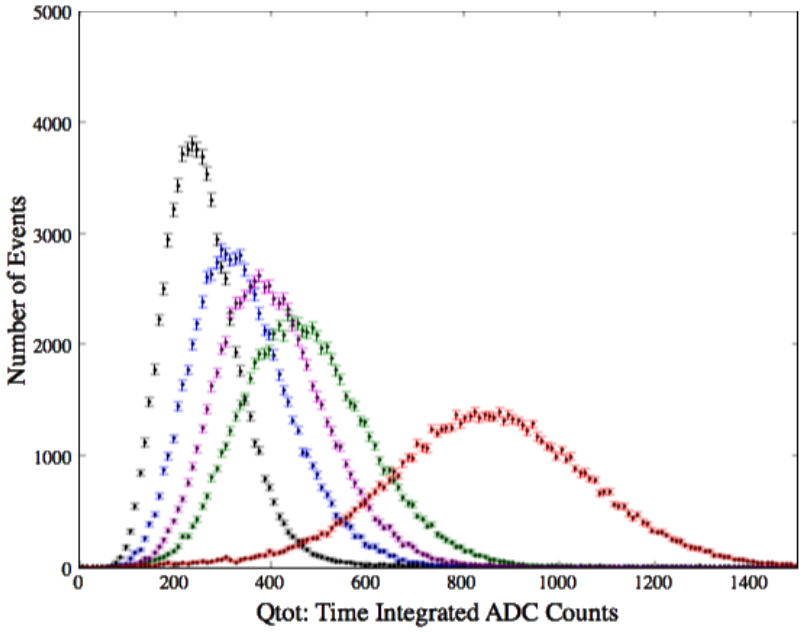

Figure 7-4: A variety of example integrated charge distributions at different distances along a cast acrylic bar with a UVT33% coating. In order from left to right, these distances are: Black: 50 cm, blue: 40 cm, magenta: 30 cm, green: 20 cm, red: 10 cm. From Reference [37].

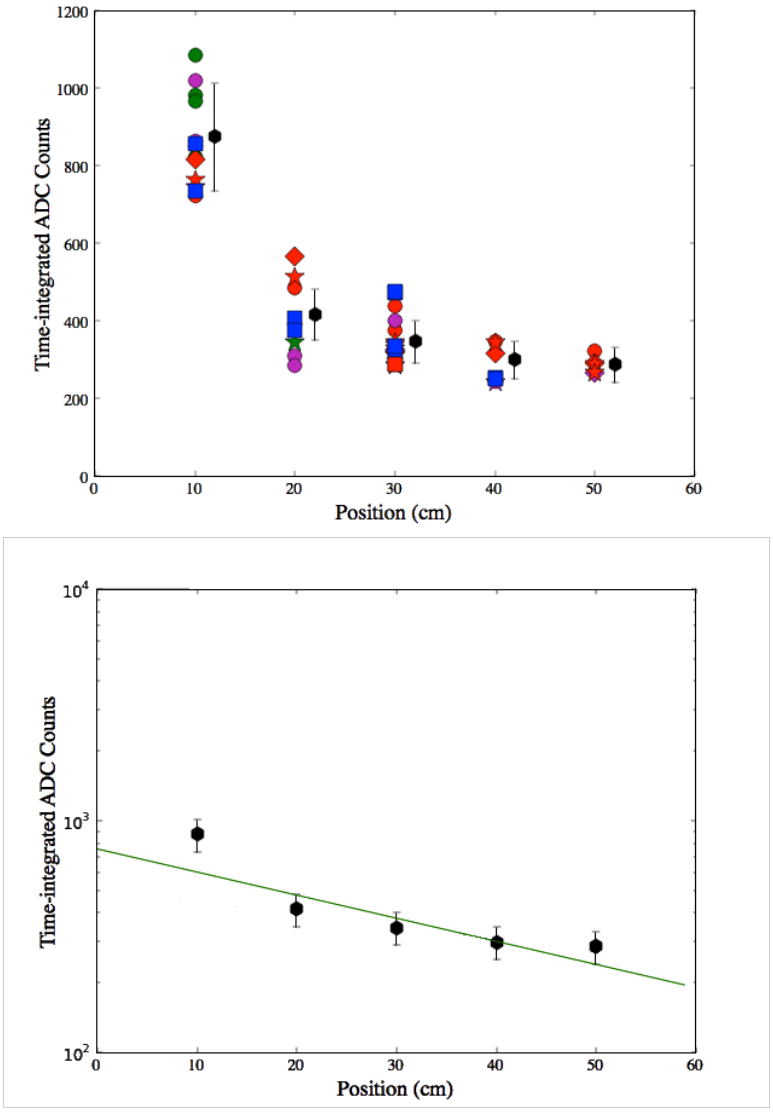

Figure 7-5: Attenuation length measurement of cast acrylic bars with UVT25% coatings. Top: colors and symbols represent four batches of LAr and and four bars respectively, showing consistency when changing these variables. Bottom: Exponential fits to the mean measurement at each position yields an attenuation length of 44 cm.

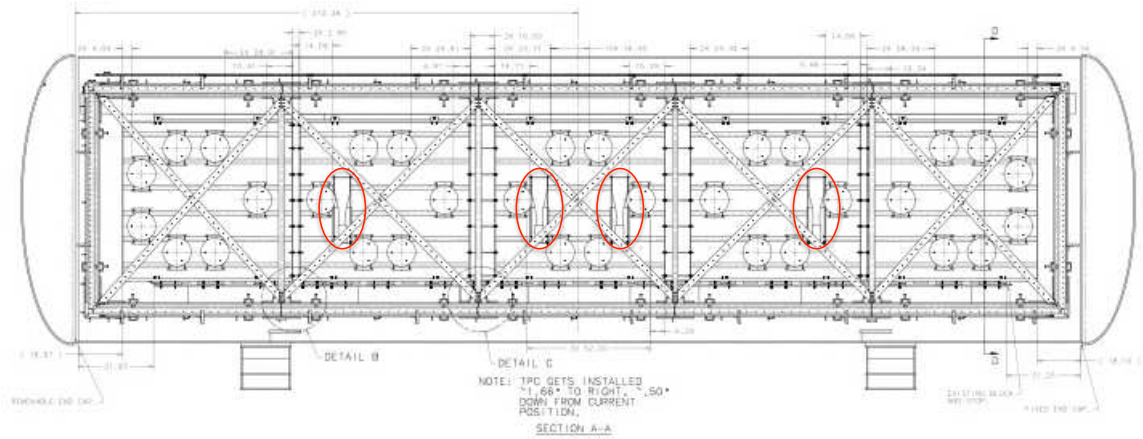

Figure 7-6: The placement of four lightguide paddles (circled) in the MicroBooNE PMT rack.

The attenuation length of cast acrylic bars with a UVT 25% coating was measured to be 44 cm, (compared with 38 cm in air). The result does not look particularly exponential, which has lead to the simulation studies described in Reference [148].

We can expect a different attenuation behavior for the same bar in air and LAr, due to the different refractive indices of light in argon and air. In addition to this, we do not expect perfect exponential attenuation, due to the losses experienced in both the bulk of the acrylic and on the surface. Bulk losses occur as the light is transmitted through the bar and surface losses occur every time the light bounces off of one of the surfaces. Unfortunately, we are unable to measure bulk and surface losses individually. However, our measured attenuation length is significantly shorter than the bulk attenuation length in most commercial acrylics (which are on the order of several meters), so we can assume that surface effects dominate. This is consistent with studies done by the nEDM experiment [149], which measured a bulk attenuation of 6.5 m with a 6% absorption per bounce for their cast surface. So for these reasons, we assume attenuation from surface effects only in the model described in Reference [148]. Reference [148] uses the measured attenuation length in air to calculate a surface absorption coefficient to predict attenuation behavior in argon. This results in a better match to our data than the exponential fit shown.

Four lightguide paddles (as shown in Figure 7-1) have been installed into MicroBooNE for a direct comparison between the MicroBooNE plate system and the lightguide system described in Reference [37]. They are placed on the PMT rack as shown in Figure 7-6.

Since our publications, changes to the base acrylic and coating method have led to further attenuation length improvements. Vertically dipping the bars into solution provides a much more uniform coating with attenuation lengths ∼1 m [150].

Chapter 8

Future Sterile Neutrino Searches

A number of sterile neutrino searches have been proposed which aim to exclude or confirm the LSND signal and other SBL anomalies. The community is aware of the need for a definitive search using a variety of channels [141]. These searches employ the use of various sources, such as reactors, accelerators, and radioactive sources. The sections in this chapter describe several of these experiments.

MiniBooNE was designed to be definitive, but despite the extraordinary sensitivity that it achieved, led to further questions. The reason MiniBooNE was not definitive was because it saw something that was more complicated than what was expected. It is good to keep this in mind when looking at sensitivity plots for future experiments.

8.1 LAr at Fermilab

The MicroBooNE experiment is an important step in the SBL picture, as it will address the MiniBooNE low-energy excess. MicroBooNE is discussed in detail in Chapter 6. While this is an important question to answer, MicroBooNE will not provide definitive information about the existence of one or more sterile neutrinos. As discussed in Section 5.3, the MiniBooNE low-energy excess is a source of tension even within the framework of sterile neutrinos. This means that even if MicroBooNE determines that the excess is due to a gamma background, this will not help to solve the other SBL anomalies. If the excess remains, it may indicate that sterile neutrino models are insufficient to explain the MiniBooNE data.

There are two new proposals involving liquid argon detectors at Fermilab. The LArTPC technology aspects of these detectors are discussed in Section 7.2. The first is LAr1-ND [120], which would put a near detector in the hall that housed the former SciBooNE experiment. It would be an 82 ton LArTPC located at a baseline of 100 m. This would improve future large detectors by providing a near detector, as well as providing valuable R&D for the next steps in the U.S. LArTPC program. The second proposal is to use the existing ICARUS T600 detector as a far detector, with the ICARUS 150T detector as a near detector [151]. Combining forces could lead to a strong program involving multiple detectors: LAr1-ND, MicroBooNE, and ICARUS.

The sensitivity for combining LAr1-ND and MicroBooNE is shown in Figure 8-1,

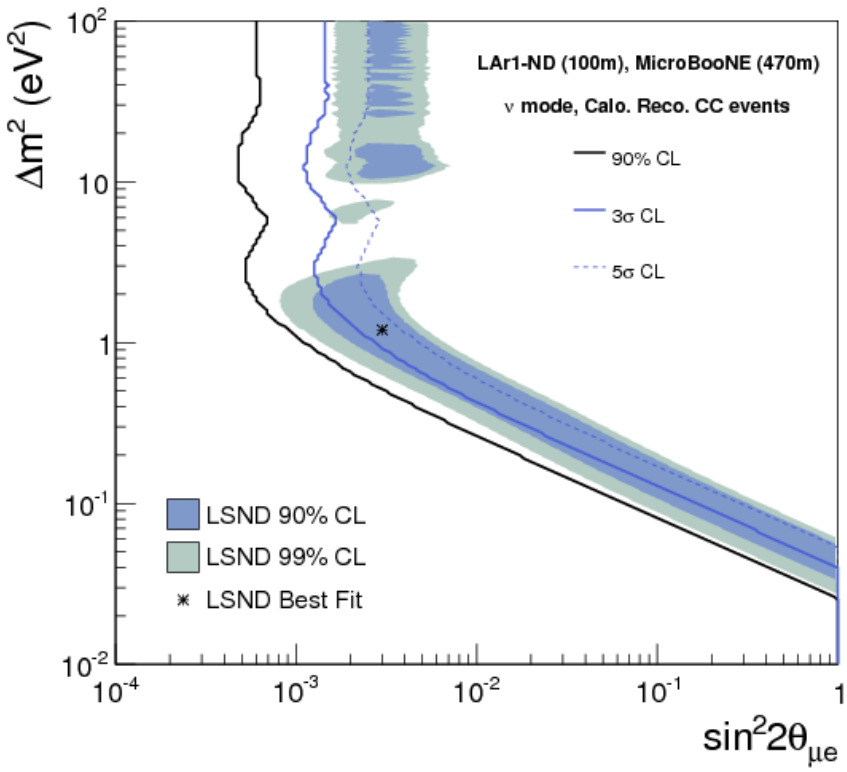

Figure 8-1: The sensitivity expected by the proposed LAr1-ND detector combined with MicroBooNE. This assumes 6.6 $\times 10^{20}$ POT for MicroBooNE and 2.2 $\times 10^{20}$ POT for LAr1-ND. From Reference [120].

and and the ICARUS sensitivity using an ICARUS-style near (150T) and far (T600) detectors is in Figure 8-2. These are shape-only fits, meaning that the resulting spectrum will be normalized to the total number of predicted events. Combining both these approaches would achieve even better sensitivity.

The sensitivity is not sufficient for a definitive measurement if there is a positive signal, however would set a strong limit and possibly exclude the existing anomalies if there is a negative signal.

8.2 IsoDAR

IsoDAR (Isotope Decay At Rest) [153] is an experiment which uses the injector cyclotron design for the DAEδALUS [22] experiment. Protons at 60 MeV are produced by the cyclotron and impinge on a ^{9}Be Target within a ^{7}Li sleeve. This creates ^{8}Li primarily through neutron capture in the ^{7}Li shell:

$$n +^7 \text{Li} \rightarrow^8 \text{Li} + \gamma \tag{8.1}$$

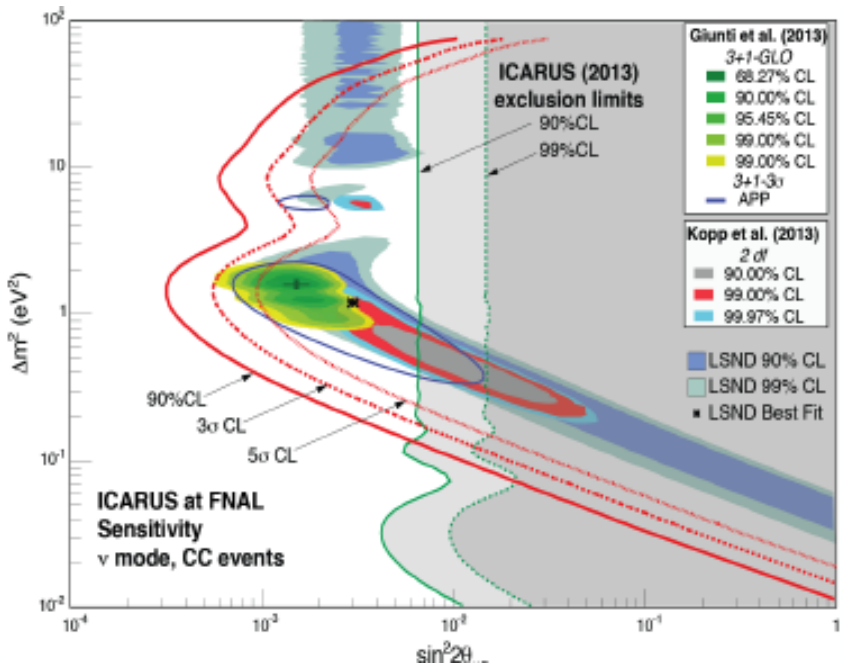

Figure 8-2: The sensitivity expected by the proposed ICARUS @ FNAL in neutrino mode for 3 years of running. From Reference [152].

The lithium-8 then decays into electron antineutrinos:

$$^{8}\text{Li} \rightarrow ^{8}\text{Be} + e^{-} + \bar{\nu}_e \tag{8.2}$$

The $\bar{\nu}_e$s are then detected in a large liquid scintillator detector and a $\bar{\nu}_e \rightarrow \bar{\nu}_e$ disappearance search is performed. The collaboration intends to use an existing or proposed detector, such as KAMLAND [9] or JUNO [154]. Studies as well as communication with these collaborations are underway.

The IsoDAR experiment is a good example of a definitive experiment because of its ability to observe the multiple undulations of an oscillation wave (Figure 8-3). The sensitivity is shown in Figure 8-4. Because of this ability to observe multiple wavelengths, IsoDAR has the advantage that if it does see a signal, it will have much smaller allowed regions. This means that if it observes oscillations, it can determine the parameters to a high confidence level. It can even distinguish between a $3+1$ and $3+2$ model. The sensitivity of IsoDAR to a variety of potential $3+1$ signal parameters is shown in Figure 8-5.

8.3 SOX

The SOX concept [155] is similar to the Gallium experiments described in Section 2.1.4, involving the placement of radioactive sources inside and/or nearby the Borexino [156] detector. The proposed sources are ^{51}Cr and ^{144}Ce-^{144}Pr. The ^{51}Cr source emits neutrino lines of 430 keV and 750 keV after undergoing electron capture. The

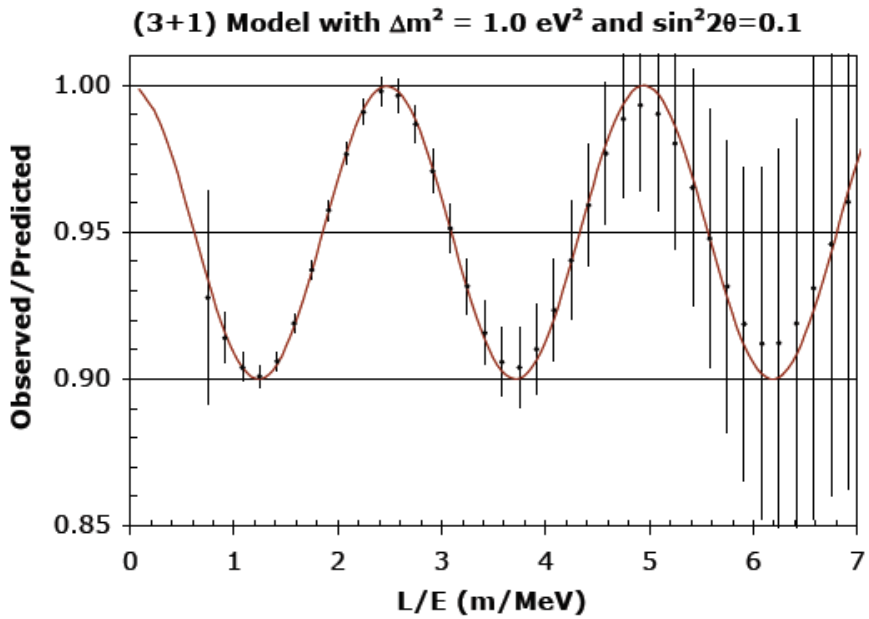

Figure 8-3: Predicted errors on data points along an oscillation wave with parameters $\Delta m^2 = 1$ eV^2 and $\sin^2 2\theta = 0.1$ for 5 years of IsoDAR running at the KAMLAND detector. From Reference [22].

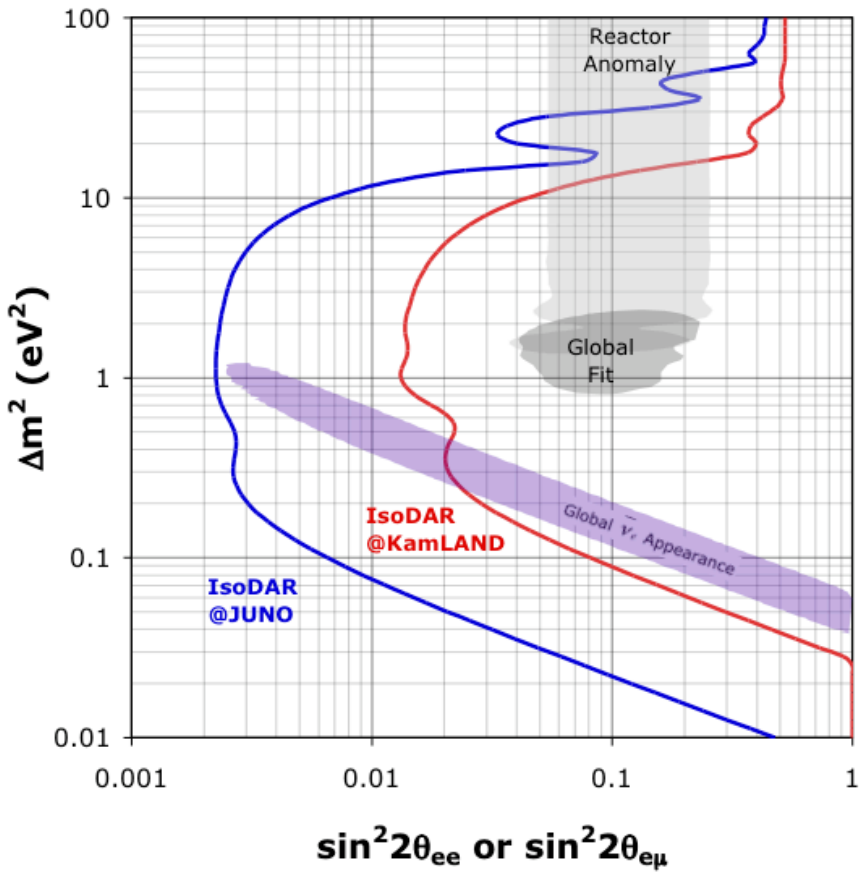

Figure 8-4: The sensitivity expected by IsoDAR at Juno or IsoDAR at KAMLAND. From Reference [153].

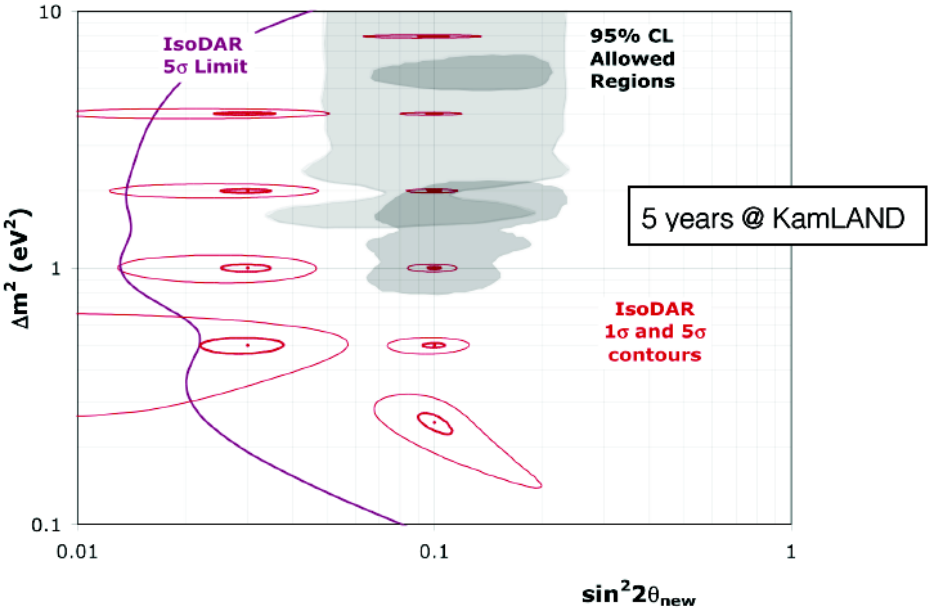

Figure 8-5: The sensitivity expected by IsoDAR with 5 years of running at KamLAND for a variety of potential signal parameters. From Reference [153].

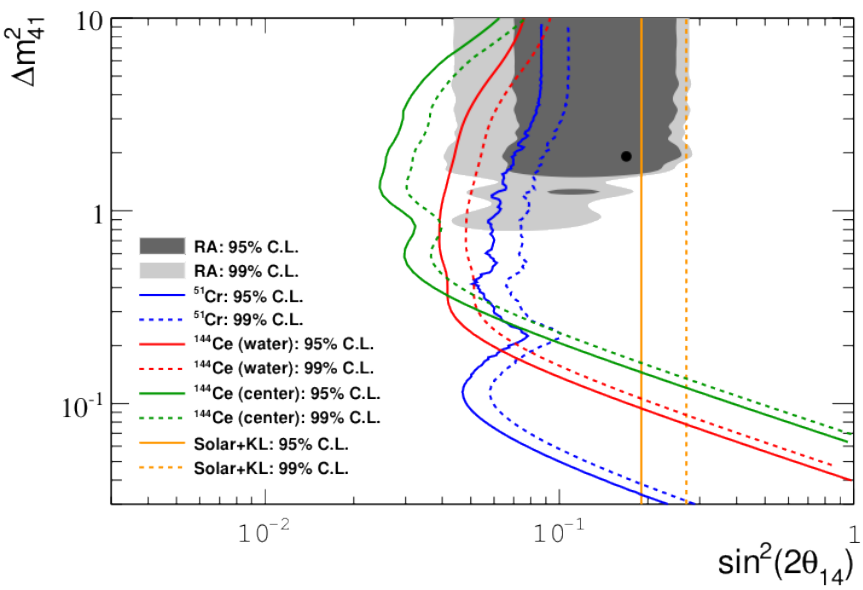

Figure 8-6: The sensitivity expected by the SOX experiment for each of its three phases. The sensitivity is plotted over the allowed region from the reactor anomaly for comparison. From Reference [155].

^{144}Ce-^{144}Pr source begins with a ^{144}Ce decay into ^{144}Pr, at which point the ^{144}Pr decays into ^{144}Nd. The antineutrinos produced in the ^{144}Pr are used for the disappearance analysis, as those produced by the ^{144}Ce decay are below threshold and therefore cannot be detected.

Reference [155] describes three phases. Phase A places a ^{51}Cr source in an existing tunnel located beneath the Borexino detector, at a distance of 8.25 m from the center of the detector. Phase B uses a 2.3 PBq ^{144}Ce-^{144}Pr source located within the water tank but outside of the scintillator volume. Phase C places a 1.5 PBq ^{144}Ce-^{144}Pr source inside the detector volume, located at the center of the detector.

The sensitivity of each of these phases is shown in Figure 8-6. While SOX is not a definitive experiment, execution of phase one can proceed rapidly, as the tunnel already exists and inserting the source will not require modifications to the detector.

8.4 νSTORM

νSTORM [157] proposes to look for ν_μ appearance from a ν_e source. It uses a precursor to a neutrino factory to produce the ν_es, using a muon ring where the muons are produced by pion decay-in-flight beam. The muons then decay into electron neutrinos:

$$\mu^+ \rightarrow \bar{\nu}_\mu + \nu_e + e^+ \tag{8.3}$$

This reversal of the usual process of $\nu_\mu \rightarrow \nu_e$ enables νSTORM to count ν_μ events over muon-like backgrounds while probing the exact same parameter space. The

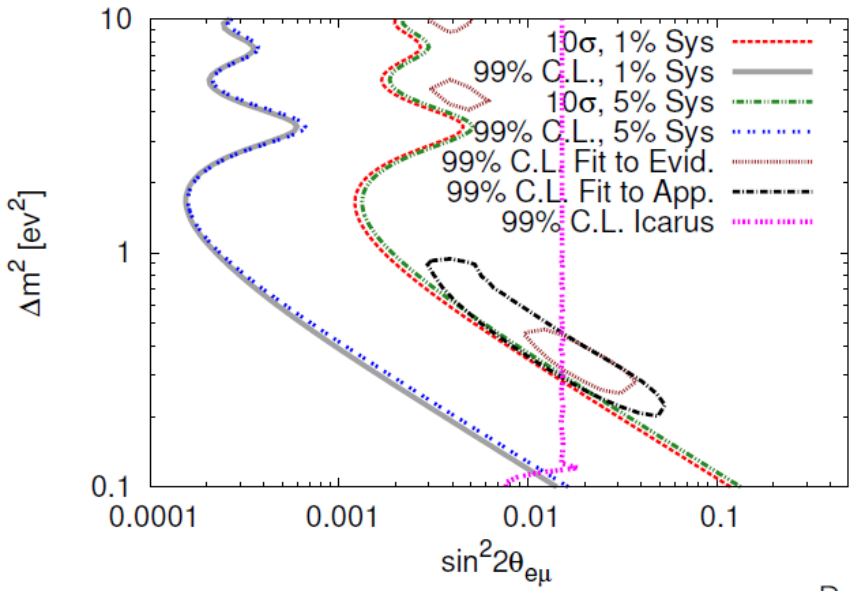

Figure 8-7: The sensitivity expected by the νSTORM experiment for 10 years of running with a near detector at 100 m and 1.3 kton far detector at 2 km. From Reference [157] .

sensitivities achievable with the νSTORM detector are shown in Figure 8-7. While the sensitivity of νSTORM is excellent, it was not recommended by the recent Particle Physics Project Prioritization Panel (P5) report [141] and therefore is unlikely to move forward in the near future.

8.5 OscSNS

OscSNS uses an LSND-style liquid scintillator detector with lightly doped oil. Like LSND, it uses a DAR beam, impinging 1 GeV protons on a mercury target and searching for $\nu_\mu \to \nu_e$. Unlike most of the other proposed sterile neutrino searches, OscSNS [158] can detect Neutral Current interactions rather than Charged Current interactions (Section 1.1). This allows for a direct probe of the sterile content of the fourth mass state since the electron, muon, and tau flavored neutrino cross-sections are identical, so any observed deficit caused by oscillations would be into a sterile state. OscSNS would search for muon neutrino disappearance using a very high power (1.5 MW) proton beam at Oak Ridge National Lab.

The sensitivity of OscSNS is shown in Figure 8-8. If nothing is seen, it would definitively rule out the LSND experiment.

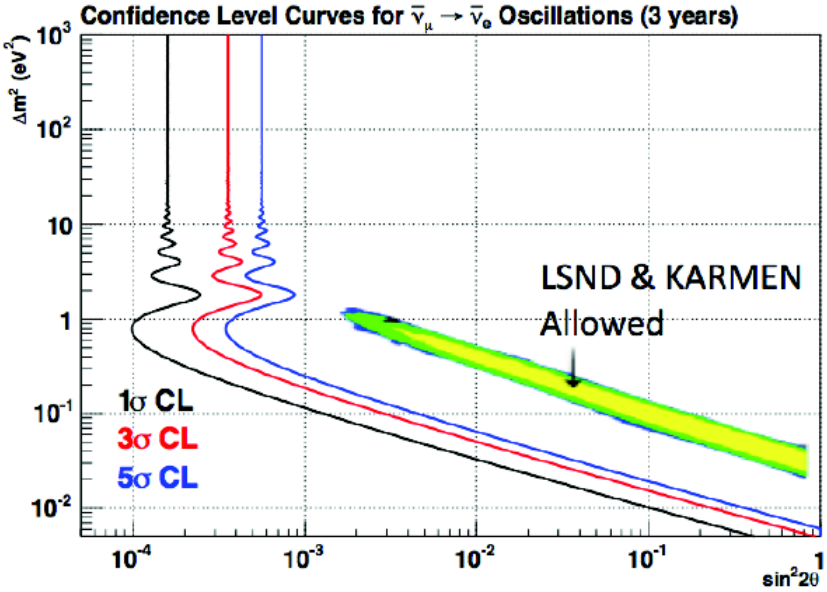

Figure 8-8: The sensitivity expected by OscSNS for three years of running. From Reference [159].

8.6 Ricochet

Ricochet also detects NC interactions, and would detect (and discover) coherent neutrino scattering, which has never before been seen [160]. This is an attractive prospect, as the coherent neutrino scattering cross-sections are expected to be much higher than scattering off of individual nucleons. Coherent neutrino scattering involves a neutrino recoiling off of the target nucleus, rather than knocking out a particular proton or neutron from the nucleus. The resulting nuclear recoil is then detected. The signature for such an interaction is very similar to that of the nuclear recoil initiated by a WIMP [160]. Detection would be accomplished using low-temperature bolometers and a design very similar to the CDMS dark matter detector [161].

Chapter 9

Conclusion

This thesis has presented an overview of sterile neutrinos and the short-baseline anomalies. We have discussed the final results of the MiniBooNE electron-flavored neutrino and antineutrino appearance searches. We have reported a consistency between the MiniBooNE antineutrino-mode results and the LSND anomaly, but tension between the MiniBooNE neutrino and antineutrino mode results. In addition, the MiniBooNE low-energy excess still remains a mystery. Global fits to world oscillation data indicate that the tension among short baseline experiments is not completely resolved with the addition of 1, 2, or even 3 sterile neutrinos.

The MicroBooNE experiment will begin taking data in early 2015 and should shed light on the MiniBooNE low-energy excess. While the $(3 + N)$ models considered produce better results than fits without sterile neutrinos, we find that current data are still insufficient to determine the viability of these models. There are a number of future and proposed experiments that will be sensitive to sterile neutrinos including many sensitive to the preferred parameter space from these fits. We conclude that future experiments are necessary to further investigate these scenarios to confirm or rule out sterile neutrino models.

Bibliography

[1] C. Cowan, F. Reines, F. Harrison, H. Kruse, and A. McGuire, "Detection of the free neutrino: A Confirmation," *Science*, vol. 124, pp. 103–104, 1956.

[2] J. Beringer *et al.*, "Review of Particle Physics (RPP)," *Phys.Rev.*, vol. D86, p. 010001, 2012.

[3] S. Schael *et al.*, "Precision electroweak measurements on the Z resonance," *Phys.Rept.*, vol. 427, pp. 257–454, 2006.

[4] C. Wu, E. Ambler, R. Hayward, D. Hoppes, and R. Hudson, "Experimental Test of Parity Conservation in Beta Decay," *Phys.Rev.*, vol. 105, pp. 1413–1414, 1957.

[5] J. N. Bahcall, A. M. Serenelli, and S. Basu, "New solar opacities, abundances, helioseismology, and neutrino fluxes," *Astrophys.J.*, vol. 621, pp. L85–L88, 2005.

[6] F. Kaether, W. Hampel, G. Heusser, J. Kiko, and T. Kirsten, "Reanalysis of the GALLEX solar neutrino flux and source experiments," *Phys.Lett.*, vol. B685, pp. 47–54, 2010.

[7] J. Abdurashitov *et al.*, "Measurement of the solar neutrino capture rate with gallium metal. III: Results for the 2002–2007 data-taking period," *Phys.Rev.*, vol. C80, p. 015807, 2009.

[8] Y. Fukuda *et al.*, "Evidence for oscillation of atmospheric neutrinos," *Phys.Rev.Lett.*, vol. 81, pp. 1562–1567, 1998.

[9] S. Abe *et al.*, "Precision Measurement of Neutrino Oscillation Parameters with KamLAND," *Phys.Rev.Lett.*, vol. 100, p. 221803, 2008.

[10] B. Aharmim *et al.*, "Electron energy spectra, fluxes, and day-night asymmetries of B-8 solar neutrinos from measurements with NaCl dissolved in the heavy-water detector at the Sudbury Neutrino Observatory," *Phys.Rev.*, vol. C72, p. 055502, 2005.

[11] P. Adamson *et al.*, "A Study of Muon Neutrino Disappearance Using the Fermilab Main Injector Neutrino Beam," *Phys.Rev.*, vol. D77, p. 072002, 2008.

[12] E. Aliu *et al.*, "Evidence for muon neutrino oscillation in an accelerator-based experiment," *Phys.Rev.Lett.*, vol. 94, p. 081802, 2005.

[13] K. Abe *et al.*, "Indication of Electron Neutrino Appearance from an Accelerator-produced Off-axis Muon Neutrino Beam," *Phys.Rev.Lett.*, vol. 107, p. 041801, 2011.

[14] Y. Abe *et al.*, "Reactor electron antineutrino disappearance in the Double Chooz experiment," *Phys.Rev.*, vol. D86, p. 052008, 2012.

[15] F. An *et al.*, "Observation of electron-antineutrino disappearance at Daya Bay," *Phys.Rev.Lett.*, vol. 108, p. 171803, 2012.

[16] J. Ahn *et al.*, "Observation of Reactor Electron Antineutrino Disappearance in the RENO Experiment," *Phys.Rev.Lett.*, vol. 108, p. 191802, 2012.

[17] C. Kraus, B. Bornschein, L. Bornschein, J. Bonn, B. Flatt, *et al.*, "Final results from phase II of the Mainz neutrino mass search in tritium beta decay," *Eur.Phys.J.*, vol. C40, pp. 447–468, 2005.

[18] V. Aseev *et al.*, "An upper limit on electron antineutrino mass from Troitsk experiment," *Phys.Rev.*, vol. D84, p. 112003, 2011.

[19] R. H. Robertson, "KATRIN: an experiment to determine the neutrino mass from the beta decay of tritium," 2013.

[20] K. Babu, E. Kearns, U. Al-Binni, S. Banerjee, D. Baxter, *et al.*, "Working Group Report: Baryon Number Violation," 2013.

[21] T. A. et. al [LBNE Collaboration], "The 2010 Interim Report of the Long-Baseline Neutrino Experiment Collaboration Physics Working Groups," arXiv:1110.6249 [hep-ex].

[22] C. Aberle, A. Adelmann, J. Alonso, W. Barletta, R. Barlow, *et al.*, "Whitepaper on the DAEdALUS Program," 2013.

[23] R. Patterson, "The NOvA Experiment: Status and Outlook," *Nucl.Phys.Proc.Suppl.*, vol. 235-236, pp. 151–157, 2013.

[24] M. Aartsen *et al.*, "Letter of Intent: The Precision IceCube Next Generation Upgrade (PINGU)," 2014.

[25] I. Avignone, Frank T., S. R. Elliott, and J. Engel, "Double Beta Decay, Majorana Neutrinos, and Neutrino Mass," *Rev.Mod.Phys.*, vol. 80, pp. 481–516, 2008.

[26] J. Albert *et al.*, "Search for Majorana neutrinos with the first two years of EXO-200 data," *Nature*, vol. 510, p. 229234, 2014.

[27] P. Gorla, "The CUORE experiment: Status and prospects," *J.Phys.Conf.Ser.*, vol. 375, p. 042013, 2012.

[28] A. Barabash and V. Brudanin, "Investigation of double beta decay with the NEMO-3 detector," *Phys.Atom.Nucl.*, vol. 74, pp. 312–317, 2011.

[29] M. Agostini *et al.*, "Results on Neutrinoless Double-β Decay of ^{76}Ge from Phase I of the GERDA Experiment," *Phys.Rev.Lett.*, vol. 111, no. 12, p. 122503, 2013.

[30] A. Gando *et al.*, "Limit on Neutrinoless $\beta\beta$ Decay of Xe-136 from the First Phase of KamLAND-Zen and Comparison with the Positive Claim in Ge-76," *Phys.Rev.Lett.*, vol. 110, no. 6, p. 062502, 2013.

[31] H. Klapdor-Kleingrothaus, A. Dietz, H. Harney, and I. Krivosheina, "Evidence for neutrinoless double beta decay," *Mod.Phys.Lett.*, vol. A16, pp. 2409–2420, 2001.

[32] C. Aalseth, I. Avignone, F.T., A. Barabash, F. Boehm, R. Brodzinski, *et al.*, "Comment on 'Evidence for neutrinoless double beta decay'," *Mod.Phys.Lett.*, vol. A17, pp. 1475–1478, 2002.

[33] A. Bakalyarov, A. Y. Balysh, S. Belyaev, V. Lebedev, and S. Zhukov, "Results of the experiment on investigation of Germanium-76 double beta decay: Experimental data of Heidelberg-Moscow collaboration November 1995 - August 2001," *Phys.Part.Nucl.Lett.*, vol. 2, pp. 77–81, 2005.

[34] L. Winslow, "Future Neutrinoless Double-Beta Decay Experiments." Slides from Neutrino2014 (Proceedings in Preparation), 2014.

[35] A. Aguilar-Arevalo *et al.*, "Improved Search for $\bar{\nu}_\mu \to \bar{\nu}_e$ Oscillations in the MiniBooNE Experiment," *Phys.Rev.Lett.*, vol. 110, p. 161801, 2013.

[36] J. Conrad, C. Ignarra, G. Karagiorgi, M. Shaevitz, and J. Spitz, "Sterile Neutrino Fits to Short Baseline Neutrino Oscillation Measurements," *Adv.High Energy Phys.*, vol. 2013, p. 163897, 2013.

[37] B. Baptista, L. Bugel, C. Chiu, J. Conrad, C. Ignarra, *et al.*, "Benchmarking TPB-coated Light Guides for Liquid Argon TPC Light Detection Systems," 2012. arXiv:1110.6249 [hep-ex].

[38] L. Bugel, J. Conrad, C. Ignarra, B. Jones, T. Katori, T. Smidt, and H.-K. Tanaka, "Demonstration of a lightguide detector for liquid argon TPCs," *Nucl.Instrum.Meth.*, vol. 640, no. 1, pp. 69 – 75, 2011.

[39] C. S. Chiu, C. Ignarra, L. Bugel, H. Chen, J. M. Conrad, B. J. P. Jones, T. Katori, and I. Moult, "Environmental effects on TPB wavelength-shifting coatings," *JINST*, vol. 7, no. 07, p. P07007, 2012.

[40] A. Aguilar-Arevalo *et al.*, "Evidence for neutrino oscillations from the observation of anti-neutrino(electron) appearance in a anti-neutrino(muon) beam," *Phys.Rev.*, vol. D64, p. 112007, 2001.

[41] R. Slansky, S. Raby, J. T. Goldman, and G. Garvey, "The oscillating neutrino: An introduction to neutrino masses and mixings," *Los Alamos Sci.*, vol. 25, pp. 28–63, 1997.

[42] C. Athanassopoulos *et al.*, "The Liquid scintillator neutrino detector and LAMPF neutrino source," *Nucl.Instrum.Meth.*, vol. A388, pp. 149–172, 1997.

[43] E. Church *et al.*, "A Letter of Intent for an experiment to measure muon-neutrino $\rightarrow$ electron-neutrino oscillations and muon-neutrino disappearance at the Fermilab Booster: BooNE," 1997.

[44] Y. Abe *et al.*, "Reactor electron antineutrino disappearance in the Double Chooz experiment," *Phys.Rev.*, vol. D86, p. 052008, 2012.

[45] C. Jones, A. Bernstein, J. Conrad, Z. Djurcic, M. Fallot, *et al.*, "Reactor Simulation for Antineutrino Experiments using DRAGON and MURE," *Phys.Rev.*, vol. D86, p. 012001, 2012.

[46] T. Mueller, D. Lhuillier, M. Fallot, A. Letourneau, S. Cormon, *et al.*, "Improved Predictions of Reactor Antineutrino Spectra," *Phys.Rev.*, vol. C83, p. 054615, 2011.

[47] G. Mention, M. Fechner, T. Lasserre, T. Mueller, D. Lhuillier, *et al.*, "The Reactor Antineutrino Anomaly," *Phys.Rev.*, vol. D83, p. 073006, 2011.

[48] P. Huber, "On the determination of anti-neutrino spectra from nuclear reactors," *Phys.Rev.*, vol. C84, p. 024617, 2011.

[49] K. Abazajian, M. Acero, S. Agarwalla, A. Aguilar-Arevalo, C. Albright, *et al.*, "Light Sterile Neutrinos: A White Paper," 2012.

[50] A. Hayes, J. Friar, G. Garvey, G. Jungman, and G. Jonkmans, "Systematic Uncertainties in the Analysis of the Reactor Neutrino Anomaly," *Phys.Rev.Lett.*, vol. 112, p. 202501, 2014.

[51] J. Abdurashitov, V. Gavrin, S. Girin, V. Gorbachev, P. Gurkina, *et al.*, "Measurement of the response of a Ga solar neutrino experiment to neutrinos from an Ar-37 source," *Phys.Rev.*, vol. C73, p. 045805, 2006.

[52] C. Giunti and M. Laveder, "Statistical Significance of the Gallium Anomaly," *Phys.Rev.*, vol. C83, p. 065504, 2011.

[53] J. Abdurashitov, V. Gavrin, S. Girin, V. Gorbachev, P. Gurkina, *et al.*, "Measurement of the response of a Ga solar neutrino experiment to neutrinos from an Ar-37 source," *Phys.Rev.*, vol. C73, p. 045805, 2006.

[54] "The Particle Zoo." www.particlezoo.net.

[55] "Photoshop." www.photoshop.com.

[56] B. Dasgupta and J. Kopp, "Cosmologically Safe eV-Scale Sterile Neutrinos and Improved Dark Matter Structure," *Phys.Rev.Lett.*, vol. 112, no. 3, p. 031803, 2014.

[57] S. Hannestad, R. S. Hansen, and T. Tram, "How Self-Interactions can Reconcile Sterile Neutrinos with Cosmology," *Phys.Rev.Lett.*, vol. 112, no. 3, p. 031802, 2014.

[58] O. Lahav and A. R. Liddle, "The Cosmological Parameters 2014," 2014.

[59] M. Archidiacono, N. Fornengo, S. Gariazzo, C. Giunti, S. Hannestad, *et al.*, "Light sterile neutrinos after BICEP-2," *JCAP*, vol. 1406, p. 031, 2014.

[60] S. Agostinelli *et al.*, "GEANT4: A Simulation toolkit," *Nucl.Instrum.Meth.*, vol. A506, pp. 250–303, 2003.

[61] M. Catanesi *et al.*, "Measurement of the production cross-section of positive pions in the collision of 8.9-GeV/c protons on beryllium," *Eur.Phys.J.*, vol. C52, pp. 29–53, 2007.

[62] I. Chemakin *et al.*, "Pion production by protons on a thin beryllium target at 6.4-Ge, 12.3-GeV/c, and 17.5-GeV/c incident proton momenta," *Phys.Rev.*, vol. C77, p. 015209, 2008.

[63] J. Sanford and C. Wang, "EMPIRICAL FORMULAS FOR PARTICLE PRODUCTION IN P - Be COLLISION BETWEEN 10-GeV/c AND 35-GeV/c," 1967.

[64] A. Aguilar-Arevalo *et al.*, "The Neutrino Flux prediction at MiniBooNE," *Phys.Rev.*, vol. D79, p. 072002, 2009.

[65] S. Brice *et al.*, "Photomultiplier tubes in the MiniBooNE experiment," *Nucl.Instrum.Meth.*, vol. A562, pp. 97–109, 2006.

[66] I. Stancu *et al.*, "The MiniBooNE detector technical design report," 2001.

[67] R. Brun, F. Bruyant, M. Maire, A. McPherson, and P. Zanarini, "GEANT3," 1987.

[68] R. B. Patterson, "A search for muon neutrino to electron neutrino oscillations at $\delta(m^2) > 0.1$ eV^2," 2007.

[69] W. C. Louis. Private Communication.

[70] A. Aguilar-Arevalo *et al.*, "The MiniBooNE Detector," *Nucl.Instrum.Meth.*, vol. A599, pp. 28–46, 2009.

[71] D. Casper, "The Nuance neutrino physics simulation, and the future," *Nucl.Phys.Proc.Suppl.*, vol. 112, pp. 161–170, 2002.

[72] J. Formaggio and G. Zeller, "From eV to EeV: Neutrino Cross Sections Across Energy Scales," *Rev.Mod.Phys.*, vol. 84, p. 1307, 2012.

[73] A. Aguilar-Arevalo *et al.*, "First Measurement of the Muon Neutrino Charged Current Quasielastic Double Differential Cross Section," *Phys.Rev.*, vol. D81, p. 092005, 2010.

[74] A. Aguilar-Arevalo *et al.*, "First Measurement of the Muon Anti-Neutrino Double-Differential Charged Current Quasi-Elastic Cross Section," *Phys.Rev.*, vol. D88, p. 032001, 2013.

[75] V. Lyubushkin *et al.*, "A Study of quasi-elastic muon neutrino and antineutrino scattering in the NOMAD experiment," *Eur.Phys.J.*, vol. C63, pp. 355–381, 2009.

[76] A. de Gouvea *et al.*, "Neutrinos," 2013.

[77] R. Patterson, E. Laird, Y. Liu, P. Meyers, I. Stancu, *et al.*, "The Extended-track reconstruction for MiniBooNE," *Nucl.Instrum.Meth.*, vol. A608, pp. 206–224, 2009.

[78] A. Aguilar-Arevalo *et al.*, "Using L/E Oscillation Probability Distributions," 2014.

[79] A. Aguilar-Arevalo *et al.*, "First Observation of Coherent π^0 Production in Neutrino Nucleus Interactions with $E_\nu < 2$ GeV," *Phys.Lett.*, vol. B664, pp. 41–46, 2008.

[80] A. A. Aguilar-Arevalo *et al.*, "Measurement of nu(mu) and anti-nu(mu) induced neutral current single pi0 production cross sections on mineral oil at E(nu) O(1-GeV)," *Phys.Rev.*, vol. D81, p. 013005, 2010.

[81] Z. Djurcic, J. Link, J. L. Raaf, H. A. Tanaka, R. Patterson, and G. Zeller, "Measurement of the Rate of NC pi0 Production at MiniBooNE." MiniBooNE Technical Note 194, 2006.

[82] A. Aguilar-Arevalo *et al.*, "Measurement of the neutrino component of an anti-neutrino beam observed by a non-magnetized detector," *Phys.Rev.*, vol. D84, p. 072005, 2011.

[83] W. Louis, "Revised Determination of the Number of Dirt Events from the Booster Beamline in Antineutrino Mode." MiniBooNE Technical Note 280, 2009.

[84] S. Brice, "An Improved Way to Propagate pi+ Production Uncertainties." MiniBooNE Technical Note 257, 2008.

[85] C. Mariani, G. Cheng, J. Conrad, and M. Shaevitz, "Improved Parameterization of K^+ Production in p-Be Collisions at Low Energy Using Feynman Scaling," *Phys.Rev.*, vol. D84, p. 114021, 2011.

[86] G. Cheng *et al.*, "Measurement of K^+ production cross section by 8 GeV protons using high energy neutrino interactions in the SciBooNE detector," *Phys.Rev.*, vol. D84, p. 012009, 2011.

[87] G. J. Feldman and R. D. Cousins, "A Unified approach to the classical statistical analysis of small signals," *Phys.Rev.*, vol. D57, pp. 3873–3889, 1998.

[88] A. Aguilar-Arevalo *et al.*, "Unexplained Excess of Electron-Like Events From a 1-GeV Neutrino Beam," *Phys.Rev.Lett.*, vol. 102, p. 101802, 2009.

[89] A. Aguilar-Arevalo *et al.*, "A Search for electron neutrino appearance at the $\Delta m^2 \sim 1\text{eV}^2$ scale," *Phys.Rev.Lett.*, vol. 98, p. 231801, 2007.

[90] J. A. Harvey, C. T. Hill, and R. J. Hill, "Anomaly mediated neutrino-photon interactions at finite baryon density," *Phys.Rev.Lett.*, vol. 99, p. 261601, 2007.

[91] S. Gninenko, "Sterile neutrino decay as a common origin for LSND/MiniBooNe and T2K excess events," *Phys.Rev.*, vol. D85, p. 051702, 2012.

[92] J. S. Diaz and A. Kostelecky, "Lorentz- and CPT-violating models for neutrino oscillations," *Phys.Rev.*, vol. D85, p. 016013, 2012.

[93] B. Armbruster *et al.*, "Upper limits for neutrino oscillations muon-anti-neutrino to electron-anti-neutrino from muon decay at rest," *Phys.Rev.*, vol. D65, p. 112001, 2002.

[94] M. Martini, M. Ericson, and G. Chanfray, "Energy reconstruction effects in neutrino oscillation experiments and implications for the analysis," *Phys.Rev.*, vol. D87, p. 013009, 2013.

[95] J. Kopp, P. A. N. Machado, M. Maltoni, and T. Schwetz, "Sterile Neutrino Oscillations: The Global Picture," *JHEP*, vol. 1305, p. 050, 2013.

[96] C. Giunti, M. Laveder, Y. Li, and H. Long, "Pragmatic View of Short-Baseline Neutrino Oscillations," *Phys.Rev.*, vol. D88, p. 073008, 2013.

[97] Y. Abe *et al.*, "Indication for the disappearance of reactor electron antineutrinos in the Double Chooz experiment," *Phys.Rev.Lett.*, vol. 108, p. 131801, 2012.

[98] P. Adamson *et al.*, "First Measurement of ν_μ and ν_e Events in an Off-Axis Horn-Focused Neutrino Beam," *Phys.Rev.Lett.*, vol. 102, p. 211801, 2009.

[99] G. Karagiorgi, Z. Djurcic, J. Conrad, M. Shaevitz, and M. Sorel, "Viability of Delta m**2 1- eV**2 sterile neutrino mixing models in light of MiniBooNE electron neutrino and antineutrino data from the Booster and NuMI beamlines," *Phys.Rev.*, vol. D80, p. 073001, 2009.

[100] P. Astier *et al.*, "Search for nu(mu) to nu(e) oscillations in the NOMAD experiment," *Phys.Lett.*, vol. B570, pp. 19–31, 2003.

[101] A. A. Aguilar-Arevalo *et al.*, "A Search for muon neutrino and antineutrino disappearance in MiniBooNE," *Phys.Rev.Lett.*, vol. 103, p. 061802, 2009.

[102] I. Stockdale, A. Bodek, F. Borcherding, N. Giokaris, K. Lang, *et al.*, "Limits on Muon Neutrino Oscillations in the Mass Range 55-eV**2 ¡ Delta m**2 ¡ 800-eV**2," *Phys.Rev.Lett.*, vol. 52, p. 1384, 1984.

[103] F. Dydak, G. Feldman, C. Guyot, J. Merlo, H. Meyer, *et al.*, "A Search for Muon-neutrino Oscillations in the Delta m**2 Range 0.3-eV**2 to 90-eV**2," *Phys.Lett.*, vol. B134, p. 281, 1984.

[104] P. Adamson *et al.*, "An improved measurement of muon antineutrino disappearance in MINOS," *Phys.Rev.Lett.*, vol. 108, p. 191801, 2012.

[105] P. Adamson *et al.*, "Search for the disappearance of muon antineutrinos in the NuMI neutrino beam," *Phys.Rev.*, vol. D84, p. 071103, 2011.

[106] P. Adamson *et al.*, "Measurement of the neutrino mass splitting and flavor mixing by MINOS," *Phys.Rev.Lett.*, vol. 106, p. 181801, 2011.

[107] A. Sousa, "First MINOS+ Data and New Results from MINOS." Slides from Neutrino2014 (Proceedings in Preparation), 2014.

[108] M. Maltoni, T. Schwetz, M. Tortola, and J. Valle, "Status of global fits to neutrino oscillations," *New J.Phys.*, vol. 6, p. 122, 2004.

[109] J. Conrad and M. Shaevitz, "Limits on Electron Neutrino Disappearance from the KARMEN and LSND ν_e - Carbon Cross Section Data," *Phys.Rev.*, vol. D85, p. 013017, 2012.

[110] Y. Declais, J. Favier, A. Metref, H. Pessard, B. Achkar, *et al.*, "Search for neutrino oscillations at 15-meters, 40-meters, and 95-meters from a nuclear power reactor at Bugey," *Nucl.Phys.*, vol. B434, pp. 503–534, 1995.

[111] P. Brâemaud, *Markov chains: Gibbs fields, Monte Carlo simulation, and queues.* Springer, New York, 1999.

[112] M. Maltoni and T. Schwetz, "Testing the statistical compatibility of independent data sets," *Phys.Rev.*, vol. D68, p. 033020, 2003.

[113] K. Mahn *et al.*, "Dual baseline search for muon neutrino disappearance at $0.5\text{eV}^2 < \Delta m^2 < 40\text{eV}^2$," *Phys.Rev.*, vol. D85, p. 032007, 2012.

[114] G. Cheng *et al.*, "Dual baseline search for muon antineutrino disappearance at $0.1\text{eV}^2 < \Delta m^2 < 100\text{eV}^2$," *Phys.Rev.*, vol. D86, p. 052009, 2012.

[115] M. Antonello *et al.*, "Search for anomalies in the ν_e appearance from a ν_μ beam," *Eur.Phys.J.*, vol. C73, p. 2599, 2013.

[116] N. Agafonova *et al.*, "Search for $\nu_\mu \to \nu_e$ oscillations with the OPERA experiment in the CNGS beam," *JHEP*, vol. 1307, p. 004, 2013.

[117] H. Chen *et al.*, "Proposal for a New Experiment Using the Booster and NuMI Neutrino Beamlines: MicroBooNE," 2007. FERMILAB-PROPOSAL-0974.

[118] C. Anderson, M. Antonello, B. Baller, T. Bolton, C. Bromberg, *et al.*, "The ArgoNeuT Detector in the NuMI Low-Energy beam line at Fermilab," *JINST*, vol. 7, p. P10019, 2012.

[119] M. Antonello *et al.*, "Analysis of Liquid Argon Scintillation Light Signals with the ICARUS T600 Detector," *ICARUS-TM*, vol. 06-03, 2006.

[120] C. Admas, C. Andreopoulos, J. Asaadi, B. Baller, M. Bishai, *et al.*, "LAr1-ND: Testing Neutrino Anomalies with Multiple LAr TPC Detectors at Fermilab," 2013.

[121] J. Asaadi, J. Conrad, S. Gollapinni, B. Jones, H. Jostlein, *et al.*, "Testing of High Voltage Surge Protection Devices for Use in Liquid Argon TPC Detectors," 2014.

[122] A. Szelc. Private Communication, 2013.

[123] S. Kubota and others., "Recombination luminescence in liquid argon and liquid xenon.," *Phys. Rev B*, vol. 17:2762, 1978.

[124] A. Molchanov, "Lasers in the vacuum ultraviolet and in the x-ray regions of the spectrum," *Sov. Phys. Usp,*, vol. 15:124, 1972.

[125] P. Cennini, J. Revol, C. Rubbia, F. Sergiampietri, A. Bueno, *et al.*, "Detection of scintillation light in coincidence with ionizing tracks in a liquid argon time projection chamber," *Nucl.Instrum.Meth.*, vol. A432, pp. 240–248, 1999.

[126] B. Jones, C. Chiu, J. Conrad, C. Ignarra, T. Katori, *et al.*, "A Measurement of the Absorption of Liquid Argon Scintillation Light by Dissolved Nitrogen at the Part-Per-Million Level," *JINST*, vol. 8, p. P07011, 2013.

[127] P. Nienaber. Private Communication, 2012.

[128] V. Gehman, S. Seibert, K. Rielage, A. Hime, Y. Sun, *et al.*, "Fluorescence Efficiency and Visible Re-emission Spectrum of Tetraphenyl Butadiene Films at Extreme Ultraviolet Wavelengths," *Nucl.Instrum.Meth.*, vol. A654, pp. 116–121, 2011.

[129] P. Benetti, R. Acciarri, F. Adamo, B. Baibussinov, M. Baldo-Ceolin, *et al.*, "First results from a Dark Matter search with liquid Argon at 87 K in the Gran Sasso Underground Laboratory," *Astropart.Phys.*, vol. 28, pp. 495–507, 2008.

[130] A. Hime, "The MiniCLEAN Dark Matter Experiment," 2011. arXiv:1110.1005 [hep-ex].

[131] "Vacuum ultraviolet deuterium light source model 632." http://mcphersoninc.com/lightsources/632.pdf.

[132] "Airgas." www.airgas.com.

[133] B. Jones, J. VanGemert, J. Conrad, and A. Pla-Dalmau, "Photodegradation Mechanisms of Tetraphenyl Butadiene Coatings for Liquid Argon Detectors," *JINST*, vol. 8, p. P01013, 2013.

[134] "The warp programme." 2008 Annual Report, preprint number LNGS-AR-2008-WArP.

[135] J. Zennamo, "Muon Neutrino Disappearance with MicroBooNE and LAr1-ND." Poster from Neutrino2014 (Proceedings in Preparation), 2014.

[136] R. Acciarri *et al.*, "Measurements of Inclusive Muon Neutrino and Antineutrino Charged Current Differential Cross Sections on Argon in the NuMI Antineutrino Beam," *Phys.Rev.*, vol. D89, p. 112003, 2014.

[137] R. Acciarri *et al.*, "The detection of back-to-back proton pairs in Charged-Current neutrino interactions with the ArgoNeuT detector in the NuMI low energy beam line," *Phys.Rev.*, vol. D90, p. 012008, 2014.

[138] P. Adamson *et al.*, "LArIAT: Liquid Argon TPC in a Test Beam," 2013.

[139] H. Berns *et al.*, "The CAPTAIN Detector and Physics Program," 2013.

[140] H. Chen *et al.*, "A LOI for a Neutrino Oscillation Experiment on the Booster Neutrino Beamline: LAr1," *Fermilab Letter of Intent*, vol. P-1030, 2012.

[141] S. Ritz *et al.*, "Building for Discovery: Strategic Plan for U.S. Particle Physics in the Global Context," 2014.

[142] L. Stanco, A. Anokhina, A. Bagulya, M. Benettoni, P. Bernardini, *et al.*, "The NESSiE Concept for Sterile Neutrinos," 2013.

[143] B. Baibussinov, M. Baldo Ceolin, G. Battistoni, P. Benetti, A. Borio, *et al.*, "A New, very massive modular Liquid Argon Imaging Chamber to detect low energy off-axis neutrinos from the CNGS beam: Project MODULAr," *Astropart.Phys.*, vol. 29, pp. 174–187, 2008.

[144] J. Thomas, "GLADE Global Liquid Argon Detector Experiment: a letter of intent to FNAL," 2012.

[145] A. Badertscher, T. Hasegawa, T. Kobayashi, A. Marchionni, A. Meregaglia, *et al.*, "A Possible Future Long Baseline Neutrino and Nucleon Decay Experiment with a 100 kton Liquid Argon TPC at Okinoshima using the J-PARC Neutrino Facility," 2008.

[146] R. Acciarri *et al.*, "Effects of Nitrogen contamination in liquid Argon," *Nucl. Phys. Proc. Suppl.*, vol. 197, pp. 70–73, 2009.

[147] R. Acciarri *et al.*, "Oxygen contamination in liquid Argon: combined effects on ionization electron charge and scintillation light," *JINST*, vol. 5, p. P05003, 2010.

[148] B. Jones, "A simulation of the optical attenuation of TPB coated light-guide detectors," *JINST*, vol. 8, p. C10015, 2013.

[149] nEDM experiment at SNS. Private Communication, 2012.

[150] Z. Moss. Private Communication, 2014.

[151] M. Antonello, B. Baibussinov, V. Bellini, H. Bilokon, F. Boffelli, *et al.*, "ICARUS at FNAL," 2013.

[152] M. Antonello, B. Baibussinov, V. Bellini, H. Bilokon, F. Boffelli, *et al.*, "ICARUS at FNAL," 2013.

[153] J. Conrad and M. Shaevitz, "Electron Antineutrino Disappearance at KamLAND and JUNO as Decisive Tests of the Short Baseline Anti-nu_mu to Anti-nu_e Appearance Anomaly," *Phys.Rev.*, vol. D89, p. 057301, 2014.

[154] C. Aberle, A. Adelmann, J. Alonso, W. Barletta, R. Barlow, *et al.*, "Whitepaper on the DAEdALUS Program," 2013.

[155] G. Bellini *et al.*, "SOX: Short distance neutrino Oscillations with BoreXino," *JHEP*, vol. 1308, p. 038, 2013.

[156] G. Alimonti *et al.*, "Science and technology of BOREXINO: A Real time detector for low-energy solar neutrinos," *Astropart.Phys.*, vol. 16, pp. 205–234, 2002.

[157] D. Adey *et al.*, "Light sterile neutrino sensitivity at the nuSTORM facility," *Phys.Rev.*, vol. D89, p. 071301, 2014.

[158] M. Elnimr *et al.*, "The OscSNS White Paper," 2013.

[159] "OscSNS: A Precision Neutrino Oscillation Experiment at the SNS," 2013.

[160] A. Anderson, J. Conrad, E. Figueroa-Feliciano, C. Ignarra, G. Karagiorgi, *et al.*, "Measuring Active-to-Sterile Neutrino Oscillations with Neutral Current Coherent Neutrino-Nucleus Scattering," *Phys.Rev.*, vol. D86, p. 013004, 2012.

[161] R. Agnese *et al.*, "Silicon Detector Dark Matter Results from the Final Exposure of CDMS II," *Phys.Rev.Lett.*, vol. 111, p. 251301, 2013.